UNIVERSITY OF CALIFORNIA
RIVERSIDE

Real-Time Sub-Meter Vehicle Positioning: Low-Cost GNSS-Aided INS

A Dissertation submitted in partial satisfaction
of the requirements for the degree of

Doctor of Philosophy

in

Electrical Engineering

by

Farzana S. Rahman

June 2020

Dissertation Committee:

Dr. Jay A. Farrell, Chairperson
Dr. Matthew J. Barth
Dr. Amit K. Roy-Chowdhury

The Dissertation of Farzana S. Rahman is approved:

Committee Chairperson

University of California, Riverside

Acknowledgments

I would like to express my deepest appreciation towards everyone who has contributed, directly or indirectly, to the realization of my PhD thesis.

I would like to express my sincere gratitude towards my supervisor, Professor Jay A. Farrell, who supported and encouraged me, provided me with guidance, and kept my spirits up all through my PhD journey at University of California Riverside. His vast knowledge and deep thinking has helped me to develop as a matured engineer. I could not have imagined having a better advisor and mentor for my PhD study.

Besides my advisor, I would like to thank the rest of my thesis committee: Professor Matthew Barth, and Professor Amit K. Roy-Chowdhury for their support in developing this thesis. During my PhD, I was fortunate enough to work with Professor Barth in one of my projects. His expertise, guidance and motivation helped me a lot in conducting that research. I also had the opportunity to attend Professor Roy-Chowdhury's courses that have provided me with excellent understanding about the basics of image processing and computer vision.

I would like to thank all of my colleagues at the Control and Robotics lab UCR, who have helped me with my research and also made my time at the School so enjoyable. In particular, I would like to thank Dr. Felipe Oliveira Silva for his technical support and constructive input with regard to this research. I would like to thank Dr. Paul Roysdon, Dr. Elahe Aghapour, Dr. Mohammad Billah, Zeyi Jiang, Jean-Bernard Uwineza, Wang Hu and Ashim Neupane for all the stimulating discussions in the last four year.

Last but not the least, I would like to thank my parents for their inspiration and continuous support to pursue my PhD. My indebtedness for their sacrifice can not be expressed in words. I am

grateful to my sister Mushfika Rahman for her never-ending love and support. Most importantly, I wish to thank my loving and supportive husband, Jawadul Bappy, who gave me perpetual inspiration. I also like to thank my mother-in law, father-in-law and sister-in-law for their guidance and motivation.

To my parents.

ABSTRACT OF THE DISSERTATION

Real-Time Sub-Meter Vehicle Positioning: Low-Cost GNSS-Aided INS

by

Farzana S. Rahman

Doctor of Philosophy, Graduate Program in Electrical Engineering
University of California, Riverside, June 2020
Dr. Jay A. Farrell, Chairperson

Many applications, including connected and autonomous vehicles, would benefit from navigation technologies that reliably achieve sub-meter position accuracy. Real-time submeter Earth-referenced positioning accuracy has the potential to be achieved with high reliability on moving vehicles by using Global Navigation Satellite Systems (GNSS) if common-mode ranging error correction information is communicated to the vehicles. For successful commercial implementation, such correction information must be delivered on continental or global scales. The communication latency must be small enough to not significantly affect performance. The main focus of the study is to investigate the feasibility to achieve sub-meter positioning accuracy with low-cost GNSS receiver and Inertial Measurement Unit (IMU) sensor. The thesis is divided into two phases based on their common-mode compensation approach. The first phase considers Local Area Differential GNSS (LADGNSS) approach and the second phase investigates Wide Area Differential GNSS (WADGNSS) method.

The first part of this project presents a local differential correction computation methodology designed to be robust to latency and studied position estimation accuracy as a function of dif-

ferential correction latency for both stationary and moving receivers [121, 122]. This performance was robust to latency up to 600 seconds. Two algorithms incorporated the local differential correction approach defined in [122]. The Position, Velocity, Acceleration (PVA) approach used only DGNSS data with a Kalman filter. The Inertial Navigation System (INS) approach used DGNSS and inertial measurement data within an extended Kalman filter(EKF). The study showed that both approaches achieved performance exceeding the Society of Automotive Engineering (SAE) J2945 specification (1.5 meter horizontal accuracy and 3.0 meter vertical accuracy at 68%) [12] with PVA achieving 1 m horizontal accuracy at 90% and 2 m vertical accuracy at 95% and the INS approach using a consumer-grade IMU achieved 1 m horizontal accuracy at 98% and 2 m vertical accuracy at 95% [125].

The second phase of this project investigates methods for implementing DGNSS corrections on a continental scale, to study the achievable accuracy. The overview includes discussion of WADGNSS, the models that it incorporates, the modeling agencies, and the existing data and model sources. The paper presents a Precise Point Positioning (PPP) aided INS design and analyzes navigation performance as a function of IMU quality. This paper considers GNSS PPP with Least Square (LS), PVA and EKF for static and only EKF for dynamic condition. The experimental results demonstrate positioning accuracy that surpasses the SAE specification using PPP corrected single frequency, single constellation GNSS measurements along with a consumer-grade IMU sensor. Experiments performed in this project (see Section 5.2.2) have demonstrated horizontal position accuracies of 1.35 ± 0.48, 1.19 ± 0.41, and 0.47 ± 0.26 using PPP PVA and demonstrated horizontal position accuracies of 0.81 ± 0.21, 0.52 ± 0.25, and 0.43 ± 0.186 using PPP INS for stationary dataset. Horizontal and vertical position accuracies (see Section 5.2.3) are 0.80 ± 0.40 and 2.32 ±

1.14 with PPP INS respectively for dynamic condition.

This study focuses on single frequency, single constellation results. The availability of multiple constellations and multiple frequencies per constellation will facilitate estimation and compensation of ionospheric error, accommodation of outliers, and accommodation of multipath. It will also greatly increase the number of available measurements and the likelihood that the user has available a set of satellites with appropriate geometry to reliably achieve the performance specification.

Contents

List of Figures

List of Tables

Chapter 1

Introduction

1.1 Background

The introduction of satellite navigation is one of the greatest technological innovations. The development of Global Navigation Satellite Systems (GNSS), started a new and exciting era in positioning, navigation, and timing at the end of the twentieth century. Estimates of position, velocity, and time have become available instantaneously and inexpensively. Since its inception in the late 1970s, GNSS has revolutionized positioning and navigation along with geodesy, geospatial science and technology. Although the primary intention of the system was for military purposes, researchers soon recognized the versatility of this system. There are a myriad of civilian applications such as vehicle, air and marine navigation, machine guidance/control, search and rescue, mapping and tracking, precision farming, and land surveying where GNSS can be utilized.

Over the last several decades, GNSS have become dominant for personal and vehicular navigation. GNSS [20, 108] have been reliably used to achieve positioning accuracy of about 10 m for twentieth century. A new generation of applications (e.g., autonomous vehicles, connected vehicles, driver's assistance, Blind Spot Warning (BSW), smart parking, and connected eco-driving, High Speed Differential Warning (HSDW) etc.) are placing much stricter specifications on position accuracy and reliability for navigation systems than was previously required [16, 25, 75, 84]. The FHWA, state DOTs, and auto manufacturers are investigating connected and autonomous highway vehicle applications which will benefit from real-time, ECEF position estimates accurate to sub-meter level at 99% probability. Pilot projects are ongoing in at least three locations [25,75,84]. The objectives include improving roadway network safety and throughput, while decreasing emissions impact.

Although started earlier, GNSS only became fully operational in 1995 and selective availability, which restricted the quality of the signal for civilian use, was ended in 2000. GNSS receivers receive coarse/acquisition codes from the satellite and compare them with its own signal to provide a distance from the receiver to the satellite, called the pseudorange. The pseudorange measurement is corrupted with several errors. The most well-known methodology to compensate these error terms is called relative or Differential GNSS (DGNSS). DGNSS can be of two major types: (a) Local Area Differential GNSS (LADGNSS) and (b) Wide Area Differential GNSS (WADGNSS). LADGNSS positioning technique involves a minimum of two receivers are required for positioning. One is referred as a base station receiver set up, while the other receiver acts as a rover receiver, which coordinates are needed to be determined. Base station positions are known precisely and both the receivers are required to simultaneously observe the same set of satellites. The errors common to receivers in same vicinity (i.e. satellite orbit, satellite clock, ionospheric delay, tropospheric delay etc.) are similar and have temporal and spatial correlation. Commonly cited single frequency pseudorange LADGNSS position accuracy levels are 1-3 meters [37, 53, 140]. The lower end of this range approaches the sub-meter specification, if this accuracy can be achieved with sufficient reliability and if it is not sensitive to DGNSS correction communication latencies. Navigation systems achieving these accuracy and reliability specifications have been demonstrated in [121]. For a national scale of implementation, topics of interest include: communication physical layers, network design for real-time applications, position error sensitivity to communication latency, and estimation algorithms to achieve the accuracy specification.

The concept of LADGNSS has been utilized over the last two decades. The accuracy of relative positioning is also constrained by the baseline length. As the baseline length increases, the correlation between errors decreases. This limits the accuracy of the positioning solutions. Therefore, the implementation of LADGNSS corrections are not feasible for continent scale. That is why a great part of localization technology focuses on Wide Area Differential GNSS (WADGNSS) based receiver navigation application. There are several methods to compute and communicate WADGNSS corrections for stand-alone rover position estimation (e.g. Virtual Reference Stations (VRS) [93], Satellite Based Augmentation System (SBAS) [145], Precise Point Positioning (PPP) etc.).

In the late 1990s, the construction of Continuously Operating Reference Station (CORS) networks around the world led to the computation of precise satellite orbit and clock corrections. These corrections made high accuracy point positioning using a single GPS receiver possible. This novel positioning technique is known as Precise Point Positioning (PPP) [154]. The concept of PPP [8] was first introduced to obtain high accuracy for single GNSS receivers using precise data products (i.e., atmospheric models, precise satellite orbit and clock, satellite hardware biases) derived from external sources. Most often, such PPP approaches use undifferenced ionosphere-free code and carrier phase observations from dual frequency receivers [89, 142, 154], where centimeter accuracy is achievable when carrier phase ambiguities can be resolved. The original PPP results were only feasible in post-processing due to latency in the required PPP data products [18, 57]. For on-vehicle applications, real-time results are needed without long ambiguity convergence times. Various organizations (e.g. International GNSS Service (IGS), European Space Agency (ESA), National Oceanic and Atmospheric Administration (NOAA), Federal Aviation Administration (FAA)) use networks of GNSS stations, to provide one or more components of the PPP correction in real-time. These real-time data products enable users to compute common-mode error-free code and phase measurements for estimating online receiver location without any nearby reference station.

Inertial navigation is a well understood and widely used technology for rover positioning. With recent significant progress in microelectromechanical systems (MEMS) technology, research interest in the application of low-grade IMU to navigation has been growing. IMU is a self-contained system and independent of any external signal. However, if a navigation system uses only IMU, errors in position and attitude are accumulated due to IMU errors as time passes. Since MEMS IMU usually has large errors, errors in position and attitude can grow very rapidly. Thus, current low-grade MEMS IMU alone offers short-term stability, but unsuitable for long-term reliable rover navigation. IMU accuracy is well studied as a function of aiding sensor availability and can easily be computed while the system is in operation. Using the complementary properties of GNSS and IMU, a navigation system can be constructed from the integration of both sensors that results in long-term stability and reliability. This method is known as GNSS-aided Inertial Navigation System (INS).

The main advantage of Inertial Navigation System (INS) is the estimation of the full vehicle state (position, velocity, acceleration, attitude and angular rate) continuously at high rates. The benefit of the integrated approach is not only limited to high rate rover state information but also for performance maintenance for GNSS signal outages and outliers. In open areas where signals from GNSS satellites are not interrupted, frequent measurement updates are available and the rapid error growth in INS with MEMS IMU may not be of great concern. One interesting research area in the navigation application, is the investigation of inertial sensor performance degradation with GNSS measurement outage periods.

1.2 Related Works

Vehicle positioning by standard GNSS and LADGNSS [45, 47, 49, 63, 92, 141] are both very well researched areas. Real-life challenges in LADGNSS positioning are sensitivity of position error to baseline separation and communication latency. In selective availability (SA) era there were many investigations to characterize sensitivity to LADGNSS correction latency [50, 90, 104]. Due to the design of SA, as intended, the correction error and hence the position error grew rapidly over tens of seconds. Until recently [121, 126], the literature lacked studies of real-time position estimation accuracy versus correction latency in the post-SA era. The literature presents extensive position estimation theory, estimation algorithms, and experimental results that illustrate alternative modeling choices and their impact on performance and reliability, for example [5, 7, 29, 132, 133].

WADGNSS is another rover positioning concept, utilized to compensate for GNSS measurement errors. One significant feature of WADGNSS branch is the PPP algorithms. This is one of the major focus of this research study. In previous works, PPP results were only feasible in post-processing due to latency in the required PPP data products [18, 57]. In current time, many organizations (i.e. IGS, JPL etc.) are working on providing real-time PPP corrections. Therefore, studies regarding real-time PPP implementation can be found. Krzan [91], Nguyen [113], Elsobeiey [44] and Liu [100] all present real-time PPP implementations using IGS Real-Time Service (IGS-RTS) products. The ionospheric delay is compensated by computing iono-free code and phase measurement from dual frequency signals. Although, many works mention IGS-RTS real-time PPP implementations, majority of the studies utilize dual-frequency code and phase measurements. Due to cost constraint in consumer markets, our focus is on single frequency positioning. Very few examples have been found to showcase IGS-RTS performance using real-time single frequency (SF) PPP methods. Among these few illustrations, Elsheikh [43] claims to achieve 60 cm accuracy using single frequency multi-GNSS code and phase measurement for moving platform.

Real-Time PPP (RT-PPP) approaches using corrections from other sources have also been proposed. Gao and Chen [56, 58], for instance, has developed a single frequency (SF) RT-PPP algorithm using JPL's precise orbit and clock products. Their work compensates for ionosphere error by combining code and carrier phase measurements. The carrier phase ambiguity resolution convergence time is 2-4 hours which is too long for automotive applications. Bree and Tiberius [87, 146, 147] uses real-time precise orbit and clock correction from REal-TIme CLock Estimation (RETICLE) service, which has been developed at the German Space Operations Center of the German Aerospace Center (GSOC/DLR). The predicted global ionospheric maps (GIM) and predicted Differential Code Bias (DCB) from the Center for Orbit Determination (CODE) in Bern are used in order to realize real-time SF-PPP. Their reported accuracies are 0.30 m and 0.71 m for stationary and moving platform respectively. The algorithm uses code and phase measurements with convergence time of 180 epochs.

The PPP corrections utilized in this study, consist of real-time precise orbit, clock from IGS-RTS [66], ionosphere parameters from US-TEC [55] and predicted satellite hardware bias (DCB) from CODE. The troposphere error is corrected using UNB3M model [48, 96]. The algorithm utilizes single frequency pseudorange and Doppler measurement from GPS constellation only.

For the last decade, many reliable and accurate GNSS aided INS implementations are found in literature for ground vehicle applications (e.g. car, freight) [127, 135, 144, 145]. GNSS and INS integration with LADGNSS correction is widely discussed in the literature [49, 123, 126, 140, 149]. Recent years have displayed some illustrations of GNSS-aided INS systems compensated with PPP correction. This particular integration approach is referred to as PPP-INS [36, 43, 100]. GNSS and inertial sensor integration has been accomplished by a variety of methods: Extended Kalman Filter (EKF) [9, 51]; complementary Kalman filtering [67]; Unscented KF (UKF) [153]; and, Extended Particle filter (EPF) [3]. Use of Doppler improves positioning accuracy on moving platforms by measuring velocity [5, 7, 132, 133]. A less well understood benefit of the Doppler measurement is that it enhances the degree-of-observability of the multipath states. This topic with a simple example is discussed in [121]. A tightly coupled Precise Point Positioning (PPP) approach is presented in [102] using an EKF algorithm. Smoothing approaches for trajectory estimation are presented in [99, 148].

1.3 Main Contribution

The main focus of this study is the feasibility of sub-meter positioning accuracy with real-time PPP-corrected single-frequency GNSS receiver integrated to consumer-grade inertial sensors.

The contributions of this study can be categorized into two sections: (a) Local area differential approach (b) PPP approach.

LADGNSS Approach:

Specific topics of interest for LADGNSS approach are:

- Theoretically expected pseudorange accuracy; measurement model and common-mode error compensation approach.
- Discussion about the differential correction latency compensation approach (see Section 3.1.1 and 3.1.2) and the state estimation algorithms used herein.
- Approaches for accurately estimating the state of a moving platform is presented in Section 5.1.7. Section 5.1.9 shows experimental results that demonstrate meter-level positioning performance that is robust to correction latency. Because this study focuses on robustness to communication latency, the experimental data sets were selected under open sky conditions. The performance demonstrated herein would not extend to urban canyon conditions where the challenges arise from non-line of sight measurement effects and the lack of satellites.

PPP Approach:

The contributions for PPP are included herein:

- Detailed methodology for PPP correction computation approach is presented in Section 3.4;
- Stochastic noise characteristics of different inertial sensor grades and the resulting noise effect in rover positioning;

- The extent to which state estimation algorithms can achieve the position accuracy and reliability specifications currently envisioned for driver assistance, connected vehicle, and autonomous vehicle applications [12] using consumer-grade PPP-INS system; The results are mentioned in Section 5.2.2 and 5.2.3.
- The discussion about feasibility of positioning accuracy for moving platform is presented in Section 5.2.4.

This article focuses on consumer applications, such as the automotive market, where low cost time-to-first-fix, and reliability is a primary drivers. Motivated by low cost, we focus on single-frequency (i.e., GPS L1) receivers. Given single-frequency receivers, carrier phase ambiguity would be unreliable and could take significant time whenever lock is lost; therefore, our focus is on methods that use only pseudorange and Doppler.

All methods presented herein apply in theory to other frequencies and constellations. At present, the PPP data is only available for GPS; therefore, this paper only considers GPS. Availability of phase measurements could greatly improve positioning accuracy if L1 integer ambiguities could be reliably estimated [140] or if convergence times of float estimates of integers could be (greatly) reduced [26].

Chapter 2

GNSS Background

This section introduces notation and GNSS measurement models. GNSS receivers provide three measurements: pseudorange, carrier phase, and Doppler. At present, on inexpensive commercial receivers, these signals are available only on a single frequency referred to as L1. In the near-future, low-cost consumer receivers are expected to provide additional measurements from multiple constellations (e.g., GPS, GLONASS, Galileo, BeiDou) and at multiple frequencies (i.e., L1, L2, and L5 for GPS). The methods discussed herein generalize to multiple frequencies and constellations. Additional frequencies and multiple constellations will further enhance performance. For example, measurements at multiple frequencies will improve estimation of ionospheric delay. Multiple constellations and multiple frequencies will greatly increase the number of measurements allowing attenuation of multipath and outlier effects. This study focuses on users with access to L1 pseudorange and Doppler measurements from the GPS constellation. Availability of phase measurements could also greatly improve positioning accuracy if L1 integer ambiguities could be reliably estimated [140] or if convergence times of float estimates of integers [26] could be (greatly) reduced. Additional information on various GNSS system along with their measurement and correction model can be found in [21, 45, 49, 109, 118].

2.1 Notation

To clearly distinguish between models and computations, this article will use two different symbols. The symbol $\doteq$ indicates that the equation is a model. Models are used to analyze, understand, and physically interpret measurements, often with the goal of designing algorithms to estimate quantities that are of interest (e.g., position). The symbol $=$ indicates that an equation represents an actual algorithmic calculation.

When it is necessary to represent the actual, measured, and computed versions of a variable, x will represent the actual value, $\tilde{x}$ will represent the measured value, $\hat{x}$ will represent the computed or estimated value. Vector and matrix variables will be printed in bold font. For example, $\mathbf{p}^s$ represents the actual position vector for satellite s while $\hat{\mathbf{p}}^s$ represents the position vector for satellite s computed from the available ephemeris data.

2.2 GNSS Measurement Model

GNSS receivers track signals from satellites to provide pseudorange, phase and Doppler measurements. For the GPS system, the dual frequency measurement models are:

$$\begin{aligned}
\rho^s_{r,L1} &\doteq R(\mathbf{p}_r, \hat{\mathbf{p}}^s) + ct_r + cb_{r_{L1,\rho}} + M^s_{r,\rho 1} + \eta^s_{r,\rho 1} \\
&\quad -ct^s + E^s_r + I^s_{L1} + T^s - cb^s_{L1,\rho}, \qquad (2.1) \\
\rho^s_{r,L2} &\doteq R(\mathbf{p}_r, \hat{\mathbf{p}}^s) + ct_r + cb_{r_{L2,\rho}} + M^s_{r,\rho 2} + \eta^s_{r,\rho 2} \\
&\quad -ct^s + E^s_r + I^s_{L2} + T^s - cb^s_{L2,\rho}, \qquad (2.2) \\
\phi^s_{r,L1} &\doteq R(\mathbf{p}_r, \hat{\mathbf{p}}^s) + ct_r + cb_{r_{L1,\phi}} + \lambda_{L1} N^s_{r,L1} + M^s_{r,\phi 1} + \eta^s_{r,\phi 1} \\
&\quad -ct^s + E^s_r - I^s_{L1} + T^s - cb^s_{L1,\phi}, \qquad (2.3) \\
\phi^s_{r,L2} &\doteq R(\mathbf{p}_r, \hat{\mathbf{p}}^s) + ct_r + cb_{r_{L2,\phi}} + \lambda_{L2} N^s_{r,L2} + M^s_{r,\phi 2} + \eta^s_{r,\phi 2} \\
&\quad -ct^s + E^s_r - I^s_{L2} + T^s - cb^s_{L2,\phi}. \qquad (2.4) \\
\lambda D^s_{r,L1} &\doteq \mathbf{h}^s_r \cdot (\mathbf{v}_r - \mathbf{v}^s) + cB_r - cB^s + \eta^s_{r,D1} \qquad (2.5) \\
\lambda D^s_{r,L2} &\doteq \mathbf{h}^s_r \cdot (\mathbf{v}_r - \mathbf{v}^s) + cB_r - cB^s + \eta^s_{r,D2} \qquad (2.6)
\end{aligned}$$

where ρ represents pseudorange and ϕ represents carrier phase. The subscript r counts over the number of available receivers. The superscript s counts over the number of available satellites. The symbols L1 and L2 indicate the two GPS carrier frequencies and λ_{L1} and λ_{L2} are the corresponding carrier signal wavelengths. The symbols $N^s_{r,L1}$ and $N^s_{r,L2}$ represent the L1 and L2 integer ambiguities that arise from carrier phase tracking. The desired information from these measurements is the range between the receiver position $\mathbf{p}_r$ and the satellite location $\mathbf{p}^s$

$$R(\mathbf{p}_r, \mathbf{p}^s) = \|\mathbf{p}_r - \mathbf{p}^s\|. \qquad (2.7)$$

$$E_r^s = R(\mathbf{p}_r, \mathbf{p}^s) - R(\mathbf{p}_r, \hat{\mathbf{p}}^s) \tag{2.8}$$

Ephemeris error E_r^s arises because the actual satellite position $\mathbf{p}^s$ is not the same as the satellite position $\hat{\mathbf{p}}^s$ computed from the ephemeris data. where the line-of-sight vector from satellite s to receiver r is

$$\mathbf{h}_r^s = \frac{\mathbf{p}_r - \mathbf{p}^s}{|\mathbf{p}_r - \mathbf{p}^s|}. \tag{2.9}$$

In a perfect vacuum the range would equal the product of the time-of-travel and the speed-of-light in a vacuum. Because the underlying measurement is the time-of-travel of a signal sent by the satellite and detected by the receiver, the timing measurement is corrupted by the receiver clock bias ct_r, the satellite clock bias ct^s, and signal path delays within the receiver cb_{r_f} and satellite cb_f^s, where f is either L1 or L2. The symbols $\mathbf{v}_r$ and $\mathbf{v}^s$ represent the receiver and satellite antennae velocity vectors, cB_r and cB^s are the receiver and satellite clock drift rates. For the remaining terms: I_f^s represents ionospheric delay for frequency f, T^s represents tropospheric error, M_r^s represents multipath error, and $\eta_{r,*}^s \sim \mathscr{N}(0, R_*^s)$ is white random noise affecting the measurement, $*$ is may be replaced by "$\rho 1$", "$\rho 2$", "$\phi 1$", "$\phi 2$", "$D1$" or , "$D2$". The error terms I_f^s and T^s arise because the signals travel through the Earth atmosphere, not a perfect vacuum.

The portions of this paper that discuss estimation of the information necessary to compute *GNSS corrections* will assume availability of a continent-wide (or global) network of high-quality receivers and antennae, at locations known to centimeter or better accuracy, that are recording both pseudorange and carrier phase measurements on (at least) two frequencies.

The portions of this report that are concerned with position estimation assume a consumer grade antenna and receiver that provides pseudorange and Doppler on a single frequency. All experimental results herein use data only from GPS. Performance would be enhanced by using data

Table 2.1: Standard GNSS error budget [55,66,96].

Source	Error Budget, m
Ephemeris error	2
Satellite clock offset	2
Ionospheric time delay	3-7
Tropospheric error	1
Receiver noise	0.2
Multipath effect	1-2
UERE, rms	4-8
Horizontal Position Error, rms (HDOP = 1.5)	6-12

from multiple GNSS's [34] or from multiple frequencies [105]. In this report, the user is considered a low-cost GNSS receiver. The user's measurement model of L1 measurements mentioned in eqns. (2.1),(2.3) and (2.5).

2.3 GNSS Measurement Errors

The L1 pseudorange measurement has 9 types of errors, (see [92], and Sections 1.2-1.3 of [140]). They can be classified into two categories:

- *Common-mode errors* (ephemeris, satellite clock bias, ionosphere, troposphere, satellite hardware bias) are common to all receivers in the same vicinity. In eqns. (2.1–2.4) the symbols representing these common-mode errors are in the second line of each equation.

- *Noncommon-mode errors* (receiver clock bias, receiver hardware bias, multipath, receiver noise) are different for each receiver.

Table 2.1 summarizes typical magnitudes for the various range error sources for standard GNSS, without differential corrections. The resulting horizontal position estimation accuracy does not achieve the desired specifications. Differential correction approaches (local DGNSS, network DGNSS, or PPP) aim to reduce the effects of the common-mode errors [10, 11, 47, 141] on the position estimates.

Chapter 3

DGNSS Correction Approach

This section discusses the DGNSS technique to compensate for GNSS common-mode errors and delineates various issues that must be addressed toward achieving sub-meter position accuracy and robustness to communication latency.

3.1 LADGNSS Correction

All DGNSS approaches use at least one base station with a high quality receiver and antenna located at a mechanically stable and known location p_b. Due to the base station antenna location being stationary and known, the DGNSS approach can estimate corrections for roving receivers, enabling significant enhancement in rover position estimation accuracy, assuming that the corrections can be communicated to the rovers in a time-effective manner. Quantification of "time effective" requires an understanding of the sensitivity of position accuracy to correction latency.

DGNSS can be implemented on local, regional or global scales. The standard local approach [47, 141] is described in Section 3.1.1. Regional and global approaches utilize a network of

GNSS receivers. The measurements from the network are combined to estimate correction information that is broadcast to users, such that each user can reconstruct a local correction [46, 83].

The collection of data from remote base receivers, computation and verification of corrections, and communication of corrections to users result in *latency* ℓ between the time-of-applicability t_0 and the time that it is actually used $t_0 + \ell$. Robustness to communication latency is critical.

A primary goal of this study is to evaluate the sensitivity of positioning accuracy to communication latency. For the purpose of this study, it is sufficient to utilize local corrections.

3.1.1 Standard Local DGNSS Corrections

The L1 pseudorange measurement model for base station is:

$$\begin{aligned} \rho_b^s &\doteq R(\mathbf{p}_b, \hat{\mathbf{p}}^s) + ct_b + cb_{b_{L1,\rho}} + M^s_{b,\rho 1} + \eta^s_{b,\rho 1} \\ &\quad - ct^s + E^s_b + I^s_{L1} + T^s - cb^s_{L1,\rho}, \end{aligned} \tag{3.1}$$

The local base station position $\mathbf{p}_b$ is known to centimeter accuracy, so that its error is neglected herein. At time t the base station algorithm computes

$$\tilde{c}^s = \rho_b^s - R(\mathbf{p}_b, \hat{\mathbf{p}}^s) - c\hat{t}_b + c\hat{t}^s \tag{3.2}$$

where ρ_b^s is the base pseudorange measurement, $R(\mathbf{p}_b, \hat{\mathbf{p}}^s) = |\mathbf{p}_b - \hat{\mathbf{p}}^s|$, $\hat{\mathbf{p}}^s$ and $c\hat{t}^s$ are the satellite position and clock bias computed from ephemeris data, and $c\hat{t}_b$ is an estimate of the base receiver clock bias.

The model for $\tilde{c}^s$ is

$$\tilde{c}^s \doteq I^s_{L1} + T^s + E^s_b - c\delta t^s - cb^s_{L1,\rho} + c\delta t_b + cb_{b_{L1,\rho}} + M^s_b + \eta^s_b \tag{3.3}$$

where $E^s = R(\mathbf{p}_b, \mathbf{p}^s) - R(\mathbf{p}_b, \hat{\mathbf{p}}^s)$ is satellite ephemeris error, $c\delta t^s = ct^s - c\hat{t}^s$ is residual satellite clock bias and $c\delta t_b = ct_b - c\hat{t}_b$ is residual receiver clock bias. Note that all of the terms on the right-hand side of eqn. (3.3) are unknown. The goal is that the broadcast correction should allow accurate prediction of the rover's common-mode error

$$I^s + T^s + E_b^s - c\delta t^s,$$

while being minimally influenced by the base station noncommon-mode error

$$M_b^s + \eta_b^s.$$

Eqn. (3.3) shows that $\tilde{c}^s$ contains both common and noncommon-mode errors; therefore, additional processing is desirable.

3.1.2 Approach to Decrease Multipath and Latency Effects

This section discusses a local base station algorithm first presented in [122] that is compatible with the RCTM standard [11].

Each noncommon-mode error source is correlated over only a few minutes whereas the common-mode error sources are correlated over several hours. Due to this frequency separation, various forms of low-pass filtering should attenuate the affects of the noncommon-mode errors.

Before filtering, it is useful to consider the ionospheric delay. When the ionospheric delay rate is high, a low-pass filtered correction would lag the present value of $\tilde{c}^s(t)$. The ionospheric delay has trends that are largely predictable using satellite data available at each base and rover. Therefore, the predictable portion of these terms is removed prior to filtering and added back into the filtered results.

Let $\hat{I}^s$ represents the ionosphere delay computed using Klobuchar model parameters sent in the navigation message. Subtracting this predicted ionospheric delay (and an estimate of the base clock $c\hat{t_b}$) produces the new computed variable

$$\tilde{d^s} = \tilde{c}^s - \hat{I}^s - c\hat{t_b}. \tag{3.4}$$

The model for $\tilde{d^s}(t)$ is

$$\begin{aligned} \tilde{d^s} &\doteq \delta I^s + T^s + E^s - c\delta t^s \\ &\quad + c\delta t_b + M_b^s + \eta_b^s \end{aligned} \tag{3.5}$$

where $\delta I^s \doteq I^s - \hat{I}^s$. The first line of eqn. (3.5) contains the desired signal for the corrections. These signals have very small changes in rate over long periods of time (i.e., many minutes). The second line of eqn. (3.5) contains the noncommon-mode errors. The first term is not critical. As long as the same value $c\hat{t_b}$ is subtracted for all satellites in eqn. (3.4), then only the magnitude of the corrections and the value of the rovering receiver's clock estimate will change. A well-designed base station is situated away from or above reflective surfaces and uses a high-quality antenna to minimize multipath effects. The base multipath error M_b^s typically has a correlation time of minutes and is assumed to be zero mean over many minutes. The measurement noise η_b^s changes rapidly and is zero mean over several minutes. Therefore, to also attain the ability to predict corrections at future times, the form of low pass filter that we select is line fitting.

At time t_0, the line $a_{t_0} + b_{t_0}(t - t_0)$ is fit to the data

$$\left\{ \tilde{d}(t) \text{ for } t \in [t_0 - L, t_0] \right\}.$$

The correction parameters $[a_{t_0}, b_{t_0}, t_0, IODE]$ are communicated from the base to the rover arriving at the rover at some time after t_0. The parameter $IODE$ ensures that the base and rover use the

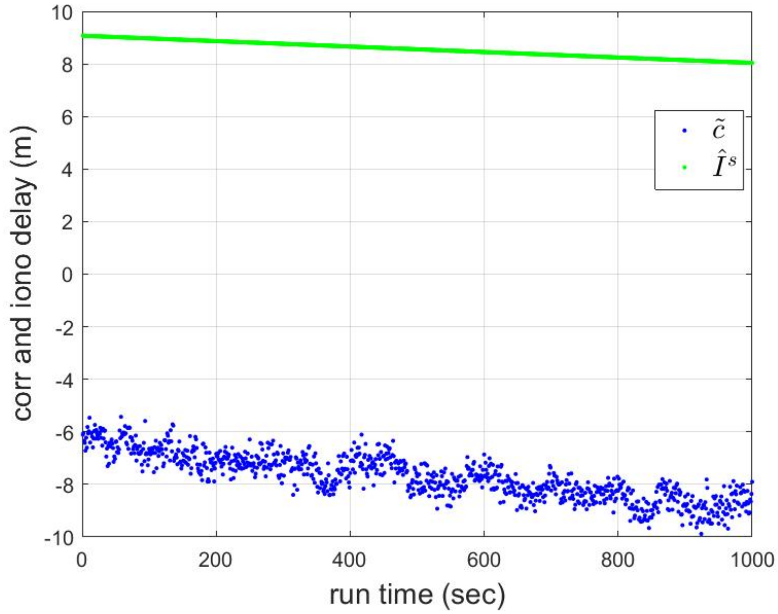

Figure 3.1: DGNSS correction $\tilde{c}$ (blue) and computed ionospheric delay $\hat{I}^s(t)$ (green).

same issue of ephemeris data. Figures showing example base station calculations are included in the Appendix of [122]. The differential correction in eqn. (3.6) is designed to be robust to latency and base station multipath error.

3.1.3 Example Computed Corrections

This section illustrates the DGNSS correction approach described in Section 3.1 using an example set of data. The blue points in Fig. 3.1 show the DGNSS corrections $\tilde{c}$ as computed using eqn. (3.2). The model corresponding to $\tilde{c}$ is defined in eqn. (3.3). An estimate $\hat{I}^s$ of the first term (i.e., I^s) is computable from ionosphere model parameters communicated in the satellite data and is plotted as the green line in Fig. 3.1.

The blue curve in Fig. 3.2 is the ionospheric-free DGNSS correction, $\tilde{d}$, formed using

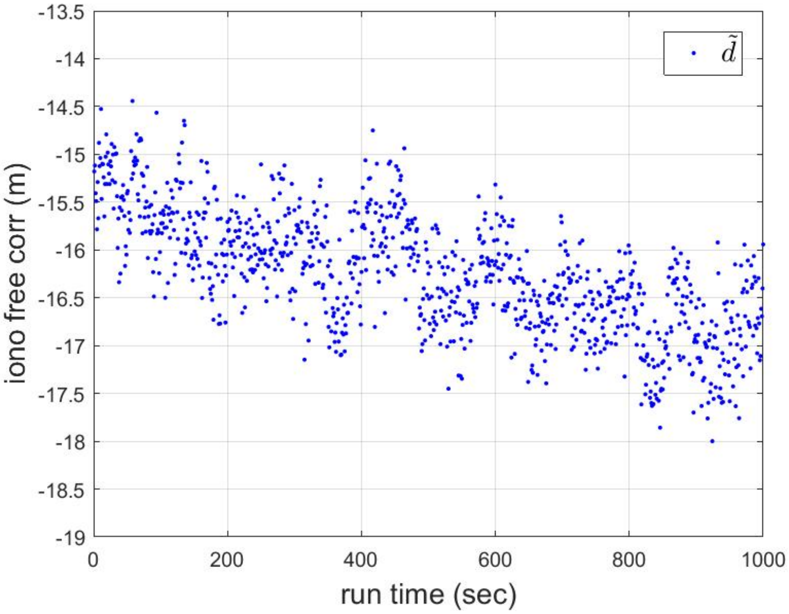

Figure 3.2: Ionospheric-free correction $\tilde{d}(t)$.

eqn. (3.4) and has the model described in eqn. (3.5). While the slope of $\tilde{c}$ was approximately 3 mm/sec, the slope of $\tilde{d}$ is reduced to approximately 1.5 mm/sec.

Over long periods of time (e.g., hours), $\tilde{d}$ will not be linear due to the rising and setting of the satellite causing the signal to traverse paths through different portions of the ionoshpere that vary in length and time of day. See Fig. 3.3. Alternative, over very short intervals of time, line fitting might fit either the random noise or multipath effects without providing useful predictive capability of future common-mode errors. For L greater than a few multiples of the multipath correlation time, multipath effects will be attenuated and the line fit should have useful predictive capabilities. In Fig. 3.4 the blue dots again show $\tilde{d}$. The red line shows the line fit to $\tilde{d}(t)$ for $t \in [t_0 - L, t_0]$ for $t_0 = 500$ and $L = 500$. On the interval $t \in [t_0 - L, t_0]$, the line follows the general trend of the data

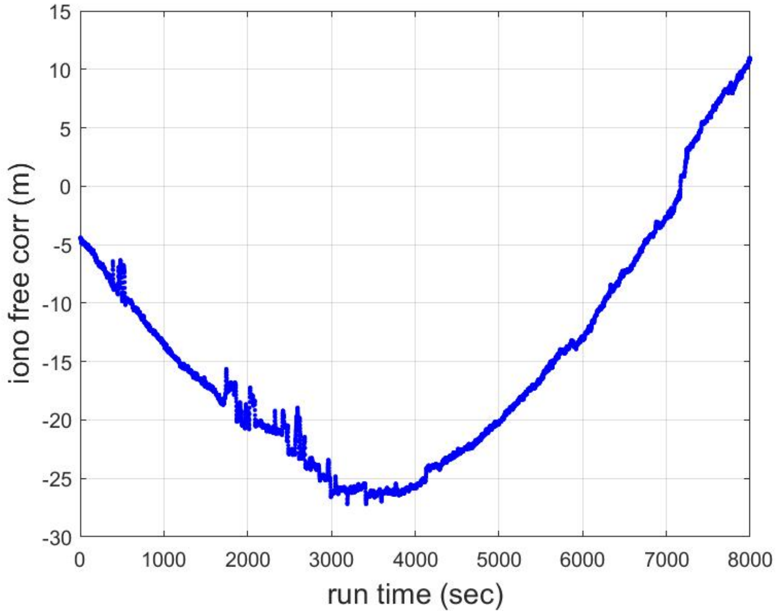

Figure 3.3: Ionospheric-free correction $\tilde{d}(t)$ for long period of time

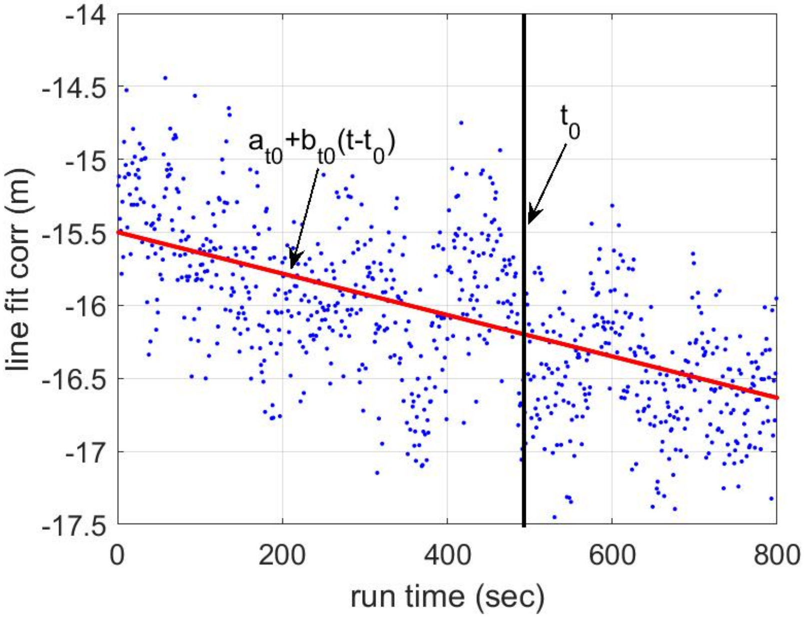

Figure 3.4: Line fit to ionospheric delay free correction.

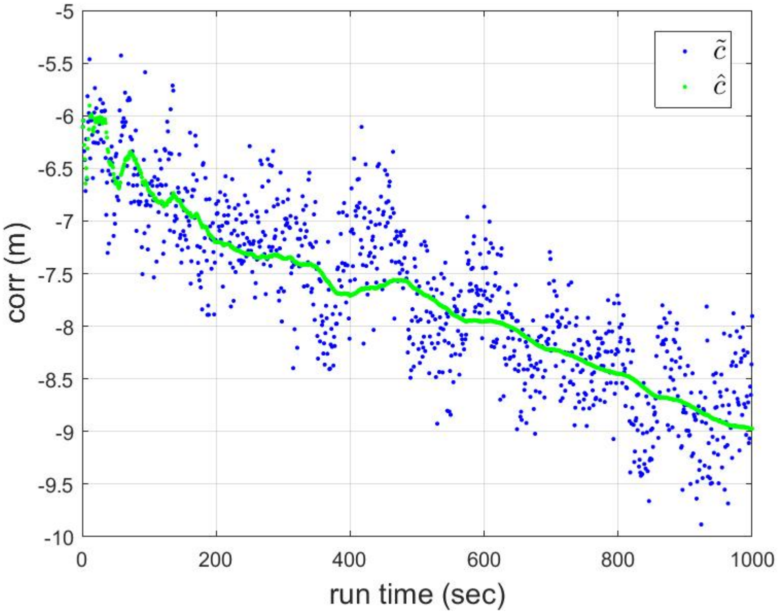

Figure 3.5: DGNSS correction raw data $\tilde{c}$ and computed correction $\hat{c}(t;t)$.

without following the random noise or multipath. For $t > t_o$, the line fit predicts the general trend of $\tilde{d}(t)$. The prediction accuracy will decease (as expected) as $(t - t_0)$ increases. Fitting the line to $\tilde{d}$ provides the parameters t_0, a_{t0} and b_{t0}.

Finally, the correction $\hat{c}(t;t)$, as computed using eqn. (3.6), is shown as the green line in Fig. 3.5 along with the original data (blue dots).

3.1.4 Rover Common-mode Error Compensation

For any time $t \geq t_0$, the rover computes the correction as

$$\hat{c}(t;t_0) = a_{t_0} + b_{t_0}(t - t_0) + \hat{I}^s(t). \tag{3.6}$$

The estimated ionospheric delay $\hat{I}^s(t)$ is computed using the same procedure as at the base station (i.e., Klobuchar model and parameters from the navigation message).

For position computations, the rover uses the DGNSS correction compensated pseudorange measurement:

$$\Delta\rho_r^s(t;t_0) = \rho_{r,L1}^s(t) - \hat{c}(t;t_0). \tag{3.7}$$

The symbol $\rho_{r,L1}^s$ symbolizes the rover pseudorange measurement mentioned in eqn. (2.1). The correction communication latency is $l = (t - t_0)$. Subsequent sections will study the effect of this latency on positioning accuracy, showing robustness for several hundred seconds of latency. Even in the ideal case where $\ell = 0$, the base and rover receiver are not synchronized. Each receiver makes its measurements according to its own clock.

The DGNSS compensated pseudorange model corresponding to eqn. (3.7) is

$$\begin{aligned}\Delta\rho_r^s(t;t_0) \quad &\doteq \quad R(\mathbf{p}_r(t), \hat{\mathbf{p}}^s(t)) + ct_r(t) + cb_{r_{L1,\rho}}(t) - c\delta t_b(t) - cb_{b_{L1,\rho}}(t) + (\hat{c}(t;t) - \hat{c}(t;t_0)) \\ &\quad + M_r^s(t) + \eta_r^s(t), \end{aligned} \tag{3.8}$$

where $\hat{c}(t;t)$ represents the actual common mode errors in the rover pseudo-range measurement at time t. The term $e(t,\ell) = (\hat{c}(t;t) - \hat{c}(t;t_0))$ accounts for the error in prediction of the common-mode errors due to communication latency.

3.1.5 Double-Differenced Rover Measurement Models

The DGNSS correction approach compensates common-mode errors affecting the pseudorange measurement. The receiver clock biases can be eliminated by double differencing (See Section 8.8.3 in [49]). In double-differencing, one differential satellite measurement is deducted from all the others. This operation removes clock bias errors at the cost of one fewer measurement for position (or state) estimation and causing the noise on all double-differenced measurements to be correlated.

The DGNSS compensated measurement model from eqn. (3.8) reduces to the below stated form

$$\Delta\rho_r^s \doteq R(p_r, \hat{p}^s) + ct_{rb} + e^s(\ell) + M_r^s + \eta_r^s, \tag{3.9}$$

where $ct_{rb} = ct_r + cb_{r_{L1,\rho}} - c\delta t_b - cb_{b_{L1,\rho}}$ and the time index t has been omitted for simplicity.

For the results herein, the pivot satellite ($s = s_p$) will be the one with the highest elevation angle. The double-differenced pseudorange measurement $d\rho_r^s$ is computed as

$$d\rho_r^s = \Delta\rho_r^s - \Delta\rho_r^{s_p}. \tag{3.10}$$

The corresponding measurement model is

$$d\rho_r^s \doteq R(\mathbf{p}_r, \hat{\mathbf{p}}^s) - R(\mathbf{p}_r, \hat{\mathbf{p}}^{s_p}) + de^s(\ell) + dM_r^s + d\eta_r^s, \tag{3.11}$$

where $de^s(\ell) = e^s(\ell) - e^{s_p}(\ell)$, $dM_r^s = M_r^s - M_r^{s_p}$ and $d\eta_r^s = \eta_r^s - \eta_r^{s_p}$. The measurement model has both time-correlated multipath and white measurement noise processes, plus the effects of correction latency.

The Doppler measurement model for rover from eqn. (2.5), after using the ephemeris data to remove $\mathbf{h}^s \cdot \hat{\mathbf{v}}^s$ and cB^s, is

$$\lambda D_{e_r}^s \doteq \mathbf{h}^s \cdot \mathbf{v}_r + cB_r + \eta_{r,D1}^s. \tag{3.12}$$

The double-differenced Doppler measurement is computed as

$$\lambda dD_r^s = \lambda D_{e_r}^s - \lambda D_{e_r}^{s_p}, \tag{3.13}$$

which yields the measurement model

$$\lambda dD_r^s \doteq (\mathbf{h}^s - \mathbf{h}^{s_p}) \cdot \mathbf{v}_r + d\eta_{r,D1}^s. \tag{3.14}$$

where $d\eta_{r,D1}^s = \eta_{r,D1}^s - d\eta_{r,D1}^{s_p}$ is the white Doppler measurement noise that is correlated between satellites.

3.2 Continent Scale DGNSS Approaches

To enhance the accuracy of GNSS receiver position estimation, the user can compensate the common-mode errors using correction information from external sources. At least three approaches exist to acquire this information: corrections from a local reference station can be directly applied (Local Area DGNSS); GNSS measurements from an array of reference stations could be used to estimate corrections for the local users (Network or Wide Area DGNSS); or, correction information estimated by national or global agencies could be used to construct corrections for the local user (Precise Point Positioning). These methods are discussed in more detail in the following subsections.

3.2.1 Local Area DGNSS Reference Station Network

Local Area DGNSS (LADGNSS) [118,140] uses a reference GNSS receiver near the area of operations to compute a correction that is the sum of the common-mode errors at the reference location. This correction is communicated to roving receivers within a distance D of the reference location for which the correction is deemed to be accurate. This approach works well even for a large number of roving vehicles, each within distance D of the reference station, but does not scale well to large areas.

Let L and W represent the length and width of the continent-sized region for which the corrections are intended to apply. The number of required base stations would be on the order of $\left(\frac{L}{D}\right)\left(\frac{W}{D}\right)$. For example, for the lower forty eight US states $L = 2802$ and $W = 1650$ miles. Depending on the value selected for D, between 475-1850 base stations would be required. Each station would need to be robustly built, the antenna location surveyed, power and data communications installed, and the entire network maintained. The corrections from each station for each satellite would need to be communicated to the master station. If the communication medium provides a data stream across the continental US, then corrections from all reference stations for all satellites would be communicated to all users, who would then use the appropriate correction for the satellites in view at their location.

Such a network of GNSS receivers to implement a continental scale set of *local corrections* is not an efficient use of resources. It is also not reliable in the sense that the loss of any reference station would eliminate corrections applicable to the surrounding region. An alternative approach is discussed in the next section. It makes more efficient use of data, allowing a smaller network, and provides opportunities for enhanced integrity and reliability.

3.2.2 Network DGNSS

Wide-area DGNSS (WADGNSS) systems are designed to cover large, continent-sized regions [46, 76, 78–81, 83, 106]. They rely on data from a network of GNSS receivers dispersed across the region exploiting the spatial and time correlation characteristics of GNSS common-mode errors.

The WADGNSS concept includes a network of reference (or monitor) stations dispersed across the region of interest, one or more master stations (central processing sites), communication of data from the reference stations to the master station(s), and a data link to provide corrections from the master station(s) to users. Each reference station includes one or more GNSS receivers that measure pseudorange and carrier-phase for each frequency of the broadcast signals from all visible satellites. This data is provided to the master station(s). Wide-area DGNSS (WADGNSS) attempts to attain submeter-level position accuracy over the large region while using a fraction of the number of reference stations that a LADGNSS would require to attain the same accuracy within the same coverage region. The general approach, described in more detail in Appendix 7.1, is to parameterize and estimate models for each component of the common-mode pseudorange error.

Satellite Ephemeris and Clock Error. The underlying cause of the ephemeris error in eqn. (2.8) is the satellite position error vector $(\mathbf{p}^s - \hat{\mathbf{p}}^s)$ that can be modeled by three parameters per satellite. Different reference stations are affected by different projections of this satellite position error vector onto their satellite line-of-sight vectors. Given four or more widely separated ground stations whose antenna positions are accurately known, accurate satellite position and clock error estimates can be achieved by combining the concept of a reverse-GNSS solution [22, 82] with sophisticated models to describe the motion of the GNSS satellites over time [27]. Such modeling is a standard method used for orbit determination for many satellite systems, including in the ground network for each GNSS constellation [76].

Ionospheric Delay. With multi-frequency measurements, each receiver at each epoch acquires one measurement per satellite of the slant ionospheric delay at the ionospheric pierce point for that satellite. Combining these slant delay measurements from all satellites and all base stations allows estimation of the parameters of an ionospheric vertical delay model [46, 106]. These vertical delay model parameters are broadcast to the user. The user equipment then computes a vertical ionospheric delay correction for each visible GNSS signal. The vertical delay correction is mapped into a slant delay correction based upon the elevation angle for each visible satellite.

Tropospheric Delay. Tropospheric delays are typically addressed through models (e.g., UNB3 [31], or Black's model [19]) employed at both the reference stations and the roving receiver.

Along with the items mentioned above the WADGNSS approach must calibrate various satellite and receiver hardware biases, and validate signal integrity.

3.2.3 Precise Point Positioning

Precise Point Positioning (PPP) methods are designed to utilize such wide-area network GNSS data products to compute more accurate user positions, without having to install and maintain a GNSS receiver network, master station, and estimation algorithms. Originally PPP methods were designed for post-processing using delayed network data products [8, 18, 154]. As these data products have become available in real-time, the interest has shifted to real-time PPP [30, 60, 91, 95, 101, 147].

After receiving parameters for the various error models, computing per satellite corrections, and applying all these corrections to its own pseudorange and phase measurements, the WADGNSS user equipment computes user position [76]. Approaches exist both for single and two frequency users.

3.2.4 WADGNSS Modeling Agencies

There are various organizations using networks of GNSS stations that provide one or more component of the WADGNSS correction.

International GNSS Service (IGS): IGS is a data service designed to enable high precision positioning using GNSS. Centimeter accuracy has been demonstrated using integer-resolved carrier phase measurements from multi-frequency receivers [56, 88]. IGS uses data from about 300 permanent, continuously-operating reference stations distributed around the world [88]. IGS also has voluntary collaboration (for data sharing) with more than 200 organizations (e.g., JPL) in more than 80 countries. IGS provides differential corrections via the Internet in RTCM Space State Representation (SSR) message format [66]. It is fully functional for GPS and nearing full functionality for GLONASS.

Federal Aviation Association (FAA): FAA has established 38 base stations distributed over the continental US (CONUS) [140]. FAA was responsible for establishing an GPS augmentation system suitable for North-American users. Their existing correction service, called WAAS, is delivered to users via geostationary satellites that also provide additional ranging signals.

European Space Agency (ESA): ESA is responsible for establishing another GNSS augmentation system. ESA has established 40 ground stations across Europe, Africa and North America [140]. The ESA correction called EGNOS is delivered to users via geostationary satellites.

National Oceanic and Atmospheric Admin. (NOAA): NOAA is responsible for providing a near real-time ionospheric Total Electron Content (TEC) map for CONUS users. Approximately 60 base stations were installed and maintained by the agency to provide a data source for their system [13].

The described agencies provide DGNSS corrections accessible by public entities free of cost. There are also private agencies (e.g., Jet Propulsion Lab (JPL), Trimble) that provide their own functioning WADGNSS services for a user fee.

To illustrate the issues and challenges related to WADGNSS model parameter estimation the elements of one approach are described in Appendix 7.1.

3.2.5 Existing WADGNSS Services

Numerous agencies have been working to establish network DGNSS services for almost 30 years [46, 78–83, 106]. The established services can be categorized into two groups based on their communication channels: geostationary satellites or internet.

Satellite Based Augmentation Systems SBAS is the generic name for any augmentation system that has implemented WADGNSS using satellites as communication channels [97, 140]. This augmentation service can provide ranging, integrity and correction information for users in different geographical locations. Some versions of SBAS are described below.

Wide Area Augmentation Service (WAAS): WAAS was developed by the US FAA to provide correction data for the GPS system [140]. The WAAS system is established based on two segments: (a) Ground segment, and (b) Space segment. The ground segment consists of all reference stations installed in CONUS and Hawaii. The reference station data is sent to the Master stations which compute the corrections and send them to Ground Uplink Stations (GUS), which then transmit to four satellites for rebroadcast to the users.

European Geostationary Overlay Service (EGNOS): This service was developed by ESA specifically for users with multi-GNSS receivers [140]. It provides correction services for the GPS, GLONASS and Galileo systems. The system has two segments: (a) ground segment with 40 base stations in Europe, Africa and North America, and (b) space segment with 3 geostationary satellites.

Multi-functional Satellite Augmentation Service (MSAS):

This service was developed in Japan. It has 4 ground stations in Japan, Hawaii and Australia and 2 geosynchronous communication satellites [134].

Starfire: This is a private fee-based correction service. The system was developed by John Deere's NavCom and precision farming groups.

There are additional augmentation services that are not yet fully functional, including:

- *GPS Aided Geo Augmented Navigation System (GAGAN)* under development by India.
- *System for Differential Corrections and Monitoring (SDCM)* under development by Russia.

Internet Based Augmentation System There are agencies working on computing network DGNSS services to be distributed via the Internet. For example, IGS has been working since 1994 to establish a real-time, precise GNSS positioning service [88]. The DGNSS correction would be delivered in RTCM SSR format [66], which consists of many message types containing information about precise orbit, clock, ionosphere, and satellite hardware biases.

3.3 WADGNSS Implementation

This section describes data sources, methodology, and performance analysis related to implementing a WADGNSS service.

3.3.1 Data Sources

A major issue in the implementation of a WADGNSS network is the reliable real-time collection of GNSS data from multi-frequency receivers well-distributed across the USA.

Various private organizations (e.g., Trimble, JPL) have established and maintained an array of reference stations across the country, but the data from these reference stations are not accessible by public users. Alternatively, some public organizations (e.g., NOAA) have spatially distributed reference stations, but real-time free access is limited to only a few reference stations. Other public organizations (e.g. Plate Boundary Observatory (PBO), Scripps Orbit and Permanent Array Center (SOPAC)) provide freely accessible real-time data, but their spatial distribution does not currently cover the entire CONUS.

Table 3.1 summarizes information related to a few examples of available sources for reference station data in the CONUS. All the sources listed as public (including all NOAA sites) allow delayed downloading of data for post-processing.

Table 3.1: Summary of Real-time Reference Station Networks.

Entities	Access	Free	Coverage
PBO	Public	Y	West coast
NOAA	Public Private	Y N	Limited USA
FRPN	Public	Y	Florida
Trimble	Private	N	USA
JPL	Private	N	Global

For an entity that desires to communicate real-time WADGNSS to automotive user there are various available approaches:

1. Compute its own WADGNSS information using data from:
    (a) an entirely new network of reference stations installed and maintained by the entity or its contractor;
    (b) existing free sources; or
    (c) existing sources that charge a fee.

2. Collaborate with entities that already computed the components of WADGNSS corrections to distribute them through alternative communication channels.

Option 1 requires development of talent, methods, and algorithms. It also requires selection of a real-time reference station data delivery approach and may also run into intellectual property issues. Option 2 allows an entity with a well established expertise in data communications to focus on that strength, avoids intellectual property issues, avoids the need to acquire raw GNSS reference data in real-time, and relies on the well developed expertise of others for the estimation of model parameters.

3.3.2 WADGNSS Implementation Strategies

Given reference station data, WADGNSS modeling entities estimate model parameters for the three-dimensional ephemeris error and clock offset for each satellite, plus ionospheric time delay model parameters that can be communicated to user receivers in real-time. The algorithms may also estimate various additional quantities: reference receiver clock error, tropospheric delay, hardware biases, and carrier phase integer ambiguities. These quantities are not communicated to the user in real-time. The reference receiver clock error and integer ambiguities are nuisance parameters that must be estimated to achieve the specified accuracy in the desired model parameters, but are not themselves useful. The hardware delays are very slowly changing ($4.23e^{-4}$ ns/day or 0.13 mm/day), so they can be communicated at low rates (e.g., every 10 days).

The process can be summarized as follows: 1) reference stations at known locations collect GNSS pseudoranges and carrier phases (if available) from all satellites in view; 2) observations or processed observations (e.g., ionospheric-free pseudorange and ionospheric delay measurements

Table 3.2: Summary of WADGNSS Strategies.

Strategy	Number User Freqs.	Number reference Freqs.	Requirements
A	1	1	More reference stations than B and C
B	1	2	Fewer reference stations than A
C	2	2	More expensive user equipment Fewer reference stations than A

(if available)) are sent to the master station; 3) the master station computes a state vector that includes the desired model parameters; 4) the model parameters are transmitted to users; 5) users calculate corrections using the model parameters and tropospheric model, then apply the corrections to their measured observations, resulting in improved navigation accuracy. Various WADGNSS techniques have been proposed in the literature [14, 22, 78–81, 103].

WADGNSS technique can be categorized according to the number of frequencies required for users and reference stations, which has implications for the estimation algorithm at the master station [81]:

- **Strategy A**: This approach allows both the reference stations and users to employ single-frequency receivers. Because the reference station is single frequency it cannot provide ionospheric time measurements. This strategy uses an ionospheric model (e.g. Klobuchar model) to estimate and remove a portion of the ionospheric time delay from the reference station measurements prior to they are used by the master station. The master station estimates the three-dimensional ephemeris error vectors, the satellite clock errors and the reference receiver clock errors in one large filter using only the (ionospheric corrected) pseudorange measurements from all reference stations. The convergence time of the master station filter is stated as 2-4 hrs [81]. To use Strategy A for position estimation, requires the user to have an ionospheric model or Total Electron Content (TEC) map from another source. Position estimation accuracy is not stated in [81].

- **Strategy B**: This method requires the reference stations to use dual-frequency receivers, while the users can employ single-frequency (or two-frequency) receivers. With two frequencies, the reference station can construct measurements of ionospheric delay. Using these ionospheric delay measurements, allows a large estimation problem to be split into two smaller problems. Estimation of the vertical TEC map parameters using ionospheric delay measurements is one process. Estimation of the three-dimensional ephemeris error vectors, the satellite clock errors, and the reference station receiver clock errors is a separate process [81]. Relative to Strategy A, Strategy B has a lower computational load, uses fewer reference stations, and provides an vertical TEC map. For a rover using L1 carrier smoothed pseudorange measurement, [118] demonstrates position accuracy of 1.1 m.

- **Strategy C**: This method requires both reference stations and users to utilize dual-frequency receivers. In this case, ionospheric parameters do not need to be estimated in the master station, and as a result, only three-dimensional ephemeris error vectors and satellite clock errors are estimated. Compared to Strategy B, Strategy C has smaller computational load. It achieves the best accuracy among the aforementioned strategies, as this method removes ionospheric delay completely [80]. For a rover using L1 and L2 carrier smoothed pseudorange measurements, [81] demonstrates position accuracy of 0.71 m.

While Strategy C has the best reported accuracy and reduced computational load, the current project focuses on users with single frequency receivers.

Table 3.3: Local and Wide-Area Differential GNSS error budgets.

Error Type	LADGNSS Error Budget, m	WADGNSS Error Budget, m	Model Source
Ephemeris	0.4	0.05	IGS
Satellite clock	0.2	0.09	IGS
Ionospheric delay	0.5	0.40	USTEC
Tropospheric	0.3	0.05	UNB3M
Satellite hardware bias	N/A	0.9	CODE
Receiver noise	0.2	0.20	
Multipath	0.1	0.10	
UERE, rms	0.8	0.48	

Therefore, one implementation of Strategy B is reviewed and described extensively in Appendix of [124].

3.3.3 Related Issues and Error Budget

A comparison of the user equivalent range error (UERE) that a user can achieve using Local or Wide-Area DGNSS is summarized in Table 3.3 [118]. The first column is the error type. The second column shows the stated accuracy to which each common-mode error type can be compensated using LADGNSS [118]. The third column shows the reported accuracy to which the WADGNSS model states the common-mode error can be corrected. The model source is listed in the fourth column. The accuracy stated for the orbit and clock corrections is from [30]. The accuracy stated for the ionospheric model (i.e., vertical TEC) is from [13]. The accuracy stated for tropospheric model is from [96]. The noncommon-mode errors' (multipath and receiver noise) nominal values are obtained from [118]. Multipath error varies as a function of environment (e.g. urban, rural, open sky, obstructed view) and vehicle motion platform (stationary and moving). Receiver noise differs for both receiver and measurement type.

The UERE is converted to a horizontal position error by multiplication by the horizontal dilution of positions (HDOP), which for GPS with at least 6 satellites in view typically ranges from 1-2. Therefore, based on the last row of Table 3.3, rms horizontal position error is predicted to be 0.8 - 1.6 m for LADGNSS and 0.48 - 0.96 m for WADGNSS.

3.4 Real-time PPP Approach

Many entities (IGS, JPL, WAAS) have investigated and established WADGNSS systems [46, 79–81, 106, 110]. Various services now provide real-time access to the products of their WADGNSS: TEC maps, satellite position and clock corrections, and satellite inter-frequency biases. These services enable real-time Precise Point Positioning (PPP).

This appendix discusses data sources and methods for computing: satellite orbit corrections and precise ephemeris; satellite clock corrections; ionospheric corrections; tropospheric corrections; and satellite hardware bias corrections. It also summarizes reported accuracy for each.

Table 3.4: IGS product for precise satellite orbit and clock correction:

Product	Communicaton period		Accuracy		latency
	Orbit	Sat. Clock	Orbit	Sat.Clock	
Real-time	5-60 sec	5 sec	5.0 cm	300 ps	25 sec
Ultra-Rapid (Predicted Half)	15 min	15 min	5.0 cm	3 ns	predicted
Ultra-Rapid (Observed Half)	15 min	15 min	3.0 cm	150 ps	3-9 hrs
Rapid	15 min	5 min	2.5 cm	75 ps	17-41 hrs
Final	15 min	30 sec	2.0 cm	75 ps	12-18 days

Satellite and Clock Orbit Corrections. Satellite ephemeris/orbit error is the difference between the satellite's true position p^s and the position $\hat{p}^s$ computed using ephemeris data. This error develops is due to uncertainty in the gravitational model, inaccuracy of the orbit representation and inadequately modeled surface forces on the satellites (e.g., solar radiation, particles of the Earths atmosphere and air drag).

Although GPS satellites have stable atomic clocks, all clocks drift relative to each other. The main distinction of higher quality clocks is that they drift more slowly, yet it is not possible to maintain synchronization of the satellite clocks with GPS time, which results in satellite clock biases. The navigation message provides parameters to predict the clock biases $c\hat{t}^s(t)$, but there will still be residual clock biases $c\delta t^s(t)$ that range from 1-3 meters.

3.4.1 Satellite Orbit

IGS has been working on establishing precise orbit and clock correction service since 1990. Currently the service provides multiple versions of these corrections. Table 3.4 provides a description of the different data products for orbit and clock corrections. It includes communication period, reported accuracy, and latency information.

Computation

The satellite position $\hat{\mathbf{p}}^s(t)$ and velocity vectors $\dot{\hat{\mathbf{p}}}^s(t)$ in ECEF frame are computed from the broadcast ephemeris. For the IGS-RTS service, the satellite orbit correction parameters $\delta\mathbf{O}_0$ and rate $\delta\dot{\mathbf{O}}_0$ are provided in Antenna Phase Center coordinates (i.e., APC frame) along with a reference time t_0 every 60 seconds. Given these items, the correction computation involves four steps [66]:

1. The satellite orbit correction parameters $\delta\mathbf{O}_0$ and rate $\delta\dot{\mathbf{O}}_0$ are provided every 60 seconds along with a reference time t_0. The orbit correction at any time t is computed as

$$\delta\mathbf{O}(t) = \delta\mathbf{O}_0 + \delta\dot{\mathbf{O}}_0\,(t - t_0). \tag{3.15}$$

In APC-frame, the vector $\delta\mathbf{O} = \begin{bmatrix} \delta O_r & \delta O_a & \delta O_c \end{bmatrix}^\top$ has radial, along-track, and cross-track components.

2. The radial $\mathbf{e}_r$, along $\mathbf{e}_a$, and cross-track $\mathbf{e}_c$ unit vectors in the ECEF frame are computed as

$$\mathbf{e}_a = \frac{\dot{\hat{\mathbf{p}}}^s}{\|\dot{\hat{\mathbf{p}}}^s\|}, \ \mathbf{e}_c = \frac{\hat{\mathbf{p}}^s \times \dot{\hat{\mathbf{p}}}^s}{|\hat{\mathbf{p}}^s \times \dot{\hat{\mathbf{p}}}^s|}, \ \mathbf{e}_r = \mathbf{e}_a \times \mathbf{e}_c. \tag{3.16}$$

3. The orbit correction $\delta\mathbf{O}(t)$ is transformed from APC frame to ECEF frame as

$$\delta\mathbf{p}^s(t) = \begin{bmatrix} \mathbf{e}_r \ \mathbf{e}_a \ \mathbf{e}_c \end{bmatrix} \delta\mathbf{O}(t). \tag{3.17}$$

4. The precise orbit $\hat{\mathbf{p}}^{s_p}$ is computed as

$$\hat{\mathbf{p}}^{s_p}(t) = \hat{\mathbf{p}}^s(t) - \delta\mathbf{p}^s(t). \tag{3.18}$$

After the computation of precise orbit $\hat{\mathbf{p}}^{s_p}(t)$, it can be used in two ways that are nearly the same. First, for a user with access to the receiver navigation code, the precise satellite location can be used for computing the estimated range $R(\hat{\mathbf{p}}_r, \hat{\mathbf{p}}^{s_p}) = \|\hat{\mathbf{p}}_r - \hat{\mathbf{p}}^{s_p}\|$ and satellite-to-receiver unit vector. Second, for a user supplying corrections to a receiver, the receiver will still use $\hat{\mathbf{p}}^s$, the ephemeris portion of the corrections $\hat{E}^{s_p}$ would be

$$\hat{E}^{s_p} = \frac{(\hat{\mathbf{p}}_u - \hat{\mathbf{p}}^{s_p})}{\|\hat{\mathbf{p}}_u - \hat{\mathbf{p}}^{s_p}\|} (\hat{\mathbf{p}}^s - \hat{\mathbf{p}}^{s_p}) \tag{3.19}$$

where $\hat{\mathbf{p}}_u$ is the approximate user location.

3.4.2 Satellite Clock

IGS-RTS data products provide satellite clock corrections using three polynomial parameters (a_{c_0}, a_{c_1}, a_{c_2}) and the message reference time is t_0. As shown in Table 3.4, these parameters are sent every 5 seconds. The correction at time t is computed using the following equation [66]:

$$c\delta t^s(t) = a_{c_0} + a_{c_1}(t - t_0) + a_{c_2}(t - t_0)^2. \tag{3.20}$$

The clock correction $c\delta t^s(t)$ is computed in meters. The equation for the precise satellite clock ct^{s_p} is

$$ct^{s_p}(t) = ct^s(t) + c\delta t^s(t). \tag{3.21}$$

3.4.3 Ionosphere Delay

The amount of ionospheric delay incurred by a GNSS signal depends on the number of free electrons or ions existing along the signal path. This measure is referred to as the Total Electron Content (TEC) which is measured in Total Electron Content Units (TECU's), where $1\ TECU = 1 \times 10^{16}\ TEC$ means there are 1×10^{16} electrons in a $1\,m^2$ cylinder around the signal path. This delay is dependent on the frequency of the carrier signal; therefore, it can be measured and removed by a user with a multi-frequency receiver. In a network GNSS approach measurements from across the network can be combined to calibrate a TEC map, as described in Appendix 7.1. A single frequency receiver cannot calibrate the ionospheric delay itself, but can incorporate ionospheric models from external sources.

Data Sources and Reported Accuracy. Table 3.5 summarizes a few example ionospheric delay map products [30]. The table includes reported accuracy, sampling period, map resolution and product latency. Some frequently used ionospheric delay products are:

- **Klobuchar Model:** The ionospheric delay model that is available to all GPS users as part of the broadcast navigation message is the Klobuchar model [86]. The modeling effort included

Table 3.5: Ionospheric Delay Map Products.

Product	Reported accuracy, TECU	Broadcast interval	Latency	Resolution longitude, deg	Resolution latitude, deg
IGS Final Product	2-8	2 hours	11 days	5	2.5
IGS Rapid Product	2-9	2 hours	$\leq$ 24 hours	5	2.5
US-TEC	2.4	15 min	Real-time	1	1

an assessment of expected accuracy versus the number of coefficients. The broadcast model uses 8 coefficients to achieve for 50% correction accuracy goal. Increasing this number of coefficients would only remove 70% to 80% RMS of the ionospheric effects.

- **Global Ionosphere Maps (GIM):** GIM represents a tool to monitor global ionospheric patterns. It provides the instantaneous snapshots of the global TEC distribution [106]. This product was developed by IGS Ionosphere Working Group (Iono-WG) established on May 1998. Currently four IGS Ionosphere Associate Analysis Centers (IAACs) provide data to generate GIMs on a daily basis. GIM produces a 2-dimensional ionosphere TEC map that corresponds to a 450 km ionospheric shell height. The IGS final GIMs are provided in Ionosphere Map Exchange (IONEX) format.

- **US Total Electron Content (US-TEC):** USTEC is a service that distributes a TEC map for the USA. The product was developed through a collaboration between the Space Weather Prediction Center (SWPC), the National Geodetic Survey (NGS), the National Centers for Environmental Information (NCEI), and the Global Systems Division (GSD) [13, 55].

Methodology

For single-frequency real-time users in North America, US-TEC is the most suitable ionospheric delay product. US-TEC (and other services) provides vertical TEC values for a uniform grid of point locations at a specified broadcast interval which can extend from minutes to hours (see Table 3.5). The user computes a TEC value for its specific location by interpolating between the provided values in both space and time [42]. Linear temporal interpolation is sufficient. Spatial interpolation can be performed in different ways. Given the values of the vertical TECU values at the grid points, linear spatial interpolation approaches take the form of eqn. (7.12):

$$\widehat{TEC}_v(\mathbf{p}^s_{p_u}) = w((\mathbf{p}^s_{p_u})\hat{\mathbf{I}}^G. \tag{3.22}$$

This interpolation is based on the pierce point $\mathbf{p}^s_{p_u}$, which the user computes using the satellite and receiver locations [119]. The discussion in Appendix 7.1 includes an example distance weighted approach. Spatial interpolation provides the vertical total electron count at the pierce point, which is converted to slant delay using eqns. (7.1) and (7.8):

$$\hat{I}^s_{L1} = \frac{40.3}{f^2_{L1}}\, F(\psi^s_r)\, \widehat{TEC}_v(\mathbf{p}^s_{p_r}) \tag{3.23}$$

The factor $F(\psi^s_r)$ is the ionospheric obliquity factor

$$F(\psi^s_r) = \frac{1}{\sin(\psi^s_{p_r})} = \sqrt{1 - \left[\frac{r_e \cos(\psi^s_r)}{r_e + h_m}\right]^2} \tag{3.24}$$

where ψ^s_r is the elevation angle for satellite s at receiver r, $\psi^s_{p_r}$ is the local elevation angle at the pierce point p_p, r_e is the average radius of the Earth, and h_m is the height of the maximum electron density (assumed herein to be 350 km).

Table 3.6: Tropospheric Delay Model Accuracy.

Model	UNB	UNB3M	EGNOS	IGGtrop
Accuracy (cm)	6-10	5.4	5.7	4.4
Location	North America	North America	Europe	Global

3.4.4 Troposphere Delay

The troposphere is the lowest layer of the atmosphere extending to about 50 km above the surface of Earth. It is a non-ionized and non-dispersive medium, so usage of multiple frequency measurements cannot eliminate tropospheric delay. This delay is affected by satellite elevation angle, receiver altitude, atmospheric temperature, pressure and humidity. The tropospheric delay can be divided into two parts: the dry/hydrostatic part and the wet part. About 90% of the total tropospheric delay is contributed by the dry component and 10% by the wet component.

Methodology

Standard tropospheric delay models for satellite measurement T^s have the form:

$$T^s = d^s_{dry}\ M^s_{dry} + d^s_{wet}\ M^s_{wet}. \tag{3.25}$$

The symbols d^s_{dry} and d^s_{wet} are the tropospheric Zenith Path Delay (ZPD) caused by the dry and wet components, respectively. The symbols M^s_{dry} and M^s_{wet} are the mapping functions that convert the ZPD dry and wet components from zenith (or vertical) to slant delays based on satellite elevation at the user location.

Literature and Reported Accuracy: The literature contains a variety of ZPD models, for example: Hopfield [72], Saastamoinen [129]. These models depend on various atmospheric parameters: receiver altitude, temperature, pressure, and humidity. Therefore, local sensors (e.g., barometer, hygrometer, thermistor) are necessary to compute tropospheric delay accurately from these models. In addition to tropospheric ZPD, there are also many mapping functions to compute slant tropospheric delay: Chao [28], Herring [17], Lanyi [94], Davies [32] and Niell mapping functions [114].

Recently, several entities have proposed newer hybrid tropospheric models combining a ZPD model and mapping function [96, 152] that do not require additional sensors; instead, additional lookup tables are provided for computing typical atmospheric parameters (i.e., temperature, pressure and humidity) for a specific location at a specific date and time. Example models are: UNB [96], UNB3M [48], EGNOS [77], and IGGtrop [98]. Different characteristics of these models are summarized in Table 3.6, based on information from [152].

Description of UNB3M: For this research project, the UNB3M model was selected as it is specifically designed for users in North America. The UNB model has been developed by researchers of University of New Brunswick, Canada [96]. The model consists of the Saastamoinen zenith delay model, the Niell mapping functions, and a look-up table to compute predicted values for temperature, pressure and water vapor pressure varying with respect to date, time, latitude and height. UNB3M model is the modified version of UNB model. In this model, instead of water vapor pressure the look-up table contains relative humidity. The model computes dry and wet delay components using look-up table values and Niell mapping functions.

3.4.5 Satellite Hardware Bias

The measurement models in eqns. (2.1-2.4) and the WADGNSS approach is Appendix 7.1 did not account for delays due to satellite hardware that may be different for code, phase, or different frequencies. These delays, referred to as satellite hardware biases or Differential Code Biases (DCB), can be as large as 12 nanoseconds. This bias are constant unless there is a satellite hardware substitution. The biases can be estimated in a network WADGNSS approach or can be downloaded from various sources.

Data Sources: Two sources for the DCB parameters are:

- The Crustal Dynamics Data Information System provides the DCB in MGEX data format. The file can be found at the URL: “ftp://cddis.nasa.gov/gnss/products/bias/”.
- IGS-RTS provides the DCB as a message in RTCM format [91].

Methodology: For the L1 C/A pseudorange measurement the satellite DCB $cb^s_{L1,\rho}$ is:

$$cb^s_{L1,\rho} = -T_{GD} + ISB_{C1,P1} \tag{3.26}$$

where $ISB_{C1,P1}$ is the delay of L1 C/A signal with respect to L1 P signal and T_{GD} is the group delay parameter in the navigation message. The group delay represents the time difference from generation to transmission of the P signal.

3.4.6 PPP Compensated GNSS Measurements

The PPP approach described herein, converts the common-mode error information into a correction for the L1 pseudorange measurement of satellite s:

$$\hat{k}^s_r = \hat{E}^{s_p} - c\hat{t}^{s_p} + \hat{I}^s_{L1} + \hat{T}^s - c\hat{b}^s_{L1,\rho}, \tag{3.27}$$

suitable for the users location. The PPP common-mode error correction terms are:

- Precise orbit correction $\hat{E}^{s_p}$ that is computed from IGS-RTS using eqn. (3.19).

- Precise satellite clock correction $c\hat{t}^{s_p}$ that is computed from IGS-RTS using eqn. (3.21).
- Slant ionospheric delay for L1 users $\hat{I}^s$ that is computed from USTEC's TEC map using eqn. (3.23).
- Slant tropospheric delay $\hat{T}^s$ is computed from the UNB3M model using eqn. (3.25).
- Satellite hardware bias for the L1 user $c\hat{b}^s$ that is computed from CODE using eqn. (3.26).

Then, the common-mode error compensated pseudorange measurement $\hat{\rho}_r^s$ is computed as follows:

$$\hat{\rho}_r^s = \rho_{r,L1}^s - \hat{k}_r^s, \tag{3.28}$$

The measurement model for $\hat{\rho}_r^s$ is:

$$\hat{\rho}_r^s \doteq R(\mathbf{p}_r, \hat{\mathbf{p}}^s) + ct_r + cb_{r_{L1,\rho}} + F(\psi_r^s)A_v + M_r^s + \delta\eta_{r,\rho}^s. \tag{3.29}$$

The symbol A_v represents the residual vertical atmospheric delay after PPP compensation. The obliquity coefficient $F(\psi_r^s)$ is defined in eqn. (7.9). Because the atmosphere pierce points for all in-view satellites are within 10 degs of the rover zenith point. The error term $\delta\eta_{r,\rho}^s$ is:

$$\delta\eta_{r,\rho}^s \doteq \eta_{r,\rho}^s + \delta k_r^s. \tag{3.30}$$

where δk_r^s is the residual common-mode error remaining after PPP correction compensation.

3.4.7 Single-Differenced PPP Measurement Model

PPP corrections compensate for the common-mode errors that affect the pseudorange measurement. The receiver clock biases can be eliminated by single differencing (See Section 8.8.3 in [49]). In single-differencing, one satellite, called the pivot satellite, has its PPP-compensated measurement subtracted from all the others. This operation removes clock bias errors (i.e., two states from the model) at the cost of one fewer measurement per epoch and causing the noise on all single-differenced measurements per epoch to be correlated.

For the results herein, the pivot satellite (denoted as s_p) will always be chosen as the one with the highest elevation angle. The single-differenced pseudorange measurement $\Delta\rho^s$ is computed as

$$\Delta\rho^s = \hat{\rho}_r^s - \hat{\rho}_r^{s_p}. \tag{3.31}$$

The corresponding measurement model is

$$\Delta\rho^s \doteq R(\mathbf{p}_r, \hat{\mathbf{p}}^s) - R(\mathbf{p}_r, \hat{\mathbf{p}}^{s_p}) + F(\psi_r^s)A_v - F(\psi_r^{s_p})A_v + dM_r^s + d\eta_{r,\rho}^s, \tag{3.32}$$

where $dM_r^s = M_r^s - M_r^{s_p}$ and $d\eta_{r,\rho}^s = \delta\eta_{r,\rho}^s - \delta\eta_{r,\rho}^{s_p}$ are the residual time-correlated multipath and white measurement noise.

Single-differencing of the Doppler measurement is computed as

$$\lambda\Delta D^s = \lambda\hat{D}_r^s - \lambda\hat{D}_r^{s_p}, \tag{3.33}$$

which yields the measurement model

$$\lambda\Delta D^s \doteq (\mathbf{h}_r^s - \mathbf{h}_r^{s_p}) \cdot \mathbf{v}_r + d\eta_{r,D}^s. \tag{3.34}$$

where $d\eta_{r,D}^s = \eta_{r,D}^s - \eta_{r,D}^{s_p}$ is the white Doppler measurement noise that is correlated between satellites.

Define the vector of two measurements per satellite at epoch k as:

$$\mathbf{z}_k^s = \mathbf{h}^s(\mathbf{x}_k) + \eta_k^s, \tag{3.35}$$

with

$$\mathbf{z}_k^s = \begin{bmatrix} \Delta\rho_k^s \\ \\ \Delta D_k^s \end{bmatrix} \text{ and } \mathbf{h}^s(\mathbf{x}_k) = \begin{bmatrix} R(\mathbf{p}_r, \hat{\mathbf{p}}_k^s) - R(\mathbf{p}, \hat{\mathbf{p}}_k^{s_p}) + (F(\psi_r^s) - F(\psi_r^{s_p}))A_v \\ \\ (\mathbf{h}_r^s - \mathbf{h}_r^{s_p}) \cdot \mathbf{v}_r \end{bmatrix}$$

where receiver antenna position $\mathbf{p}_r$ and velocity $\mathbf{v}_r$ will be sub-vectors of the state vector $\mathbf{x}$. The measurement noise is $\eta_k^s \sim \mathcal{N}(0, \mathbf{R}_z)$ with

$$\mathbf{R}_z = \begin{bmatrix} R_p^s + R_p^{s_p} & 0 \\ \\ 0 & R_D^s + R_D^{s_p} \end{bmatrix}.$$

The vector of measurements at epoch k corresponding to the model in eqn. (3.35) concatenates the measurements per satellite: $\mathbf{z}_k = [\mathbf{z}_k^1, \ldots, \mathbf{z}_k^m]^\top$ with $\mathbf{h}(x) = [\mathbf{h}^1(\mathbf{x}), \ldots, \mathbf{h}^m(\mathbf{x})]^\top$, where m is the number of available GNSS measurements minus one.

Chapter 4

IMU Measurement

An IMU consists of two triads of perpendicularly mounted inertial sensors: (a) gyroscopes and (b) accelerometers. The accelerometers measure platform acceleration relative to an inertial frame-of-reference, resolved in the accelerometer frame-of-reference (i.e., along the accelerometer sensitive axis). The gyros measure the platform angular rate relative to the inertial frame-of-reference, as resolved in gyro frame (i.e., along the gyro sensitive axis). The gyro measurements are transformed into the platform frame using the (usually) constant calibration matrix. The platform frame gyro measurements are processed to maintain the platform-to-navigation frame rotation matrix. Finally, the platform-to-navigation frame rotation matrix is used to transform the accelerometer measurements into the navigation frame where they are processed to determine navigation frame velocity and position. For designing an optimal estimator, the measurement and noise model of these sensors should be studied extensively.

4.1 Measurement Model

The measurement model of accelerometers and gyroscopes are:

$$\mathbf{u}_g^b \doteq \omega_{ib}^b + \mathbf{z}_g. \tag{4.1}$$

$$\mathbf{u}_a^b \doteq \mathbf{a}_{ib}^b - \mathbf{g}^b + \mathbf{z}_a. \tag{4.2}$$

The term $\mathbf{u}_g^b$ denotes the gyroscope measurement and ω_{ib}^b is the angular rate in body frame respectively. The term $\mathbf{u}_a^b$ denotes accelerometer measurement, $\mathbf{a}_{ib}^b$ is the acceleration and $\mathbf{g}^b$ denotes local gravity vector in body frame respectively. In the above equation, $\mathbf{z}_g$ and $\mathbf{z}_a$ represent stochastic errors. This implementation assumes

$$\mathbf{z}_g \doteq \mathbf{b}_g + \gamma_g. \tag{4.3}$$

$$\mathbf{z}_a \doteq \mathbf{b}_a + \gamma_a. \tag{4.4}$$

The error term $\mathbf{b}_g$ is the gyroscope bias and γ_g is a Gaussian white noise with PSD $\sigma_{\gamma_g}^2$. The accelerometer bias is denoted by $\mathbf{b}_a$ and γ_a is a Gaussian white noise with PSD $\sigma_{\gamma_a}^2$. The specific force is defined as:

$$\mathbf{f}_{ib}^b \doteq \mathbf{a}_{ib}^b - \mathbf{g}^b. \tag{4.5}$$

The sensor bias ($\mathbf{b}_g$ and $\mathbf{b}_a$) can be adequately modeled as first order Gauss Markov process for implementation:

$$\dot{\mathbf{b}}_g \doteq \lambda_g \mathbf{b}_g + \varepsilon_g \tag{4.6}$$

$$\dot{\mathbf{b}}_a \doteq \lambda_a \mathbf{b}_a + \varepsilon_a \tag{4.7}$$

where ε_g and ε_a are Gaussian white noise process with PSD of $\sigma_{b_g}^2$ and $\sigma_{b_a}^2$ respectively, and λ_g and λ_a are the time constant parameters of the correlated noise of the sensors.

4.2 Sensor Error Model

The data fusion system that combines the IMU and aiding sensor data will be able to achieve improved performance by real-time calibration if it incorporates an IMU error model in state-space form. The PSD and time correlation parameters of the aforementioned IMU sensor's stochastic noise can be found either in the manufacturer's technical specification sheet or it can be extracted from the Allan Standard Deviation (ASD) plot. The manufacturer may itself provide an ASD plot [54]. This section reviews the Allan Variance and its relationship to the power spectral density.

4.2.1 Allan Variance

The Allan Variance is a well-known time domain analysis technique, which was originally developed to study the frequency stability of oscillators [6, 15]. Due to its relative simplicity, it has been successfully adopted to model IMU stochastic errors [1, 2, 35, 69, 107, 111, 120, 136, 151].

Let $D = \{\tilde{u}_i\}_{i=1}^{L}$ be a (detrended) set of specific force (or angular rate) data, measured at a constant sampling interval T for a stationary IMU. At each time instant $t_i \in [T, 2T, \ldots, (L-n)T]$, form a group (cluster) of n consecutive data points (beginning at t_i). The duration of each such cluster is $\tau = nT$. For each such n-point cluster, compute the average value $\bar{u}_i(\tau) = \frac{1}{n}\sum_{j=1}^{n} \tilde{u}_{i+j}$. The equation to compute the AV, as the average of the $(L-2n)$ cluster differences for each specific value of τ, is [1, 6],

$$\sigma_u^2(\tau) = \frac{1}{2(L-2n)} \sum_{i=1}^{L-2n} [\bar{u}_{i+n}(\tau) - \bar{u}_i(\tau)]^2 \tag{4.8}$$

The AV is computed for values of the cluster time τ ranging from T to $LT/2$.

Since some IMU's (especially those that are high-grade) provide the integral of specific force (or angular rate), denoted as $\tilde{\theta}_i$, we may alternatively define $\bar{u}_i(\tau)$ as

$$\bar{u}_i(\tau) = \frac{\tilde{\theta}_{i+n} - \tilde{\theta}_i}{\tau} \tag{4.9}$$

Substitution of eqn. (4.9) in eqn. (4.8) yields,

$$\sigma_u^2(\tau) = \frac{1}{2\tau^2(L-2n)} \sum_{i=1}^{L-2n} (\tilde{\theta}_{i+2n} - 2\tilde{\theta}_{i+n} + \tilde{\theta}_i)^2 \tag{4.10}$$

which is an alternative formula for estimating the AV [1].

4.2.2 PSD and Allan Variance

The AV is related to the two-sided power spectral density by [1],

$$\sigma_u^2(\tau) = 4\int_0^\infty S_u(f)\frac{\sin^4(\pi f \tau)}{\pi f \tau}df. \tag{4.11}$$

There is no inversion formula for eqn. (4.11) (e.g., see [138]).

When the power spectrum is represented as a power series in frequency f, it has the form,

$$S_u(f) = \cdots + N^2 + \frac{B^2}{2\pi f} + \frac{K^2}{(2\pi f)^2} + \cdots, \tag{4.12}$$

Table 4.1: Dominant Errors in Consumer Grade IMU's

Noise type (Coef.)	Coef. unit	Allan Variance Acc: $(\mathrm{m/s^2})^2$ Gyro: $(\mathrm{deg/s})^2$	PSD Acc: $\mathrm{m^2/s^3}$ Gyro: $\mathrm{deg^2/s}$
Ang./Vel. random walk, N	Acc: $\mathrm{m/s^{3/2}}$ Gyro: $\mathrm{deg/s^{1/2}}$	$\frac{N^2}{\tau}$	N^2
Bias instability, B	Acc: $\mathrm{m/s^2}$ Gyro: deg/s	$\frac{2B^2 ln2}{\pi}$	$\frac{B^2}{2\pi f}$
Rate/Accel. random walk, K	Acc: $\mathrm{m/s^{5/2}}$ Gyro: $\mathrm{deg/s^{3/2}}$	$\frac{K^2\tau}{3}$	$\left(\frac{K}{2\pi f}\right)^2$

where only the terms that are of interest herein have been kept. These relate to the dominant errors in consumer grade IMU's. Assuming that each of these three types of errors are mutually independent, each can be modeled by its own state-space process with its own independent driving noise. However, it is impossible to exactly replicate the term $\frac{B^2}{2\pi f}$ with a finite-dimensional state-space model because its power spectrum is not an even function of $s = j2\pi f$.

4.2.3 Continuous-time State Space Models

This section considers the development of continuous-time state-space models able to reproduce (approximately) the power spectral density of eqn. (4.12) and ASD plots. The overall model will have the form,

$$z(t) = z_N(t) + z_B(t) + z_K(t). \tag{4.13}$$

where $z_N(t)$, $z_B(t)$ and $z_K(t)$ are the IMU stochastic errors associated with coefficients N, B, and K, respectively. Herein, a general model is described as stochastic error, For accelerometers and gyroscopes, notations will be z_a and z_g respectively instead of z.

4.2.4 Angular/Velocity Random Walk Errors: $z_N(t)$

The term N^2 in eqn. (4.12) is constant as a function of frequency f which corresponds to the power spectrum of white noise [23]. Therefore,

$$z_N(t) = \omega_N(t) \tag{4.14}$$

where $\omega_N(t)$ is white Gaussian random noise with power spectral density Q_N. When N is known, Q_N can be computed using Table 4.1,

$$Q_N = N^2. \tag{4.15}$$

In the literature and on manufacturer specifications, this type of error is called *angular random walk* error for gyros and *velocity random walk* error for accelerometers. Applying the transformation in eqn. (4.11) to $S_{z_N}(f) = N^2$ yields error variance [1],

$$\sigma^2_{z_N}(\tau) = \frac{N^2}{\tau} \quad \text{or} \quad \sigma_{z_N}(\tau) = \frac{N}{\tau^{1/2}}. \tag{4.16}$$

4.2.5 Rate/Acceleration Random Walk Errors: $z_K(t)$

The term $\frac{K^2}{(2\pi f)^2} = \frac{K}{s}\frac{K}{s^*}\big|_{s=j2\pi f}$ in eqn. (4.12) corresponds to a linear system with transfer function $H(s) = \frac{1}{s}$ that is driven by input $\omega_K(t)$. The output of this linear system is $z_K(t)$. The state-space model for $z_K(t)$, corresponding to this linear system is,

$$\dot{z}_K(t) = \omega_K(t), \tag{4.17}$$

where $\omega_K(t)$ is white Gaussian noise with power spectral density

$$Q_K = K^2. \tag{4.18}$$

In the literature and on manufacturer specifications, this type of error is called *rate random walk* error for gyros and *acceleration random walk* error for accelerometers.

Given eqns. (4.18) and (4.17), the PSD of $z_K(t)$ is,

$$S_{z_K}(2\pi f) = \left(H(s)H(s^*)\Big|_{s=j2\pi f} \right) K^2 = \frac{K^2}{(2\pi f)^2}, \tag{4.19}$$

which has the desired form corresponding to eqn. (4.12). Using eqn. (4.11) on $S_{z_K}(f) = \frac{K^2}{(2\pi f)^2}$, yields error variance [1],

$$\sigma^2_{z_K}(\tau) = \frac{K^2 \tau}{3} \quad \text{or} \quad \sigma_{z_K}(\tau) = K\sqrt{\frac{\tau}{3}}. \tag{4.20}$$

4.2.6 Bias Instability: $z_B(t)$

The error term $z_B(t)$ corresponding to $S_{z_B}(f) = \frac{B^2}{2\pi f}$ is generally referred to, in the literature, as the *bias instability* (or flicker noise) [1, 2, 69, 120]. The remaining challenge is to find a finite-dimensional state-space model that is able to regenerate $\sigma^2_{z_B}(\tau)$ to suitable accuracy. Various approximation methods have been suggested in the literature, using state-space models of various dimensions. These include first-order Gauss-Markov [35, 64, 69, 120, 131, 151] and higher-order autoregressive models [107, 111, 136]. The important trade-off is that, as the dimension of the state-space model increases, the fidelity of the approximation increases, but so does the required real-time computational load of the state estimation algorithm. To exemplify the idea, the next section considers a first-order Gauss-Markov model, which represents exponentially correlated noise, to model the bias instability error.

4.2.7 Gauss-Markov Error Model

A first-order continuous-time Gauss-Markov model has the following model [23, 52, 59],

$$\dot{z}_B(t) = -\mu_B z_B(t) + \omega_B(t) \tag{4.21}$$

with,

$$\mu_B = \frac{1}{T_B}, \text{ where } T_B > 0. \tag{4.22}$$

The symbol T_B represents the correlation time of the process. The symbol $\omega_B(t)$ represents a white driving noise with power spectral density Q_B. A first-order scalar Gauss-Markov process can be used (approximately) to model the flat portion (i.e., bias instability) of the ASD plot as follows. If the manufacturer only provides the values of B and T_B, the PSD is

$$Q_B = \frac{2B^2\, ln(2)}{\pi(0.4365)^2\, T_B}. \tag{4.23}$$

the state-space model of eqn. (4.21) is completely specified. If instead, the manufacturer provides the ASD plot, then the analyst can first select T_B so that $1.89\, T_B$ lies near the flat portion of the ASD plot.

4.3 INS Propagation Error Model

The INS integrates the (bias compensated) IMU measurements through the vehicle kinematic model to propagate the vehicle state through time at the IMU measurement rate [49, 74, 143]. This section briefly presents the INS kinematic and error models.

The navigation equations in the Earth-centered Earth-fixed (ECEF) frame are:

$$\begin{bmatrix} \dot{\mathbf{p}}^e \\ \dot{\mathbf{v}}^e \\ \dot{\mathbf{R}}^e_b \end{bmatrix} \doteq \begin{bmatrix} \mathbf{v}^e \\ \mathbf{R}^e_b \mathbf{f}^b_{ib} - 2\Omega^e_{ie}\mathbf{v}^e + \mathbf{g}^e \\ \mathbf{R}^e_b \Omega^b_{eb} \end{bmatrix} \tag{4.24}$$

where $\mathbf{p}^e, \mathbf{v}^e$ denote the rover position and velocity state resolved in ECEF frame, $\mathbf{R}^e_b$ represents the rotation matrix transforming a vector from the body frame b to ECEF frame, Ω^e_{ie} is the skew-symmetric matrix of earth rotation rate ω^e_{ie}. The local gravity vector is $\mathbf{g}^e$ where

$$\mathbf{g}^e = \mathbf{G}_e(\mathbf{p}^e) - \Omega_{ie}\Omega_{ie}\mathbf{p}^e \tag{4.25}$$

The term $\mathbf{G}_e$ is the gravitational acceleration that is a function of rover position $\mathbf{p}^e$. Finally, Ω^b_{eb} is the skew-symmetric matrix version of the rotation rate vector

$$\omega^b_{eb} = \omega^b_{ib} - \mathbf{R}^b_e \omega^e_{ie} \tag{4.26}$$

The mechanization eqns. (4.24) is integrated to obtain the position, velocity, and attitude. The assumption is that the initial conditions of the vehicle states are known. There are many ways a system designer can initialize these states. The details of the mechanization equations and state initialization methods can be found in [49, 70, 71, 127].

Detailed derivatives of the first-order approximations of error state model can be found in [49, 65, 71, 100]. The linearized form of the mechanization eqns. (4.24) describes the INS error state propagation:

$$\begin{bmatrix} \delta\dot{\mathbf{p}}^e \\ \delta\dot{\mathbf{v}}^e \\ \dot{\rho}^e \end{bmatrix} \doteq \begin{bmatrix} \delta\mathbf{v}^e \\ \mathbf{G}^e\delta\mathbf{p}^e - 2\Omega^e_{ie}\delta\mathbf{v}^e + \mathbf{F}^e_{ib}\rho^e - \mathbf{R}^e_b\gamma_a \\ -\Omega^e_{ie}\rho^e + \mathbf{R}^e_b\gamma_g \end{bmatrix}. \tag{4.27}$$

where $\delta\mathbf{p}^e$ and $\delta\mathbf{v}^e$ indicate the error in position and velocity respectively, ρ^e indicates the angle error for rover attitude, $\mathbf{F}^e_{ib}$ is the skew-symmetric matrix computed from $\mathbf{f}^e_{ib}$, where $\mathbf{f}^e_{ib} = \mathbf{R}^e_b\mathbf{f}^b_{ib}$. The term $\mathbf{G}^e$ is the linearized error model for the local gravity vector $\mathbf{g}^e$ (See eqn. (11.15) and (11.16) of [49]).

$$\mathbf{G}^e = -GM[\frac{1}{((\mathbf{p}^e)^T\mathbf{p}^e)^{\frac{3}{2}}}\mathbf{I} - \frac{3}{((\mathbf{p}^e)^T\mathbf{p}^e)^{\frac{5}{2}}}\mathbf{p}^e(\mathbf{p}^e)^T] \tag{4.28}$$

where G is the universal gravitational constant and M represents mass of the earth.

The accelerometer and gyroscope bias state error propagation equations:

$$\begin{bmatrix} \delta\dot{\mathbf{b}}_g \\ \delta\dot{\mathbf{b}}_a \end{bmatrix} \doteq \begin{bmatrix} \lambda_g\delta\mathbf{b}_g + \varepsilon_g \\ \lambda_a\delta\mathbf{b}_a + \varepsilon_a \end{bmatrix} \tag{4.29}$$

4.4 INS Full Error State Model

Tight integration architectures of INS and GNSS are well-known and widely used in navigation application [38, 49]. The state vector for PPP-INS is slightly different than that of a

LADGNSS-aided INS. In the LADGNSS setup, all common-mode errors are adequately compensated whereas, in SF-PPP the system has to accommodate for residual atmospheric delays. In PPP-INS, the state vector has to be augmented with an extra error state for vertical atmospheric delay.

4.4.1 DGNSS-INS Full Error State

The state vector for DGNSS-INS is then,

$$\mathbf{x}(t) \doteq [\mathbf{p}^T, \mathbf{v}^T, \mathbf{q}^T, \mathbf{b}_a^T, \mathbf{b}_g^T]^T \in \Re^{16} \tag{4.30}$$

The symbol $\mathbf{q} \in \mathbb{R}^4$ represents the attitude quaternion. The state is integrated through time using eqn.(4.24) and the IMU data and corrected using an EKF. The full error state model can be obtained by combining eqns. (4.27) and (4.29) of Section 4.3.

$$\begin{bmatrix} \delta\dot{\mathbf{p}}^e \\ \delta\dot{\mathbf{v}}^e \\ \dot{\rho}^e \\ \delta\dot{\mathbf{b}}_g \\ \delta\dot{\mathbf{b}}_a \end{bmatrix} \doteq \begin{bmatrix} \mathbf{0} & \mathbf{I} & \mathbf{0} & \mathbf{0} & \mathbf{0} & 0 \\ \delta\mathbf{g}^e & -2\Omega_{ie}^e & F_{ib}^e & \mathbf{0} & \mathbf{0} & 0 \\ \mathbf{0} & \mathbf{0} & -\Omega_{ie}^e & \mathbf{0} & \mathbf{0} & 0 \\ \mathbf{0} & \mathbf{0} & \mathbf{0} & \lambda_g \delta\mathbf{b}_g & \mathbf{0} & 0 \\ \mathbf{0} & \mathbf{0} & \mathbf{0} & \mathbf{0} & \lambda_a \delta\mathbf{b}_a & 0 \end{bmatrix} \begin{bmatrix} \delta\mathbf{p}^e \\ \delta\mathbf{v}^e \\ \rho^e \\ \delta\mathbf{b}_g \\ \delta\mathbf{b}_a \end{bmatrix}$$
$$+ \begin{bmatrix} 0 & 0 & 0 & 0 \\ -\mathbf{R}_b^e & 0 & 0 & 0 \\ 0 & \mathbf{R}_b^e & 0 & 0 \\ 0 & 0 & \mathbf{I} & 0 \\ 0 & 0 & 0 & \mathbf{I} \end{bmatrix} \begin{bmatrix} \gamma_a \\ \gamma_g \\ \varepsilon_g \\ \varepsilon_a \end{bmatrix} \tag{4.31}$$

where **I** and **0** denote identity and zero matrices with 3 × 3 dimension respectively. The symbol *0* symbolizes zero matrix with 3 × 1 dimension.

4.4.2 PPP-INS Full Error State

The full state vector for PPP-INS is then,

$$\mathbf{x}(t) \doteq [\mathbf{p}^T, \mathbf{v}^T, \mathbf{q}^T, \mathbf{b}_a^T, \mathbf{b}_g^T, A_v]^T \in \Re^{17} \tag{4.32}$$

The symbol $A_v \in \mathbb{R}^1$ represents residual vertical atmospheric delay. The state is integrated through time using eqn.(4.24) and the IMU data and corrected using an EKF. The full error state model can be obtained by combining eqns. (4.27) and (4.29) of Section 4.3.

$$\begin{bmatrix} \delta\dot{\mathbf{p}}^e \\ \delta\dot{\mathbf{v}}^e \\ \dot{\rho}^e \\ \delta\dot{\mathbf{b}}_g \\ \delta\dot{\mathbf{b}}_a \\ \delta\dot{A}_v \end{bmatrix} \doteq \begin{bmatrix} \mathbf{0} & \mathbf{I} & \mathbf{0} & \mathbf{0} & \mathbf{0} & \mathit{0} \\ \delta\mathbf{g}^e & -2\Omega_{ie}^e & F_{ib}^e & \mathbf{0} & \mathbf{0} & \mathit{0} \\ \mathbf{0} & \mathbf{0} & -\Omega_{ie}^e & \mathbf{0} & \mathbf{0} & \mathit{0} \\ \mathbf{0} & \mathbf{0} & \mathbf{0} & \lambda_g\delta\mathbf{b}_g & \mathbf{0} & \mathit{0} \\ \mathbf{0} & \mathbf{0} & \mathbf{0} & \mathbf{0} & \lambda_a\delta\mathbf{b}_a & \mathit{0} \\ \bar{0} & \bar{0} & \bar{0} & \bar{0} & \bar{0} & 0 \end{bmatrix} \begin{bmatrix} \delta\mathbf{p}^e \\ \delta\mathbf{v}^e \\ \rho^e \\ \delta\mathbf{b}_g \\ \delta\mathbf{b}_a \\ \delta A_v \end{bmatrix}$$
$$+ \begin{bmatrix} \mathit{0} & \mathit{0} & \mathit{0} & \mathit{0} & 0 \\ -\mathbf{R}_b^e & \mathit{0} & \mathit{0} & \mathit{0} & 0 \\ \mathit{0} & \mathbf{R}_b^e & \mathit{0} & \mathit{0} & 0 \\ \mathit{0} & \mathit{0} & \mathbf{I} & \mathit{0} & 0 \\ \mathit{0} & \mathit{0} & \mathit{0} & \mathbf{I} & 0 \\ 0 & 0 & 0 & 0 & 1 \end{bmatrix} \begin{bmatrix} \gamma_a \\ \gamma_g \\ \varepsilon_g \\ \varepsilon_a \\ \varepsilon_{A_v} \end{bmatrix} \tag{4.33}$$

where $\bar{0}$ is zero matrix with dimension of 1×3. The residual atmospheric delay A_v is modeled as a random walk process and its driving noise is denoted by ε_{A_v}.

Chapter 5

Experimental Results

This section includes descriptions of the data set that will be used for analysis, metrics to understand the quality of the available GNSS data, metrics for assessing algorithm performance, the employed algorithm, acquired data set, performance analysis of the aforementioned DGNSS-PVA, DGNSS-INS and PPP-INS algorithm and effect of sensor (i.e. IMU, GNSS) measurement quality in rover positioning. The main purpose is to analyze the algorithm's ability to achieve either SAE specification [12] or yet, a one-meter horizontal positioning accuracy requirement for moving platform using L1 real-time PPP GPS data. For generation of results, this section describes the position estimation algorithms used for the performance analysis herein. The main references can be found in [49, 122, 124].

5.1 DGNSS based Position Estimation

This paper considers the problem of state estimation, where the main points of interest are whether meter level position estimation accuracy can be reliably achieved and the sensitivity of that accuracy to correction latency. The experimental analysis includes two scenarios: stationary and moving.

The PVA approach will be used for both the stationary and moving data. For both sets of data, the same model parameters will be used, which are tuned for an automotive motion scenario. For the PVA model, state estimation is performed using the linear Kalman filter (KF) [24, 49]. The differential corrections are designed to remove common-mode errors, receiver clock errors are accommodated by double differencing, and multipath is modeled as a state.

The INS approach is only implemented for the moving data. For the INS approach, state estimation is implemented by an extended Kalman filter [49]. The description of both algorithms of DGNSS are described.

5.1.1 Time Propagation Models

Two approaches to temporal propagation of the state are considered. The position, velocity, and acceleration (PVA) approach of Section 5.1.1 only uses GNSS measurements, while the INS approach of Section 5.1.1 also incorporates inertial measurements.

PVA model

The PVA rover state is

$$x = [\mathbf{p}^\top, \mathbf{v}^\top, \mathbf{a}^\top, \mathbf{M}_r]^\top \in \mathbb{R}^{\mathrm{n_s}}, \tag{5.1}$$

where $n_s = 9 + m$. The symbols $\mathbf{p}$, $\mathbf{v}$, $\mathbf{a} \in \mathbb{R}^3$ represent the position, velocity and acceleration vectors. The analysis herein augments the standard PVA state vector [24, 49, 122] with a vector of multipath states $\mathbf{M}_r \in \mathbf{R}^m$.

The discrete-time PVA rover state is assumed to propagate as

$$\mathbf{x}_k \doteq \boldsymbol{\Psi}\mathbf{x}_{k-1} + \boldsymbol{\Gamma}\boldsymbol{\omega}_{k-1}, \tag{5.2}$$

where $\mathbf{x}_k = \mathbf{x}(t_k)$, $t_k = kT$, where T is the time between measurement epochs, $\boldsymbol{\omega}_k \sim \mathcal{N}(0, \mathbf{Q}_d)$, and the matrices of the discrete-time state-space model are:

$$\boldsymbol{\Psi} = \begin{bmatrix} \psi_v & 0 \\ 0 & \psi_M \end{bmatrix}, \quad \boldsymbol{\Gamma} = \begin{bmatrix} \boldsymbol{\Gamma}_v & 0 \\ 0 & \boldsymbol{\Gamma}_M \end{bmatrix}, \text{ and } \quad \boldsymbol{Q}_d = \begin{bmatrix} \boldsymbol{Q}_{d_v} & 0 \\ 0 & \boldsymbol{Q}_{d_M} \end{bmatrix}.$$

The PVA model assumes that the acceleration vector is constant for all $t \in [t_{k-1}, t_k]$, and that its value is accurately modeled as a first-order discrete-time Markov process between measurement epochs. The parameters of the acceleration Markov process are assumed to be time-invariant.

The PVA state estimate is time-propagated as

$$\hat{\mathbf{x}}_k^- = \boldsymbol{\Psi}\hat{\mathbf{x}}_{k-1}^+, \tag{5.3}$$

where the superscript '–' and '+' denote the values just before and after incorporating the GNSS measurements at time k. The error state covariance matrix is time-propagated as

$$\mathbf{P}_k^- = \boldsymbol{\Psi}\mathbf{P}_{k-1}^+\boldsymbol{\Psi}^\top + \boldsymbol{\Gamma}\mathbf{Q}_d\boldsymbol{\Gamma}^\top. \tag{5.4}$$

GNSS receivers allow the user to select T over a wide range from 0.02 seconds to infinity. The tradeoff is that the validity of the PVA model improves for smaller T, but the assumption of GNSS white measurment noise becomes more valid as T increases. In this article, $T = 1$ second.

The main trade-off in the PVA approach is that there is no optimal set of model parameters uniformly applicable over all epochs. Nevertheless, the designer must choose a set of model parameters. For epochs over which the selected model is accurate, the PVA approach will perform well, perhaps even optimally. Over other epochs, the performance may deteriorate. Herein, the model parameters of the PVA and multipath states are tuned for a moving platform with moderate acceleration correlated over a few seconds. The details of the model and its parameters ($\boldsymbol{\Psi}$, $\boldsymbol{\Gamma}$ and $\mathbf{Q}_d$) are explained in Appendix B of [122].

INS model

The INS rover state is

$$\mathbf{x} = [\mathbf{p}^\top, \mathbf{v}^\top, \mathbf{q}^\top, \mathbf{b}_a^\top, \mathbf{b}_g^\top, \mathbf{M}_r]^\top \in \mathbb{R}^{\mathrm{n_s}}. \tag{5.5}$$

where $n_s = 16 + m$ and m is the number of GNSS satellites available.

The symbols $\mathfrak{p}$, $\mathbf{v}$, $\mathbf{b}_a$, $\mathbf{b}_g \in \mathbb{R}^3$ represent the ECEF position, velocity, accelerometer bias and gyro bias vectors, while $\mathbf{q} \in \mathbb{R}^4$ is the attitude quaternion, and $\mathbf{M}_r \in \mathbb{R}^{\mathrm{m}}$ is the multipath bias state vector with one element per satellite.

The kinematic model for the continuous-time propagation of the vehicle state has the form:

$$\dot{\mathbf{x}}(t) = f(\mathbf{x}(t), \mathbf{u}(t)) \tag{5.6}$$

where the specific form of the function f can be found in many references, e.g., [49]. The vector $u \in \mathbb{R}^6$ denotes the IMU sensor measurements: specific force vector and angular rate vector.

The IMU measurements occur in discrete-time with sample period $\tau \ll T$. The IMU discrete-time measurements are modeled as

$$\tilde{\mathbf{u}}(\tau_{k,i}) \doteq \mathbf{u}(\tau_{k,i}) + \mathbf{b}_u(\tau_{k,i}) + \boldsymbol{\omega}_u(\tau_{k,i}) \tag{5.7}$$

where $\omega_u(\tau_{k,i}) \sim \mathcal{N}(0, Q)$ and the sensor bias vector $\mathbf{b}_u = [\mathbf{b}_a^\top, \mathbf{b}_g^\top]$ is modeled as a first-order Markov process. Let $\tau_{k,i} = t_k + i\tau$ where $i = 0, \ldots, f_s T$, $t_k = kT$ are the GNSS measurement times, and $f_s = \frac{1}{\tau}$. Over any interval $[t_{k-1}, t_k]$, when the context is clear, this notation will be simplified to τ_i. In this notation, $\mathbf{x}_{k,i}$ means $\mathbf{x}(\tau_{k,i})$, which may be simplified to $\mathbf{x}_i$.

Time propagation of the INS state is the numeric integral of

$$\dot{\hat{\mathbf{x}}}(t) = f(\hat{\mathbf{x}}(t), \hat{\mathbf{u}}(t)) \tag{5.8}$$

in discrete-time, which is denoted as

$$\hat{\mathbf{x}}_i = \phi(\hat{\mathbf{x}}_{i-1}, \hat{\mathbf{u}}_{i-1}) \tag{5.9}$$

where $\hat{\mathbf{u}}_i = \tilde{\mathbf{u}}_i - \hat{\mathbf{b}}_u$ and

$$\phi(\mathbf{x}_{i-1}, \mathbf{u}_{i-1}) = \mathbf{x}_{i-1} + \int_{\tau_{i-1}}^{\tau_i} f(\mathbf{x}(\tau), \mathbf{u}(\tau)) d\tau.$$

Many algorithms are available for the numeric integration [33].

The error propagation model between two IMU time samples can be written as:

$$\delta\mathbf{x}_i \doteq \mathbf{\Phi}_i \delta\mathbf{x}_{i-1} + \gamma_i \boldsymbol{\omega}_i \tag{5.10}$$

where $\delta\mathbf{x}_i = \mathbf{x}_i - \hat{\mathbf{x}}_i$, $\boldsymbol{\omega}_i \sim \mathcal{N}(0, \mathbf{Q}_d)$, and $\mathbf{\Phi}_i = \frac{\delta\phi}{\delta\mathbf{x}}|_{\mathbf{x}_{i-1}, \tilde{u}_{i-1}}$ is the discrete-time INS error state transition matrix. The derivations are in [49, 122, 128].

Due to $\tau \ll T$, eqn. (5.9) is iterated many times between consecutive GNSS measurements. The iterated application of eqn. (5.9) starts for $i = 0$ with $\hat{\mathbf{x}}(\tau_{k-1,0}) = \hat{\mathbf{x}}_{k-1}^{+}$, which is the state estimate after incorporating the GNSS measurements at epoch $k-1$. The iterated application of eqn. (5.9) is denoted as

$$\hat{\mathbf{x}}_k^{-} = \phi_k(\hat{\mathbf{x}}_{k-1}^{+}, \mathbf{U}_{k-1}) \tag{5.11}$$

where $\mathbf{U}_{k-1} = \{\tilde{\mathbf{u}}(\tau_i) \text{ for } \tau_i \in [t_{k-1}, t_k]\}$ denotes the set of IMU measurements over the GNSS epoch. The result of the iterated numeric integration by (5.9) is the prior $\hat{\mathbf{x}}_k^{-}$ for the extended Kalman filter measurement update at t_k.

The INS error covariance matrix is propagated at high sampling rate that can be described as below

$$\mathbf{P}_k^- = \mathbf{\Phi}_k \mathbf{P}_{k-1}^+ \mathbf{\Phi}_k + \mathbf{Q}_{d_k} \tag{5.12}$$

where the derivation and detailed discussion of $\mathbf{Q}_{d_k}$ and $\mathbf{\Phi}_k$ are beyond the scope of this article, but can be found in Section 2 and 3 of [128].

5.1.2 Measurement Update Model

For both the PVA and INS approaches, the prior state at time t_k will be corrected using the double-differenced pseudorange and Doppler measurements as defined in Section 3.1.5.

The model for the measurement vector $\mathbf{z}_k^s = [d\boldsymbol{\rho}^s_{r_k},\ \lambda d\mathbf{D}^s_{r_k}]^\top$ for satellite s at t_k is

$$\mathbf{z}_k^s \doteq \mathbf{h}_d^s(x_k) + \mathbf{n}_{rk}^s, \tag{5.13}$$

where $\mathbf{h}_d^s(x_k)$ represents the differentially corrected pseudorange and Doppler differenced with the measurements for the pivot satellite, as defined in eqns. (3.32) and (3.34):

$$\mathbf{h}_d^s(x_k) = \begin{bmatrix} \mathbf{R}(\mathbf{p}_k, \hat{\mathbf{p}}_k^s) - \mathbf{R}(\mathbf{p}_k, \hat{\mathbf{p}}_k^{s_p}) + \mathbf{M}_r^s(t_k) \\ (\mathbf{h}_k^s - \mathbf{h}_k^{s_p}) \cdot \mathbf{v}_k \end{bmatrix} \text{ and } \mathbf{n}_{rk}^s = \begin{bmatrix} d\boldsymbol{\eta}_{rk}^s \\ d\boldsymbol{\epsilon}_{rk}^s \end{bmatrix}$$

The noise vector $\mathbf{n}_{rk}^s \sim \mathcal{N}(0, \mathbf{R}_{d_d})$ with $\mathbf{R}_{d_d} = \begin{bmatrix} \mathbf{R}_p^s + \mathbf{R}_p^{s_p} & 0 \\ 0 & \mathbf{R}_d^s + \mathbf{R}_d^{s_p} \end{bmatrix}$, where cross satellite correlation introduced by the double-difference is ignored.

Using eqn. (5.13), the measurement residual is computed as

$$d\mathbf{z}_k^s = \mathbf{z}_k^s - \mathbf{h}_d^s(\hat{\mathbf{x}}_k^-).$$

By employing the first-order Taylor series expansion, the linearized measurement model is:

$$d\mathbf{z}_k^s \doteq \mathbf{H}_{d_k}^s \delta\mathbf{x}_k + \mathbf{n}_{rk}^s \tag{5.14}$$

where the measurement or observation matrix is referred to as $\mathbf{H}^s_{d_k}$. The measurement matrix can be described as below

$$\mathbf{H}^s_{d_k} = \begin{bmatrix} (\mathbf{h}^s_k - \mathbf{h}^{s_p}_k) & \mathbf{0}_{l_1} & \mathbf{0}_{l_2} & \mathbf{e}_s \\ \mathbf{0}_{l_1} & (\mathbf{h}^s_k - \mathbf{h}^{s_p}_k) & \mathbf{0}_{l_2} & \mathbf{0}_{l_3} \end{bmatrix}, \tag{5.15}$$

with $\mathbf{e}^s \in \mathbf{R}^{1\times m}$ being s^{th} row of the identity matrix and $\mathbf{0}_{l_j}$ being the zero vector in $\mathbf{R}^{1\times l_j}$. For PVA $l_2 = 3$, while for INS[1] $l_2 = 9$. Both case have $l_1 = 3$ and $l_3 = m$. Accumulating all satellite measurements $d\mathbf{z}^s_k$ into vector $\mathbf{z}_k$ yields:

$$d\mathbf{z}_k = \mathbf{H}_{d_k}\delta\mathbf{x}_k + \mathbf{n}_k \tag{5.16}$$

where $d\mathbf{z}_k = [d\mathbf{z}^s_k]|_{s=1:m}$ is a vector in $\mathbf{R}^{2m}$ and $\mathbf{H}_{d_k} = [\mathbf{H}^s_{d_k}]|_{s=1:m}$ is a matrix in $\mathbf{R}^{2m\times n_s}$, and $m+1$ denotes total available satellite measurements.

5.1.3 Outlier Accommodation

The data for the analysis was collected on a moving platform in real life circumstance. The trajectory had trees and buildings nearby, thus the measurements may suffer from some outliers. Therefore, outlier accommodation must be included.

Outlier detection is implemented by applying a Neyman Pearson (NP) test [112] to each element of the measurement residual vector $\mathbf{z}_k$. Residuals are only used in the KF/EKF if they pass the test $d\mathbf{z}^s_k \leq \gamma_o \sigma^s_{z_k}$ where symbol $\sigma^s_{z_k}$ is the residual standard deviation as computed by the KF/EKF and γ_o is a user-defined threshold.

---

[1] The INS error state has one less dimension than the INS state because the quaternion has four elements while its error representation only requires three elements [49].

5.1.4 Experimental Data Description

The experimental data were acquired using a consumer-grade, single-frequency GNSS receiver (u-blox M8T). The data were saved and post-processed so that multiple algorithms can be compared using identical data. All state estimation results are produced using only pseudorange and Doppler data. Phase measurements were not used for state estimation.

In real-time applications, base station data would be obtained and used to compute the DGNSS correction parameters $[a_{t_0}, b_{t_0}, t_0, IODE]$. These correction parameters would be communicated to vehicles by any convenient radio link using the RTCM standard [11] and the NTRIP protocol. Our experiments use typically cell phone data channels. Most FHWA and state DOT pilot projects us dedicated short-range radios (DSRC). For this particular experiment, because we wanted to implement and compare multiple algorithms, the data was saved to a hard disk. The value of L used in the computation of the correction parameters was $L = 500$. This value of L was selected to be about four times the expected base pseudorange multipath correlation time. The DGNSS corrections $c(t; t - \ell)$ will be used at time t to study the impact of the latency ℓ.

Stationary Data

The duration of the experiment is 3000 seconds. The stationary rover has a GNSS receiver connected to an antenna at a surveyed location on the top of a campus building. The base station was at ESRI with a baseline separation of 14.5 km.

Moving Data

This experimental hardware includes two GNSS receivers and one IMU. Both receivers are connected to the same consumer grade antenna (Antcomm ANN-MS-0-005). One receiver is a single frequency u-blox M8T (consumer grade) and the other is dual frequency NOVATEL OEMV2 (survey grade). The dataset length is 1300 s. The M8T single-frequency GNSS receiver provides data for the state estimation using both PVA and INS. The IMU sensor used for this experiment is an NV-IMU 1000. The UCR base station was used with a baseline separation of 6 km.

During data acquisition, the hardware is mounted on a sedan that is driven repeatedly along a multi-block section of an urban street. To focus on performance as a function of communication latency, the street was selected to have only with low buildings and trees adjacent to the street. Therefore, the sky is open, not an urban canyon. The section of street has three stop lights. The trajectory involves two U-turns, one at each end. Therefore, the trajectory involves acceleration and turn rates typical for urban trajectories, which may exceed the variation predicted by the PVA model parameters for short time durations, followed by other trajectory sections where the near constant velocity travel in a lane yields conservative motion relative to that predicted by the PVA model.

5.1.5 Ground Truth Trajectory: Dynamic

Ground truth trajectory estimation was performed in post-processing using a Maximum a Posteriori smoothing algorithm [148]. This algorithm used the two-frequency pseudorange and integer-resolved, carrier phase GNSS data from the OEMV3 and IMU to achieve centimeter accuracy. This ground truth trajectory and OEMV2 data are only used to assess the accuracy of the state estimation results that used the single frequency u-blox M8T.

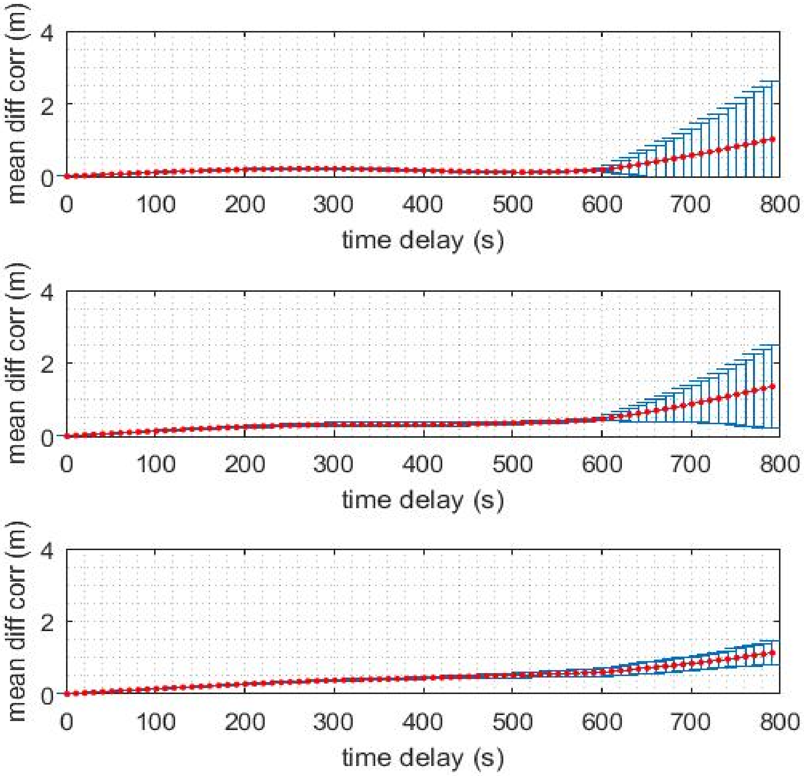

Figure 5.1: Correction error defined in eqn. (5.17) versus latency for three satellites.

5.1.6 Correction Sensitivity to Latency

The correction error due to communication latency l, as defined after eqn. (3.8), is

$$e_c(k,l) = |\hat{c}(k;k) - \hat{c}(k;k-l)|, \tag{5.17}$$

where $\hat{c}(k;k)$ is the correction with no latency and $\hat{c}(k;k-l)$ is the correction with latency of l epochs. Both corrections are computed using eqn. (3.6). Statistics related to $e_c(k,l)$ are computed by averaging over $k = 1,\ldots,N_d$.

Fig. 5.1 shows the mean plus and minus the standard deviation of $e_c(k,l)$ versus l for three satellites. For each fixed value of l and each satellite, the mean and standard deviation of $e_c(k,l)$ are computed from experimental data by averaging over $(N_d - \ell)$ epochs where $N_d = 3000$. Fig. 5.1 shows that the correction error $e_c(k,l)$ remains less than one meter for over 600 seconds.

5.1.7 Position Estimation Scenarios

The following subsections report positioning accuracy for three estimation scenarios:

1. **Stationary PVA** is the $(9+m)$ state PVA model with a Linear KF to estimate the state defined in eqn. (5.1) using double-difference pseudorange and Doppler measurements when the platform is stationary. This data set is outlier free, so a NP test is not required. Label this scenario by $a = 1$.
2. **Moving PVA** is the $(9+m)$ state PVA model with a Linear KF to estimate the state defined in eqn. (5.1) using double-difference pseudorange and Doppler measurements. It used the NP outlier rejection criteria with $\gamma_o = 1$. Label this scenario by $a = 2$.
3. **Moving INS** is an $(16+m)$ state INS model with an EKF to estimate the state defined in eqn. (5.5) using double-difference pseudorange and Doppler measurements. It used the NP outlier rejection criteria with $\gamma_o = 1$. Label this scenario by $a = 3$.

Additional information on the selection of the model parameters are included in the Appendix of [122].

Each algorithm is used to process the set of measurements $(k = 1, \dots, N_d)$ as if they were occurring in real-time (i.e., incrementally) to estimate the state vector at each time k, using correction $\hat{c}(k; k-l)$ from eqn. (3.6) for a given value of the latency l.

5.1.8 Accuracy Metrics

Due to our interest in vehicular applications, we separately analyze horizontal and vertical accuracy. Therefore, the main metrics used for comparison of algorithms are the norm of the horizontal position error:

$$e_h^a(k,l) = \left\| \begin{bmatrix} 1 & 0 & 0 \\ 0 & 1 & 0 \end{bmatrix} \left(\mathbf{p}_g(k) - \hat{\mathbf{p}}_r^a(k,l)\right) \right\| . \tag{5.18}$$

and the vertical position error:

$$e_v^a(k,l) = \begin{bmatrix} 0 & 0 & 1 \end{bmatrix} \left(\mathbf{p}_g(k) - \hat{\mathbf{p}}_r^a(k,l)\right) . \tag{5.19}$$

The symbol $\hat{\mathbf{p}}_r^a(k,l)$ denotes the position estimated at time k, latency l and algorithm a. The symbol $\mathbf{p}_g(k)$ denotes the antenna's ground truth position as discussed in Section 5.1.4. Eqns. (5.18-5.19) assume that the position vector has been transformed into a locally level frame-of-reference.

5.1.9 Positioning Accuracy

Fig. 5.2 show histograms of $e^n_{h_{k,l}}$ as defined in eqn. (5.18) for latency $l = 0$ for each scenario summarized in Section 5.1.7.

Table 5.1 and 5.2 summarize various measures of positioning accuracy for latency $l = 0$

Table 5.1: Horizontal Positioning Performance with $l = 0$.

Scen.	Mean	Std. Dev	Max	Prob.	
				$e_h < 1m$	$e_h < 2m$
1	0.33	0.16	0.91	99	100
2	0.46	0.34	1.70	90	100
3	0.39	0.18	1.10	98	100

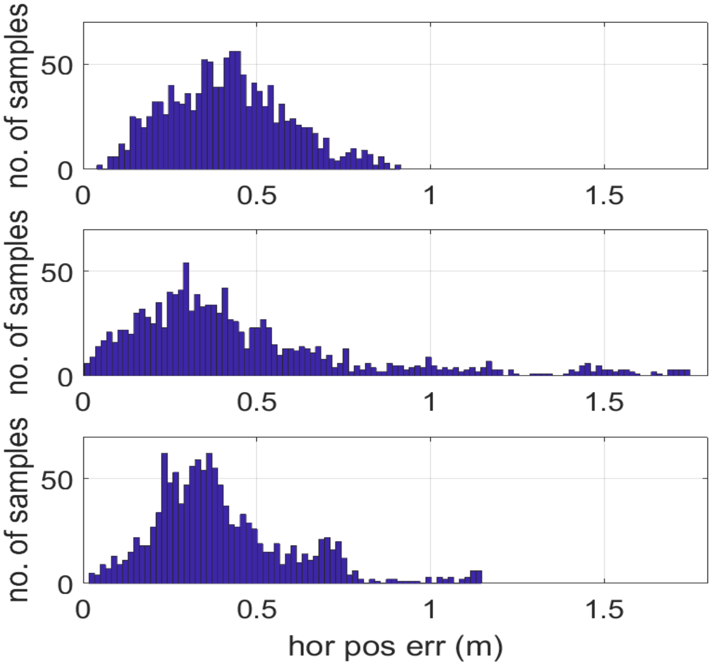

Figure 5.2: Histogram of horizontal position error $e^n_{h_{k,l}}$ defined in eqn. (5.18) with $l = 0$ for Scenario 1 (Top), Scenario 2 (Middle), Scenario 3 (Bottom).

for horizontal (e_h) and vertical (e_v) error, respectively. Column 1 shows the scenario number a. Column 2 displays the mean position error. Column 3 contains the standard deviation of the position error. Column 4 shows the maximum value of the position error. Column 5 reports the percentage of samples that have a positioning error less than a specified accuracy. Row 1 shows the Scenario 1 results over $N_d = 3000$ seconds. Rows 2-3 show the statistics for the moving data using Scenarios 2 and 3 over $N_d = 1300$ seconds.

Table 5.2: Vertical Positioning Performance with $l = 0$.

Scen.	Mean	Std. Dev	Max	Prob.	
				$e_v < 2m$	$e_v < 3m$
1	0.59	0.38	1.65	100.00	100.00
2	0.98	0.70	4.40	95.00	98.00
3	0.93	0.52	3.20	97.00	99.80

For the stationary case ($a = 1$), the PVA-KF approach tuned for vehicular motion is a conservative model, meaning that the variation of the modeled acceleration exceeds the actual acceleration. This scenario achieves meter level horizontal position accuracy for 99% of the samples.

For the moving case ($a = 2$), the PVA-KF approach yields a position error distribution with wider variation than for the stationary data set. This is expected due to the fact that in Scenario 2 the platform has a wider range of acceleration. Nevertheless, the PVA approach achieves meter level horizontal position accuracy at 90%.

For the moving case ($a = 3$), the INS-EKF approach yields a position error distribution with statistics similar to that for the stationary data set. This is expected because it is the purpose of the INS to remove the motion that is predictable based on the IMU data. After doing so, the INS error model has small eigenvalues, yielding slowly changing error states that are relatively independent of the vehicle motion. The double-difference GNSS aided INS approach with multipath states achieves one meter accuracy at 98% and two meter accuracy at 100%, thereby exceeding the SAE standard [12].

5.1.10 Position Estimation: Sensitivity to Latency

The experiment is repeated for each scenario for latency values $l = 0, \ldots, 900$ seconds. For the stationary case ($a = 1$), with $N_d = 3000$. For the moving cases ($a = 2, 3$), with $N_d = 500$. For each scenario a and and each latency l, this produces the position sequence $\hat{p}^a_{k,l}$ for $k = 1, \ldots, N_d$.

For each of the three scenarios, Fig. 5.3 illustrates the effect of the DGNSS correction latency l on the GNSS position accuracy as measured by $e^a_{h_{k,l}}$ defined in eqn. (5.18). For each graph, the black curve shows the mean of $e^a_{h_{k,l}}$. Each point on the graph is also marked with a one-standard-deviation error bar that is indicated in blue.

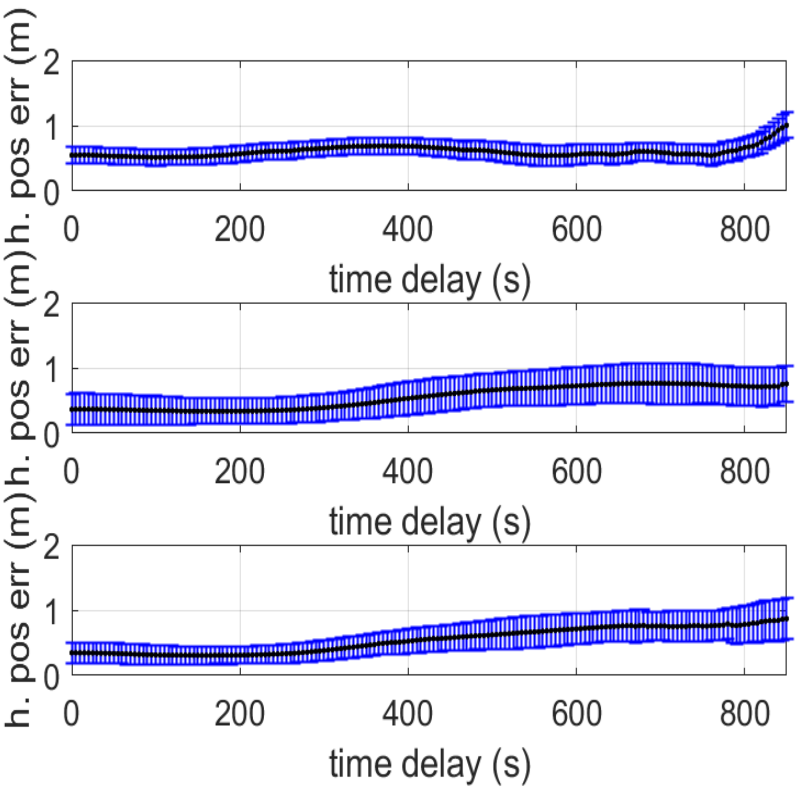

Figure 5.3: Horizontal position error vs latency. Scenario 1 (Top). Scenario 2 (Middle). Scenario 3 (Bottom).

All three figures show that position estimation accuracy is insensitive to communication latency in the sense that one meter accuracy at the $1-\sigma$ level is achievable for latency exceeding 500 sec.

5.2 PPP based Position Estimation

This study considers the problem of state estimation for meter-level accuracy achievement using real-time PPP method. The experimental analysis is performed for moving scenarios. The INS approach is only implemented for the moving data. For the INS approach, state estimation is implemented by an extended Kalman filter [49]. The description of PPP-INS algorithm is described herein.

The time propagation model for PPP-INS is mentioned in Section 4. The state vector is first introduced in eqn. (4.32). The kinematic equations for error state vectors are found in eqns. (4.24-4.29). The full state error covariance propagation equation is mentioned in eqn. (4.33).

5.2.1 PPP Compensated Measurement Update Model

EKF state update equations are described herein. Based on eqn. (3.35), the measurement residual can be computed as

$$d\mathbf{z}_k^s = \mathbf{z}_k^s - \mathbf{h}^s(\hat{\mathbf{x}}_k^-). \tag{5.20}$$

Employing the first-order Taylor series expansion, the linearized measurement model is:

$$d\mathbf{z}_k^s \doteq \mathbf{H}_k^s \delta\mathbf{x}_k + \eta_k^s. \tag{5.21}$$

For the pair of satellites s and s_p, the measurement matrix $\mathbf{H}_k^s$ is

$$\mathbf{H}_k^s = \begin{bmatrix} (\mathbf{h}_r^s - \mathbf{h}_r^{s_p}) & \mathbf{0}_3 & \mathbf{0}_9 & F(\psi_r^s) - F(\psi_r^{s_p}) \\ \mathbf{0}_3 & (\mathbf{h}_r^s - \mathbf{h}_r^{s_p}) & \mathbf{0}_9 & 0 \end{bmatrix}. \tag{5.22}$$

Where $\mathbf{0}_3$ and $\mathbf{0}_9$ denote zero matrices with 1×3 and 1×9 dimensions respectively. The term $F(\psi_r^s) - F(\psi_r^{s_p})$ is the obliquity factor difference that can be computed using eqn. (7.9).

Accumulating all satellite measurement residual $d\mathbf{z}_k^s$ into a vector $d\mathbf{z}_k$ yields:

$$d\mathbf{z}_k \doteq \mathbf{H}_k \delta\mathbf{x}_k + \eta_k \tag{5.23}$$

where $d\mathbf{z}_k \in \mathbf{R}^{2m}$, and $\mathbf{H}_k$ is a matrix with $2m$ rows.

5.2.2 Stationary Experimental Results

This section presents experimental results for positioning performance using the three PPP algorithms defined in Section 5.2.2. A goal is to analyze the ability to satisfy a one-meter accuracy specification.

Position Estimation Algorithms

Section 5.2.2 will study performance using three algorithms:

PPP-LS: This defines the state vector as

$$\mathbf{x}(t) = [\mathbf{p}^T, t_r, A_v]^T \in \Re^5$$

and solves each epoch of data separately using Least Squares (LS) with L1 PPP pseudorange measurements. These results are point-wise, without any filtering.

PPP-PVA: This defines the state vector as

$$\mathbf{x}(t) = [\mathbf{p}^T, \mathbf{v}^T, \mathbf{a}^T, A_v]^T \in \Re^{10}$$

and estimates the state using a linear Kalman Filter (KF) with single-differenced (between satellites) PPP L1 pseudorange and Doppler measurements.

PPP-INS: This defines the state vector as

$$\mathbf{x}(t) = [\mathbf{p}^T, \mathbf{v}^T, \mathbf{q}^T, \mathbf{b}_a^T, \mathbf{b}_g^T, A_v]^T \in \Re^{17}$$

and estimates the state using an extended Kalman Filter (KF) with single-differenced (between satellites) PPP L1 pseudorange and Doppler measurements. The IMU data is artificially generated to have the characteristics of a consumer-grade IMU (i.e., ADIS16360) (see appendix of [125]).

Each algorithm processes the set of GNSS measurements ($k = 1, \ldots, N_d$) incrementally, as if they were occurring in real-time, to estimate the state vector at each time k. The state variable s_v is a vector with one element per satellite. This state is augmented to account for multipath and residual atmospheric errors.

The symbol $\hat{\mathbf{p}}_k^a$ denotes the position estimated at time k for algorithm a, where $a = 1$ for PPP-LS, $a = 2$ for PPP-PVA, and $a = 3$ for PPP-INS.

Stationary Datasets

The experimental analysis will use L1 pseudorange and Doppler measurements. Carrier phase measurements were not directly used because integer resolution is not reliable for single-frequency receivers and the float solution require tens of minutes to converge.

To evaluate the consistency of the PPP results, experiments were performed using spatially separated datasets. Each dataset is from a stationary reference antenna for which the ground truth position is known. Table 5.3 summarizes key information about each dataset. The first column displays the name of the reference station in the CORS network, which will also be used as the name of the dataset. The second column states the general location of the reference station. The third column states the receiver brand and model. The fourth column states the antenna type brand and model. The fifth column states the length of the dataset in seconds. All of these datasets were acquired using ftp in Rinex 2.11 format for the same time: date-March 12, 2019 and time-7:00 pm in Pacific time-zone. The PPP data to compute real-time corrections was acquired from the sources listed in Table 3.3 for the same date and time. The 200 Hz IMU data for the PPP-INS algorithm was artificially generated to have consumer grade sensor characteristics (see the Appendix B of [125]).

Table 5.3: Dataset Description.

Base Station	Location	Receiver Name	Antenna Type	Data Length, s
BRMU	Bermuda	LEICA GRX1200GGPRO	JAVRINGANT DM + None	3600
HNTP	Maryland	LEICA GRX1200GGPRO	LEIAX1202GG + None	3040
QUIN	California	JAVAD TRE 3 DELTA	ASH701945E M + SNOW	3100

Positioning Accuracy

Fig. 5.4 shows histograms of $e^a_{h_k}$ as defined in eqn. (5.18) for the three datasets described in Section 5.1.4 and for each algorithm defined in Section 5.2.2. Each column shows the histogram of a given algorithm for all three datasets. Each row shows the histogram of all three algorithms for a given dataset. The performance improves as the algorithm improves (INS is better than PVA which is better than LS).

Table 5.4: Positioning Performance of the Algorithms Defined in Section 5.1.8.

(a) Horizontal Error Statistics for BRMU dataset.

Scenario	Mean	Std. Dev	Max	Prob. of $e^a_{h_{k,0}}$	
				$< 1m$	$< 2m$
1. LS	1.86	0.21	2.61	0	77
2. PVA	1.35	0.48	2.16	34	89
3. CG-INS	0.81	0.21	1.88	82	100

(b) Vertical Error Statistics for BRMU dataset.

Scenario	Mean	Std. Dev	Max	Prob. of $e^a_{v_{k,0}}$	
				$< 2m$	$< 3m$
1. LS	2.85	2.33	5.41	31	39
2. PVA	4.18	0.87	6.56	0	10
3. CG-INS	5.51	1.26	8.04	0.08	0.08

(a) Horizontal Error Statistics for HNTP dataset.

Scenario	Mean	Std. Dev	Max	Prob. of $e^a_{h_{k,0}}$	
				$< 1m$	$< 2m$
1. LS	1.67	0.49	2.50	6	65
2. PVA	1.19	0.41	2.24	45	96
3. CG-INS	0.52	0.25	0.98	100	100

(b) Vertical Error Statistics for HNTP dataset.

Scenario	Mean	Std. Dev	Max	Prob. of $e^a_{v_{k,0}}$	
				$< 2m$	$< 3m$
1. LS	1.37	0.51	2.40	85	100
2. PVA	1.70	0.47	2.67	70	100
3. CG-INS	0.03	0.63	1.21	100	100

(a) Horizontal Error Statistics for QUIN dataset.

Scenario	Mean	Std. Dev	Max	Prob. of $e^a_{h_{k,0}}$	
				$< 1m$	$< 2m$
1. LS	0.73	0.34	1.60	74	100
2. PVA	0.47	0.26	3.19	96	100
3. CG-INS	0.43	0.18	0.83	100	100

(b) Vertical Error Statistics for QUIN dataset.

Scenario	Mean	Std. Dev	Max	Prob. of $e^a_{v_{k,0}}$	
				$< 2m$	$< 3m$
1. LS	4.12	2.60	8.47	30	37
2. PVA	0.80	1.02	4.05	93	99
3. CG-INS	0.84	0.61	2.71	95	100

Statistics quantifying the performance of each algorithm are summarized in Table 5.4. Each row of tables corresponds to one of the datasets listed in Table 5.3. The left column of tables contains statistics for the horizontal position error. The right column of tables contains statistics for the vertical position error. The statistics in each table are as follows. Column 1 shows the algorithm number a and name. Column 2 displays the mean norm of the position error. Column 3 contains the standard deviation of the norm of the position error. Column 4 shows the maximum value of the norm of the position error. Columns 5 and 6 report the percentage of samples for which the norm of the positioning error is less than the accuracy specified in the column header.

Both the histogram and the tables show that, for the HNTP and QUIN datasets, the INS results exceed the SAE specification [12]. The INS, which has more information, performs better than LS and PVA approaches. The INS performance is expected to carryover to datasets for moving platforms, because the job of the IMU/INS is to remove the mean motion of the platform. The performance of the PVA approach may be distinct for each moving platform dataset, depending on the extend to which the platform motion matches the design assumptions of the PVA estimation approach [123].

5.2.3 Dynamic Experimental Results

This section includes descriptions of the data set that will be used for analysis, metrics to understand the quality of the available GNSS data, metrics for assessing algorithm performance, the employed algorithm, acquired data set, performance analysis of the aforementioned PPP-INS algorithm and effect of sensor (i.e. IMU, GNSS) measurement quality in rover positioning. The main purpose is to analyze the algorithm's ability to achieve either SAE specification [12] or yet, a one-meter horizontal positioning accuracy requirement for moving platform using L1 real-time PPP GPS data.

Data Acquisition and Ground Truth Trajectory

For data acquisition, the hardware was mounted on a sedan that was driven repeatedly along a multi-block section of an urban street (Columbia Ave. near the intersection with Iowa Avenue in Riverside, CA) with low buildings and trees adjacent to the street. The trajectory encompasses two U-turns, one at each end, and therefore also includes acceleration, deceleration and turn rates typical for urban trajectories. The experiment lasted 40 minutes. The experimental data were saved for post-processing so that algorithmic analysis could be performed.

The PPP information, required to compensate the common-mode errors was collected from external sources. The satellite orbit, clock model parameters were collected from IGS-RTS using the BNC software. The ionospheric delay model parameters were obtained from US-TEC [55] real-time data. Tropospheric error was corrected using the UNB3M model [96]. Satellite hardware bias was obtained from CODE service.

The on-vehicle experimental hardware included two GNSS receivers and one IMU. One receiver was a single frequency u-Blox ZED-F9P (consumer grade) and the other was a dual frequency NOVATEL OEMV2 (survey grade). Both receivers were connected to the same Antcomm ANN-MS-0-005 antenna. The ZED-F9P single-frequency receiver provided GNSS data that is used for PPP GPS state estimation. The OEMV2 provided data that was used to establish the ground-truth trajectory. The IMU sensor was an NV-IMU 1000.

Ground truth trajectory estimation was performed in post-processed, using a Maximum a Posteriori (MAP) smoothing algorithm [148]. It used the OEMV2 two-frequency pseudorange and integer-resolved, carrier phase GNSS data and NV-IMU 1000 data to estimate the ground truth trajectory with centimeter accuracy. This ground truth trajectory and OEMV2 data are only used to assess the accuracy of the state estimates achieved using only the IMU and consumer-grade ZED-F9P receiver.

GNSS Data Quality Metrics

For state estimation by PPP GPS aided INS, an important item to consider is the quality of the PPP GPS data versus time. Relevant factors include the number and geometry of the satellites available to the receiver and the quality of the range measurements as affected by local factors (e.g., multipath, foilage). To assess these items we consider the following quality indicators.

Geometric Dilution of Precision (GDOP) quantifies the geometry of the user-to-satellite line-of-sight vectors at time instant k [20, 109, 142]. $GDOP_k$ is computed as

$$GDOP_k = \sqrt{trace(\mathbf{A}_k^T \mathbf{A}_k)^{-1}} \tag{5.24}$$

where $\mathbf{A}_k$ is the matrix constructed by stacking the vectors $[\mathbf{h}_r^s,\ 1]$ from all available satellites, where $\mathbf{h}_r^s$ is defined in eqn. (2.9). Larger GDOP values indicate worse geometric diversity and larger covariance of the Least Squares position error covariance matrix.

At each GPS epoch for which there are at least five satellites available, the L1 PPP corrected pseudorange measurements defined in eqn. (3.28) will be solved using iterated nonlinear least squares to estimate the vector $\mathbf{x}\doteq[\mathbf{p}_r^T, ct_r, A_v]^T \in \Re^5$ where $\mathbf{p}_r \in \Re^3$, $ct_r \in \Re^1$ and $A_v \in \Re^1$ denote rover position, receiver clock bias and residual vertical atmospheric delay. At each GPS epoch for which there are only four satellites available, the vector is defined as $\mathbf{x}\doteq[\mathbf{p}_r^T, ct_r]^T \in \Re^4$ where residual vertical atmospheric delay is dropped.

At the conclusion of the *PPP least squares (PPP-LS)* process at epoch k, the measurements residual r_k^s for $s = 1, \ldots, m$ indicate the extend to which LS adjustment of $\hat{\mathbf{x}}_k$ was able to match the set of measurements at that epoch. Each $|r_k^s|$ indicates the degree to which that measurement conformed to the measurement model, given the full set of measurements. One indicator of the quality of a set of m measurements is the *risk* r_k computed as

$$r_k = \frac{1}{m} \sum_{s=1}^{m} |r_k^s|. \tag{5.25}$$

The symbol m indicates the number of available measurements at epoch k.

Table 5.7: IMU sensor noise parameter.

Sensor Type	Acc. N_a	Acc. B_a	Gyro. N_g	Gyro. B_g
TG	0.001	0.0002	0.0033	0.0006
CG	0.010	0.0010	0.0333	0.0042
NV-IMU 1000	0.003	0.0003	0.0011	0.0006
Unit	$m/s^{3/2}$	m/s^2	$\deg/s^{1/2}$	$\deg/s$

The PPP-LS state estimates are point-wise, without any filtering. The above risk quantification is computed using PPP-LS residuals, not INS residuals, to allow each epoch to be assessed independently of other epochs. While small risk does not necessarily indicate a good set of measurements (i.e., it may be possible for LS to find an estimate to perfectly fit four low quality measurements), large risk r_k does indicate that something is wrong with the set of measurements available at epoch k.

IMU Sensor Parameters and Noise Corruption

The PPP-INS implementation uses IMU data. Authors tend to grade IMU sensors into five different categories, according to their accuracy and price: (a) marine (b) navigation (c) intermediate (d) tactical and (e) consumer or automotive. Among all these categories, ground vehicle applications generally use tactical to consumer-grade IMU sensors [65]. Thus, this paper's discussion focuses on the latter.

Table 5.7 shows different IMU grades and their typical random-walk N and bias instability B parameters [65]. The first and second rows represent tactical and consumer-grade IMUs respectively. The last row describes the on-board sensor's (NV-IMU 1000) specifications. In Table

Table 5.8: Selected IMU sensor parameters.

Parameter	N_a	B_a	N_g	B_g
IMU1	0.004	0.0004	0.003	0.0006
IMU2	0.007	0.0007	0.016	0.0025
IMU3	0.011	0.0010	0.033	0.0042
Unit	$m/s^{3/2}$	m/s^2	$\deg/s^{1/2}$	$\deg/s$

5.7, subscript ‘a’ refers to accelerometers and subscript ‘g’ to gyroscopes. The noise coefficients of NV-IMU 1000 indicate that its accelerometers lie in between tactical and consumer-grade and the gyroscopes can be labeled as tactical-grade.

Three different sensor specifications were selected for this experimental Section to showcase the effect of IMU quality in algorithm performance. They were labeled as IMU1, IMU2 and IMU3 and their parameters are presented in Table 5.8. In current setup, IMU3 was considered as a consumer-grade sensor for both accelerometer and gyroscope. These sensors data were generated by corrupting NV-IMU 1000 data with additive stochastic errors derived from Table 5.8 specifications. ASD plots of these sensors (IMU1, IMU2 and IMU3) are presented in Fig. 5.5 and 5.6. For delineating these ASD plots, state space model based stochastic errors were computed with parameters from Table 5.8. The details of error generation methodology are described in [54].

Positioning Performance

Figure 5.7 shows two histograms of $e_h^a(k)$ as defined in eqn. (5.18).The top figure is generated using IMU1 sensor and the bottom one, using IMU3. The plots are generated using $N_d = 2400$ epochs.

Tables 5.9 and 5.10 summarize various measures of positioning accuracy for horizontal

Sensor	Mean	Std. Dev	Max	Prob. of e_{h_k}		
	m	m	m	$< 1m$	$< 1.5m$	$< 2m$
IMU1	0.79	0.40	2.88	70.6	94.5	99.3
IMU3	0.80	0.41	2.89	71.0	94.5	99.4

Table 5.9: Horizontal Error Statistics.

Sensor	Mean	Std. Dev	Max	Prob.	
	m	m	m	$e_{v_k} < 2m$	$e_{v_k} < 3m$
IMU1	2.32	1.14	5.26	36.2	75.5
IMU3	2.32	1.13	5.29	36.4	75.2

Table 5.10: Vertical Error Statistics.

(e_h) and vertical errors (e_v), respectively. Column 1 indicates the IMU grade used in the algorithmic implementation, column 2 displays the mean position error, column 3 contains the standard deviation, and column 4 shows the maximum value. Columns 5 and 6 report the percentage of samples that have a positioning error less than the accuracy specified in the column header.

The results in Table 5.9 and 5.10, show that the accuracy of the investigated sensors (consumer- and tactical-grade IMUs) satisfy the SAE J2945 specification. Moreover, the performance of both sensors proved to be similar for this particular dataset. Therefore, regardless of the IMU quality PPP-INS results are comparable. Performance divergence might only become more apparent for larger epoch periods or in situations where GNSS measurements became unavailable for longer periods of time (10s of seconds). This discussion is further investigated in Section 5.2.4.

5.2.4 IMU Data Quality Analysis

The divergence in performance between different IMU grades becomes more apparent over time periods of longer duration between update epochs. Therefore, in this section, PPP GPS epoch period is varied from 5 to 60 seconds. For each value of T, the analysis performs a Monte

Carlo experiment with $M = 40$ iterations. For one iteration, a sample of IMU noise is produced and scaled for IMU1, IMU2 and IMU3 (same noise sequence, different scaling).

In this demonstration, two experiments have been conducted. Each experiment was divided into two trials. In trial T1, only accelerometer was perturbed with additional stochastic error. In trial T2, only gyroscope additional error is enforced. In Monte Carlo Experiment 1, at $t = KT$, the state and covariance were updated using ground truth information. In Monte Carlo Experiment 2, at $t = KT$, an EKF based state update method was utilized to estimate state and covariance. In each trial, the first 700 seconds of the aforementioned dataset was utilized. The rover horizontal position error was computed at 200 Hz frequency. Therefore, the mean of the horizontal position error was computed with 140000 samples for each update period of every Monte Carlo run.

In Section 4.9.3 of [49], the error variance of the vehicle position state is described as

$$P_p(t) = (P_{p_0} + P_{v_0}t^2 + P_{b_0}\frac{t^4}{4}) + (\sigma_{\gamma_a}^2\frac{t^3}{3} + \sigma_{b_a}^2\frac{t^5}{20}) \tag{5.26}$$

The first three terms of the above mentioned equation (P_{p_0}, P_{v_0} and P_{b_0}) are the error variances of position, velocity and accelerometers bias state after GNSS observation update. The remainder two terms $\sigma_{\gamma_a}^2$ and $\sigma_{b_a}^2$ are the stochastic noise of IMU sensors mentioned in Section 4.1. In Experiment 1, first parenthesis enclosed terms of eqn.(5.26) becomes zero after each epoch update. Therefore, position error is affected by only the second parenthesis enclosed terms of eqn.(5.26) which is the IMU sensor stochastic noise. For Experiment 2, the terms related to the state vector of eqn.(5.26) gets updated using GNSS measurement. As a result in Experiment 2, position error is affected by both IMU sensor noise as well as update measurement quality.

Figures 5.8 and 5.9 show the mean horizontal position error for trials T1 and T2 of Experiment 1 respectively. Fig. 5.10 shows the rover positioning performance of Experiment 2 with both trial results plotted together. Solid lines are used for demonstrating accelerometer performance and dashed lines indicate gyroscope accuracy in these figures. The blue, red and green indicate IMU1, IMU2 and IMU3 respectively.

In Figs. 5.8 to 5.10, the mean horizontal position error increases with the increase of the update period. Fig. 5.8 and 5.9, in particular, show that, average sub-meter positioning is maintained up to 35 seconds and 2 meter accuracy for 42 seconds. For Experiment 2, the CG sensors (green curve) sustain sub-meter accuracy up to 17 seconds for accelerometers but only 8 seconds for gyroscopes.

From these results it can be summarized that achievement and sustenance of meter-level accuracy is mostly dependent on the GNSS update frequency and measurement quality; In other words, positioning performance is more dependent on GNSS availability and measurement quality, than on IMU grade. Additionally, and as expected, rover performance proves to be affected more adversely by gyroscopes quality rather than by accelerometers quality.

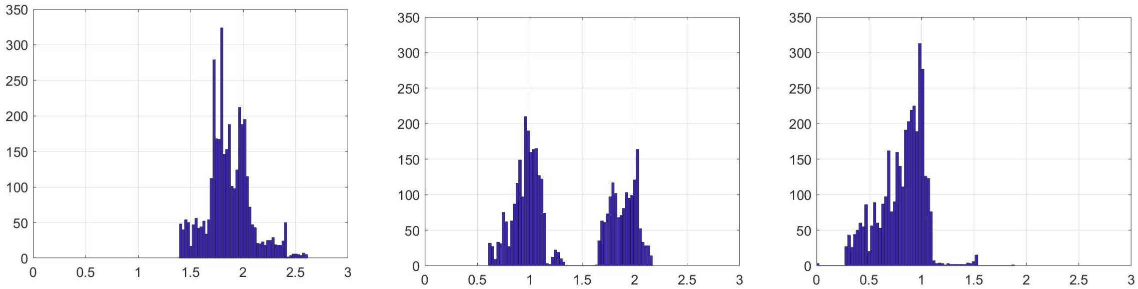

(a) LS for BRMU dataset (b) PVA for BRMU dataset (c) INS for BRMU dataset

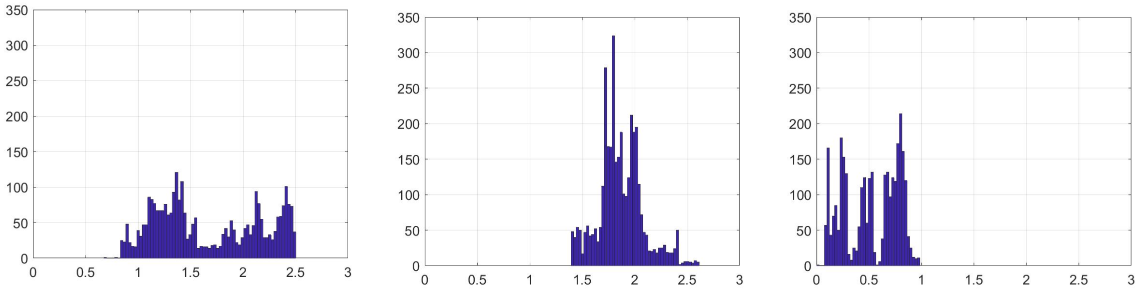

(d) LS for HNTP (e) PVA for HNTP (f) INS for HNTP

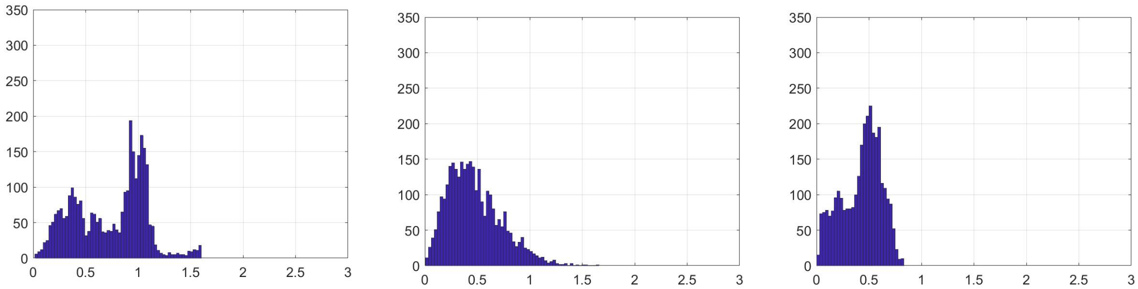

(g) LS for QUIN (h) PVA for QUIN (i) INS for QUIN

Figure 5.4: Histogram plots of the horizontal position error for the datasets described in Table 5.3.

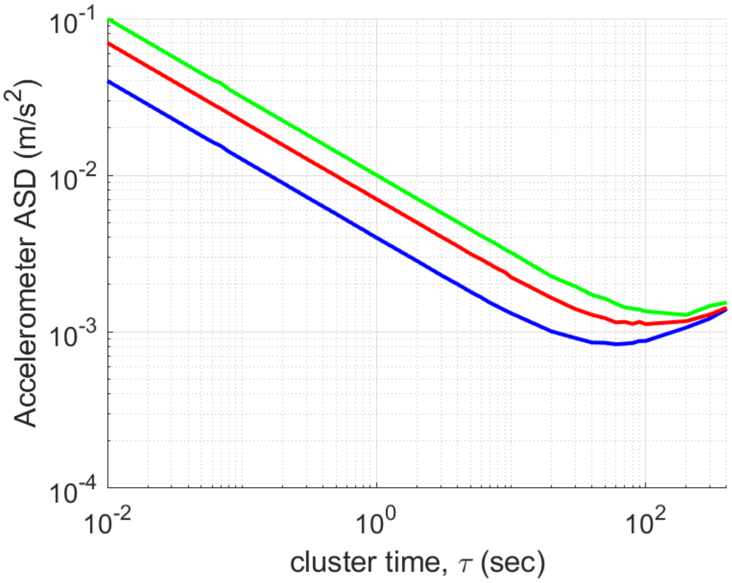

Figure 5.5: ASD plots of accelerometers mentioned in Table 5.8 (blue, red and green indicates IMU1, IMU2 and IMU3 respectively)

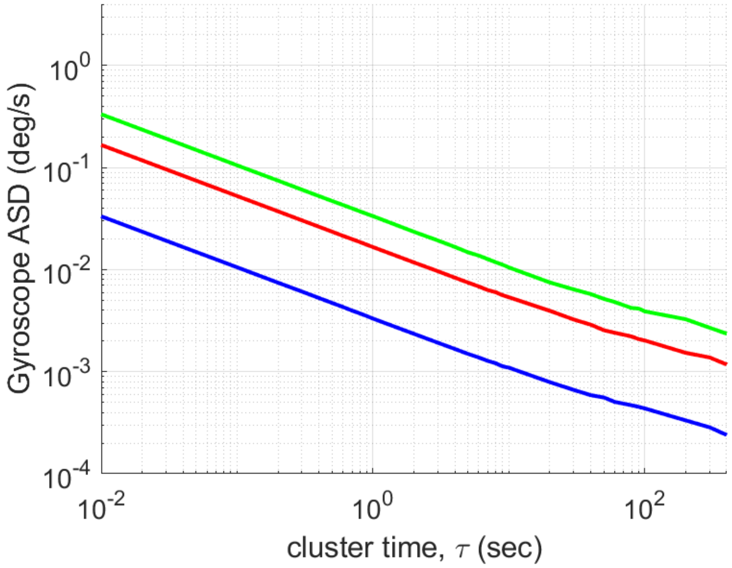

Figure 5.6: ASD plots of gyroscopes mentioned in Table 5.8 (blue, red and green indicates IMU1, IMU2 and IMU3 respectively)

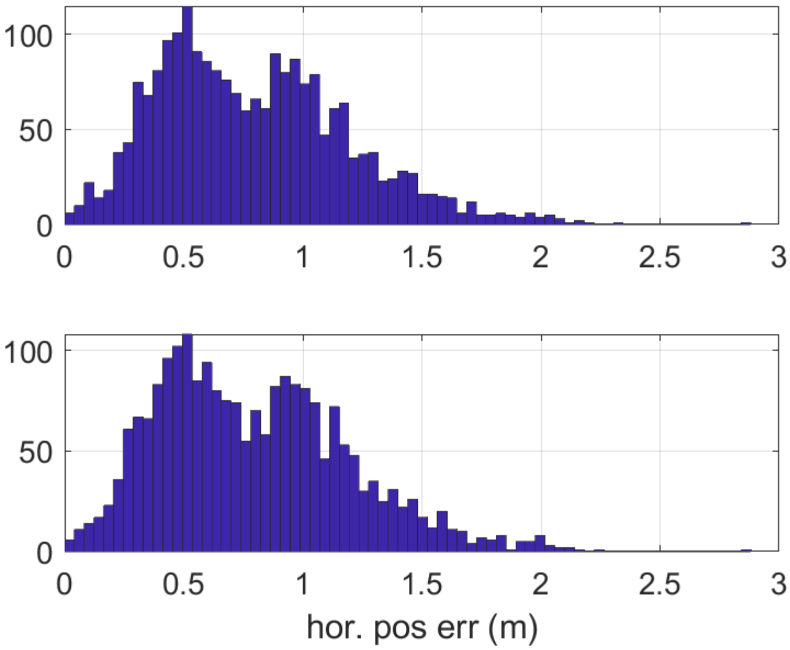

Figure 5.7: Histogram of horizontal position error $e^a_{h_k}$ defined in eqn. (5.18) for PPP-INS using IMU1 (Top) and IMU3 (Bottom) sensors.

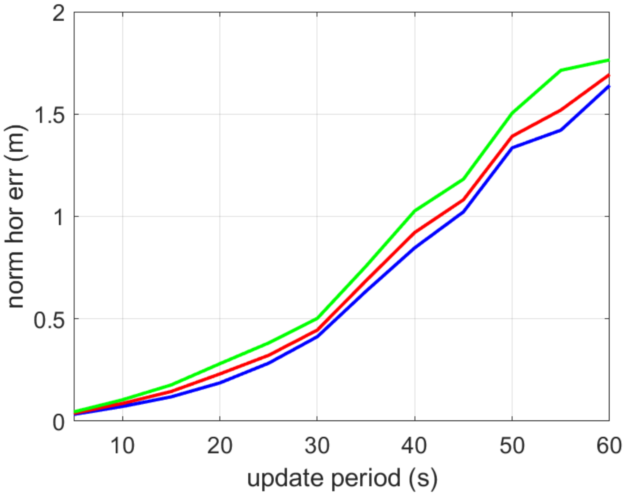

Figure 5.8: Mean of horizontal error vs update period for T1 of Exp1. Blue, red and green indicate sensor IMU1, IMU2 and IMU3 respectively.

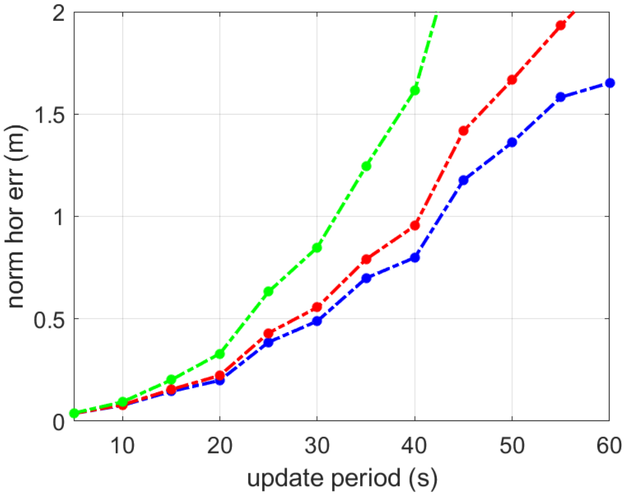

Figure 5.9: Mean of horizontal error vs update period for T2 of Exp1. Blue, red and green indicate sensor IMU1, IMU2 and IMU3 respectively.

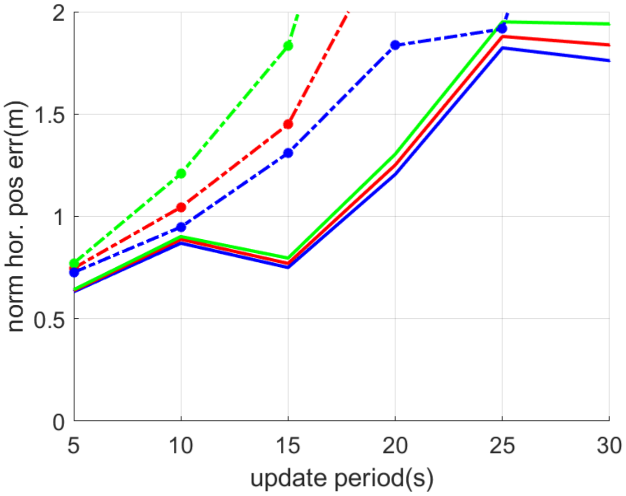

Figure 5.10: Mean of horizontal error vs EKF update period. Blue, red and green indicate IMU sensor 1, 2 and 3 respectively. The solid lines show accelerometer (T1) and dashed lines indicate gyroscope (T2) performance.

Chapter 6

Conclusions

Successful commercial implementation of Connected Autonomous Vehicle (CAV) application involves low-cost sensors, real-time corrections, data communication services, sensor information incorporation and reliable estimation algorithms.

The article provides a DGNSS correction algorithm able to compensate latency, short-term communication interruption, and lost packets. The article also provides estimation algorithms able to use the DGNSS corrections to exceed the SAE specifications. The PVA and INS methods herein both augment one multipath state per satellite and use Doppler measurements along with pseudorange. The research described in this article demonstrated that: (1) with suitable algorithmic processing, positioning performance is insensitive to correction latency up to 500 s; and (2) horizontal position estimation accuracy is achievable at the submeter level for over 98% of samples. The data sets used herein were urban, but had a relatively open view of the sky. They were not acquired in urban canyon type settings. The performance demonstrated herein would not be achievable in urban canyons using GNSS alone; instead, to maintain positioning accuracy, alternative sensors would be required.

This paper also focused on assessing the factors that affect the ability to achieve meter-level vehicle positioning accuracy with consumer-grade sensors, real-time Precise Point Positioning (RT-PPP) correction services and integration of Inertial Measurement Unit(IMU) with Global Navigation Satellite System(GNSS) measurement.

The paper presented and discussed: GNSS and IMU sensor measurement models, DGNSS correction latency computation methodology, RT-PPP correction computation methodology, atmospheric error models suitable for North America users, description of a real-time PPP implementations and demonstration of sub-meter positioning performance accuracy for moving platforms in a challenging environment. The investigated PPP-INS algorithm achieved mean horizontal position error of 0.79 m with standard deviation of 0.40 m. The horizontal position was accurate to 1.0 m accuracy at 71% and 2 m at 99.4%. The vertical position accuracy was accurate to 3 m at 75.5% of probability. This performance metrics met the SAE J2945 specification, proposed for intelligent automotive applications. Sub-meter accuracy was maintained up to 8 seconds of epoch period in an Extended Kalman Filter (EKF) setup for consumer-grade IMU.

The concluding remarks of this study are: rover positioning performance depends on PPP correction accuracy and IMU and GNSS sensor quality. GNSS data affected with outliers and signal outage, degrade positioning accuracy. Rover performance is quite similar for IMU sensor qualities when the update period is limited to one second. However, as the update period increases, their errors start to become distinguishable. Another remarkable observation is that rover performance is affected more adversely by gyroscope stochastic errors than by accelerometers.

Incorporation of other GNSS constellations (GLONASS, Beidou, GALILEO) along with robust outlier detection algorithm will improve rover's positioning performance. Implementation of PPP for multi-constellation systems and the utilization of innovative measurement selection algorithms [4] are two important topics for future research.

Chapter 7

Appendix

7.1 WADGNSS Correction Estimation

The appendix discusses an example approach for the implementation of Strategy B as defined in Section 3.3.2. The approach is strongly motivated by [46,81] which document a precursor study leading to WAAS.

WADGNSS Reference Station Processing. Receiver r provides code and carrier phase measurements for each satellite s and frequency f. These measurements are, respectively denoted by $\phi^s_{r,f}$ and $\rho^s_{r,f}$ where the value of f is either $L1$ or $L2$. The models for these measurements are given by eqns. (2.1–2.4). The second line of each equation contains the common-mode errors which should be removed by differential processing. All the error terms enter all four equations in an identical manner with the exception of the ionospheric terms. Also, the number of unknown quantities can be reduced by noting that the two ionospheric delay terms I^s_{L1} and I^s_{L2} in these four equations are both related (to first-order) to the slant total electron count (TEC) along the signal pathway from satellite

s to reference station r by the equations

$$I^s_{L1} = \frac{40.3}{f^2_{L1}}\,TEC \quad \text{and} \quad I^s_{L2} = \frac{40.3}{f^2_{L2}}\,TEC. \tag{7.1}$$

Therefore, the ionospheric delay will be compensated by estimating a parameterized function that maps to TEC, which is then used to compute I^s_{L1} and I^s_{L2} using eqns. (7.1).

One set of strategies [46,62,73,115,116,130,139,150] starts by separating the TEC from the other portions of eqns. (2.1–2.4) while also reducing the effects of noise and multipath. Some articles [39, 117, 137] propose employing the Hatch filter [68]. The approach of Enge *et al.* [46] builds on an idea from [61] by using changes in the carrier measurements to estimate changes in the pseudorange and ionosphere. The changes in carrier measurements

$$\delta\phi^s_{r,f}(n) = \phi^s_{r,f}(n) - \phi^s_{r,f}(n-1) \tag{7.2}$$

remove the need to estimate the (constant) carrier integer ambiguities which cancel in the time difference as long as there is no loss of phase-lock. The symbol f signifies the measurement frequency which can be $L1$ or $L2$. This dual-frequency carrier-smoothing filter is based on the following observation equation,

$$\begin{bmatrix} \tilde{\rho}^s_{r,L1} \\ \delta\phi^s_{r,L1} \\ \tilde{\rho}^s_{r,L2} \\ \delta\phi^s_{r,L2} \end{bmatrix} \doteq \begin{bmatrix} 1 & 0 & \frac{40.3}{f^2_{L1}} & 0 \\ 0 & 1 & 0 & -\frac{40.3}{f^2_{L1}} \\ 1 & 0 & \frac{40.3}{f^2_{L2}} & 0 \\ 0 & 1 & 0 & -\frac{40.3}{f^2_{L2}} \end{bmatrix} \begin{bmatrix} \bar{\rho}^s_r \\ \delta\bar{\rho}^s_r \\ TEC^s_r \\ \delta TEC^s_r \end{bmatrix} + \nu^s_r \tag{7.3}$$

where

$$\bar{\rho}^s_r = R(\mathbf{p}_r, \mathbf{p}^s) + ct_r - ct^s + T^s \tag{7.4}$$

and ν_r^s is a noise vector that accounts for the cumulative effects of multipath and receiver noise, which are both assumed to be zero mean and uncorrelated. The quantity $\delta\bar{\rho}_r^s$ in the right-hand side of eqn. (7.2) is the change in $\bar{\rho}_r^s$ between two consecutive epochs n and $n-1$:

$$\delta\bar{\rho}_r^s = \bar{\rho}_r^s(n) - \bar{\rho}_r^s(n-1) \tag{7.5}$$

The ρ quantities on the left-hand side (i.e., $\tilde{\rho}_{r,L1}^s$ and $\tilde{\rho}_{r,L2}^s$) are the calibrated measurements after the receiver and satellite hardware bias estimates have been removed:

$$\tilde{\rho}_{r,L1}^s = \rho_{r,L1}^s - c\hat{b}_{r_{L1,\rho}} + c\hat{b}_{L1,\rho}^s \tag{7.6}$$

$$\tilde{\rho}_{r,L2}^s = \rho_{r,L2}^s - c\hat{b}_{r_{L2,\rho}} + c\hat{b}_{L2,\rho}^s. \tag{7.7}$$

Alternative approaches to estimate the ionosphere time delays in the presence of receiver and satellite hardware biases are described in [62, 73, 115, 116, 130, 139, 150].

For each satellite, eqn. (7.3) is used as the measurement equation for either least squares or a simple Kalman filter designed to attenuate the effects of noise and multipath. The state vector for each filter includes: $\bar{\rho}_r^s$, $\delta\bar{\rho}_r^s$, TEC_r^s, and δTEC_r^s.

The symbol TEC_r^s in eqn. (7.3) represents the slant TEC for receiver r and satellite s. This is the cumulative delay experienced by the signal on its non-vertical path through the ionosphere, which is unique for each satellite and receiver. The ionospheric delay map will model the vertical TEC at the ionospheric pierce point of the signal. The conversion of vertical to slant TEC is

$$TEC_r^s = F(E_r^s)\, TEC_v(p_{p_r}^s) \tag{7.8}$$

by use of the ionospheric obliquity factor $F(E_r^s)$

$$F(E_r^s) = \frac{1}{\sin(E_{p_r}^s)} = \frac{1}{\sqrt{1 - \left[\frac{r_e \cos(E_r^s)}{r_e + h_m}\right]^2}} \tag{7.9}$$

where E_r^s is the elevation angle for satellite s at receiver r, $E_{p_r}^s$ is the local elevation angle at the pierce point $p_{p_r}^s$, r_e is the average radius of the Earth, and h_m is the height of the maximum electron density (assumed to be 350 km). After the slant ionospheric delays for all satellites in view for the reference station have been smoothed and converted to vertical delay estimates, they are sent to the master station for further processing.

The symbol $\bar{\rho}_r^s$ in eqn. (7.3) represents the *iono-free smoothed pseudorange estimate*. This quantity must be compensated for tropospheric delays before being used to estimate the satellite clock and satellite position error vector. The tropospheric delay is a function of elevation angle, pressure, temperature and humidity (see Chapter 1 of [118]) . The literature provides many models for tropospheric delay estimate [72, 96, 129, 152]. One of these models (e.g. UNB3M [96]) is implemented and used to compensate the $\bar{\rho}_r^s$ for the predictable portion of tropospheric effects. After compensating for the atmospheric (i.e., ionospheric and tropospheric) delays, smoothed pseudorange are sent to the master station.

WADGNSS Master Station Algorithms. The master station accumulates the data from all base stations for all satellites. It then assembles a vector of the vertical TEC's that it uses to estimate the TEC map as a function of the pierce point $p_{p_r}^s$. Separately it assembles a vector of the atmospheric-free smoothed pseudoranges that it uses to estimate the satellite clock and position error vectors.

Estimation of Ionospheric TEC Grid Map: Each reference station's computed TEC is organized as a vector:

$$\tilde{\mathbf{I}}_r^S = \begin{bmatrix} TEC_r(p_{p_r}^{s_1}) \\ TEC_r(p_{p_r}^{s_2}) \\ \vdots \\ TEC_r(p_{p_r}^{s_M}) \end{bmatrix} \tag{7.10}$$

In this document, for simplicity of notation, we assume that there are total M satellites in view from all reference stations.

The master station receives the TEC vectors $\tilde{\mathbf{I}}_r^S$ from N reference stations, so $r = 1, \ldots, N$. This reference station data is concatenated to form a large measurement vector,

$$\tilde{\mathbf{I}}^S = \begin{bmatrix} \tilde{\mathbf{I}}_{r_1}^S \\ \tilde{\mathbf{I}}_{r_2}^S \\ \vdots \\ \tilde{\mathbf{I}}_{r_N}^S \end{bmatrix} \doteq \mathbf{I}^S + \varepsilon^S \tag{7.11}$$

which is interpreted as the true ionospheric delay vector $\mathbf{I}^S$ plus a measurement error vector ε^S. The vector of measurements $\tilde{\mathbf{I}}^S$ will be used to maintain a vertical TEC map function.

The vertical TEC map is constructed using a grid of vertical TEC values denoted by the vector $\mathbf{I}^G$ [40, 41, 85]. The value of the k-th element of $\mathbf{I}^G$ represents the vertical TEC at a pierce point p_{p_k}. The set of points $\{p_{p_k}\}_{k=1}^K$ forms a regular grid. The vertical TEC at an arbitrary pierce point p_p within the geographical extent of the grid points is computed as a linear function of the values at the grid points:

$$TEC_v(p_p) \ = \ \mathbf{w}(p_p)\mathbf{I}^G \tag{7.12}$$

where $\mathbf{w}(p_p)$ is a vector of weights. The k-th element of the weight vector $w_k = [\mathbf{w}(p_p)]_k$ shows how much the vertical TEC value $[I^G]_k$ at the k-th grid point p_{p_k} contributes to the value of the TEC at the desired pierce point p_p.

The elements of $\mathbf{w}(p_p) = [w_1, \ldots, w_K]$ should satisfy a few constraints. The first constraint is that $\sum_{i=k}^{K} w_k = 1$, so that eqn. (7.12) interpolates the value for $TEC(p_p)$ from the TEC values at the grid points. A second constraint is that when $p_p = p_{p_k}$ the vector $\mathbf{w}(p_{p_k})$ should be all zero except for a single one as the k-th element. This causes $TEC(p_p)$ to evaluate to match the k-th element of the vector $\hat{\mathbf{I}}^G$. A third constraint is that the k-th element $[\mathbf{w}(p_p)]_k$ should decrease smoothly as $d_k = \|p_p - p_{p_k}\|$ increases. This results in a smooth interpolation between the grid point values. One example choice of the weighting function is the inverse distance approach [46], where the weights are selected as

$$a_k = 1/d_k \text{ and } w_k = \frac{a_k}{\sum_{i=1}^{K} a_i}$$

which requires special treatment for the case where $d_k = 0$.

The vector of measurements $\tilde{\mathbf{I}}^S$ defined in eqn. (7.11) will be used to estimate the TEC values at the grid points (i.e., $\mathbf{I}^G$). The i-th element of $\tilde{\mathbf{I}}^S$ corresponds to a pierce point p_{p_i}. For accurate estimation of the TEC map, this set of pierce points should be well distributed throughout the geographic region defined by the grid points. Using eqn. (7.12) allows calculation of a weight matrix $\mathbf{W}$ with rows defined by $\mathbf{w}(p_{p_i})$ such that the measurements relate to the grid values as

$$\tilde{\mathbf{I}}^S \doteq \mathbf{W}\mathbf{I}^G + \varepsilon^S. \tag{7.13}$$

The value of $w_{i,k} = [\mathbf{W}]_{i,k}$ is the element in the i-th row of the k-th column of matrix $\mathbf{W}$, which represents the interpolation weight from the k-th grid point at the i-th pierce point.

If the spatial distribution of the pierce points results in the matrix $\mathbf{W}$ being full column rank, then eqn. (7.13) could be solved as

$$\hat{\mathbf{I}}^G \doteq (\mathbf{W}^T \mathbf{W})^{-1} \mathbf{W}^T \tilde{\mathbf{I}}^S. \tag{7.14}$$

Alternatively, either constraints could be added to ensure that a unique and smooth solution exists or eqn. (7.13) could be used as the measurement equation for a Kalman filtering approach to allow information accumulation and noise reduction over time [22].

Estimation of Satellite Orbit and Clock Corrections: The satellite orbit and clock correction vectors are estimated by the master station using the atmospheric-free smoothed pseudorange vectors from all reference base stations.

Based on eqn. (7.4), the atmospheric-free smoothed pseudorange between reference station r to satellite s is

$$\bar{\rho}_r^s \doteq R(\mathbf{p}_r, \mathbf{p}^s) + ct_r - ct^s + w_r^s. \tag{7.15}$$

This measurement is based on the actual satellite position, not the computed satellite position using on the ephemeris data. These two items are related to each other by $\mathbf{p}^s = \hat{\mathbf{p}}^s + \delta\mathbf{p}^s$ where $\hat{\mathbf{p}}^s$ is the calculated satellite location and $\delta\mathbf{p}^s$ is satellite position error vector.

The range can be equivalently represented as a dot product

$$\begin{aligned} R(\mathbf{p}_r, \mathbf{p}^s) &= \mathbf{e}_r^s \cdot [(\hat{\mathbf{p}}^s + \delta\mathbf{p}^s) - \mathbf{p}_r] \\ &= \mathbf{e}_r^s \cdot \delta\mathbf{p}^s + \mathbf{e}_r^s \cdot (\hat{\mathbf{p}}^s - \mathbf{p}_r) \end{aligned} \tag{7.16}$$

where $\mathbf{e}_r^s = \frac{\mathbf{p}_r - \mathbf{p}^s}{\|\mathbf{p}_r - \mathbf{p}^s\|}$ is the unit vector from satellite s to reference station r; and w_r^s is the atmospheric-free smoothed pseudorange estimation error. Since the quantity $(\hat{\mathbf{p}}^s - \mathbf{p}_r)$ is known for the reference sations, it can be removed by defining a new variable

$$y_r^s = \bar{\rho}_r^s - \mathbf{e}_r^s \cdot (\hat{\mathbf{p}}^s - \mathbf{p}_r). \tag{7.17}$$

Combining the above equations yields the measurement model

$$y_r^s \doteq \mathbf{e}_r^s \cdot \delta\mathbf{p}^s + ct_r - ct^s + w_r^s. \tag{7.18}$$

where $r = 1,\ldots,N$ counts over reference stations and $s = 1,\ldots,M$ counts over GNSS satellites.

The master station will estimate the vector

$$\mathbf{x} = \begin{bmatrix} \delta\mathbf{p}^T & \mathbf{B}^T & \mathbf{b}^T \end{bmatrix}^T, \tag{7.19}$$

where for $\delta\mathbf{p}^s \in \Re^3$

$$\begin{aligned} \delta\mathbf{p} &= \begin{bmatrix} (\delta\mathbf{p}^1)^T & (\delta\mathbf{p}^2)^T & \ldots & (\delta\mathbf{p}^M)^T \end{bmatrix}^T \in \Re^{3M}, \\ \mathbf{B} &= \begin{bmatrix} ct^1 & ct^2 & \ldots & ct^M \end{bmatrix}^T \in \Re^M, \\ \mathbf{b} &= \begin{bmatrix} ct_1 & ct_2 & \ldots & ct_N \end{bmatrix}^T \in \Re^N. \end{aligned}$$

Using this definition of $\mathbf{x}$ and eqn. (7.18), the vector of measurements for the m_r satellites at reference station r, denoted as $\mathbf{y}_r$, can be organized as

$$\mathbf{y}_r \doteq \begin{bmatrix} \mathbf{E}_r & -\mathbf{I}_r & \mathbf{1}_r \end{bmatrix} \mathbf{x} + \mathbf{w}_r. \tag{7.20}$$

The matrix $\mathbf{E}_r \in \Re^{m_r \times (3M)}$ is compose of rows that are all zeros, with the exception that in each row, where the i-th row corresponds to $y_r^{s_i}$, the row vector $\mathbf{e}_r^{s_i}$ will be in the columns corresponding to $\delta\mathbf{p}^{s_i}$. The matrix $\mathbf{I}_r \in \Re^{m_r \times M}$ is composed of rows that are all zeros with the exception that in the i-th row corresponding to $y_r^{s_i}$ there is a one in the column corresponding to ct^{s_i}. The matrix $\mathbf{1}_r \in \Re^{m_r \times N}$ is composed of rows that are all zeros with the exception that in each row there is a one in the column corresponding to ct_r. For example, if reference station $r = 3$ was receiving satellites

1 and 4, then

$$\mathbf{E}_3 = \begin{bmatrix} (\mathbf{e}_r^1)^T & \mathbf{0} & \mathbf{0} & \mathbf{0} & \mathbf{Z}_{3(M-4)} \\ \mathbf{0} & \mathbf{0} & \mathbf{0} & (\mathbf{e}_r^4)^T & \mathbf{Z}_{3(M-4)} \end{bmatrix},$$

$$\mathbf{I}_3 = \begin{bmatrix} \mathbf{1} & \mathbf{0} & \mathbf{0} & \mathbf{0} & \mathbf{Z}_{M-4} \\ \mathbf{0} & \mathbf{0} & \mathbf{0} & \mathbf{1} & \mathbf{Z}_{M-4} \end{bmatrix},$$

$$\mathbf{1}_3 = \begin{bmatrix} \mathbf{0} & \mathbf{0} & \mathbf{1} & \mathbf{0} & \mathbf{0} \\ \mathbf{0} & \mathbf{0} & \mathbf{1} & \mathbf{0} & \mathbf{0} \end{bmatrix},$$

where $\mathbf{Z}_p \in \Re^{1\times p}$ is a row vector with all zeros. The matrix $\mathbf{1}_3$ consists of all zeros except the third column that is 1.

Concatenating the measurements from all the reference stations provides a measurement equation of the form

$$\mathbf{y} \doteq \mathbf{H}\mathbf{x} + \mathbf{w} \tag{7.21}$$

where

$$\mathbf{y} = \begin{bmatrix} \mathbf{y}_1 \\ \mathbf{y}_2 \\ \vdots \\ \mathbf{y}_N \end{bmatrix}, \quad \mathbf{H} = \begin{bmatrix} \mathbf{E}_1 & -\mathbf{I}_1 & \mathbf{1}_1 \\ \mathbf{E}_2 & -\mathbf{I}_2 & \mathbf{1}_2 \\ \vdots & \vdots & \vdots \\ \mathbf{E}_N & -\mathbf{I}_N & \mathbf{1}_N \end{bmatrix}, \text{ and } \mathbf{w} = \begin{bmatrix} \mathbf{w}_1 \\ \mathbf{w}_2 \\ \vdots \\ \mathbf{w}_N \end{bmatrix}.$$

The master station can solve eqn. (7.21) by a variety of methods (e.g., batch least squares). If there are more measurements than unknowns in the WADGNSS network, the system of equations is over-determined. The least squares solution is

$$\hat{\mathbf{x}} = (\mathbf{H}^T\mathbf{H})^{-1}\mathbf{H}^T\mathbf{y}. \tag{7.22}$$

It is also possible through suitable parameterizations to extract information from multiple epochs of data using recursive least squares or Kalman filter methods.

WADGNSS Reference Network Design Constraints: In (7.21), if m represents the minimum number of satellites available per base station, then there will be at least Nm measurements and $4M+(N-1)$ unknowns[1]. To achieve an over-determined set of equations requires

$$Nm \geq 4M+(N-1) \tag{7.23}$$

Therefore, at least

$$N \geq \frac{4M-1}{m-1}$$

reference stations are required. For $M = 32$ and $m = 6$, at least $N = 26$ reference stations would be required. In addition, the reference stations must be geographically distributed such that the matrix $\mathbf{H}$ is full column rank and well-conditioned.

---

[1] The $(N-1)$ appears instead of N because clock errors can be estimated only relative to a fixed reference. Therefore, one of the values can be set to an arbitrary value such as zero.

Bibliography

[1] IEEE std 952: Specification format guide and test procedure for single-axis interferometric fiber optic gyros. Technical report, IEEE, 1997.

[2] IEEE std 1293: Specification format guide and test procedure for linear, single-axis, non-gyroscopic accelerometers. Technical report, IEEE, 1999.

[3] Priyanka Aggarwal, Zainab Syed, and Naser El-Sheimy. Hybrid extended particle filter (HEPF) for integrated inertial navigation and global positioning systems. *Meas. Science and Tech.*, 20(5), 2009.

[4] E. Aghapour, F. Rahman, and J. A. Farrell. Outlier accommodation in nonlinear state estimation: A risk-averse performance-specified approach. *IEEE T. Control Systems Technology, In Press*, 2019.

[5] M. De Agostino, A. Manzino, and G. Marucco. Doppler measurement integration for kinematic real-time GPS positioning. *Applied Geomatics*, 2(4):155–162, 2010.

[6] D. W. Allan. Statistics of atomic frequency standards. *P. IEEE*, 54(2):221–230, 1966.

[7] J. An and J. Lee. Improvement of GPS position estimation using SNR and Doppler. *in IEEE Int. Conf. on AIM*, pages 1645–1650, 2017.

[8] Richard J Anderle. Point positioning concept using precise ephemeris. *Satellite Doppler Positioning*, pages 47–75, 1976.

[9] A Angrisano, MG Petovello, and G Pugliano. GNSS/INS integration in vehicular urban navigation. *ION GNSS*, 2010.

[10] Anonymous. 10403.1 for Differential GNSS (Global Navigation Satellite Systems) Services-Version 3. Technical report, Radio Technical Commission for Maritime Services, 2006.

[11] Anonymous. RTCM 10403.2: Differential GNSS (Global Navigation Satellite Systems) Service. Technical report, Radio Technical Commission for Maritime Services, February, 2013.

[12] Anonymous. On-Board System Requirements for V2V Safety Communications. Technical report, Society of Automotive Engineers, March, 2016.

[13] EA Araujo-Pradere, TJ Fuller-Rowell, PSJ Spencer, and CF Minter. Differential validation of the US-TEC model. *Radio Science*, 42(3), 2007.

[14] V. Ashkenazi, C. J. Hill, W. Y. Ochieng, and J. Nagle. Wide-area differential GPS: A performance study. *Navigation*, 40(3)(3):297–319, 1993.

[15] J. A. Barnes, A. R. Chi, L. S. Cutler, D. J. Healey, D. B. Leeson, T. E. McGunigal, J. A. Mullen Jr., W. L. Smith, R. L. Sydnor, R. F. C. Vessot, and G. R. Winkler. Characterization of frequency stability. *IEEE Trans. Instrum. Meas.*, IM-20(2):105–120, 1971.

[16] C. Basnayake, M. Joerger, and J. Auld. Safety-Critical Positioning for Automotive Applications: Lessons from Civil Aviation. Technical report, Inside GNSS, November, 2016.

[17] Michael Bevis, Steven Businger, Thomas A Herring, Christian Rocken, Richard A Anthes, and Randolph H Ware. GPS meteorology: Remote sensing of atmospheric water vapor using the Global Positioning System. *Journal of Geophysical Research: Atmospheres*, 97 (D14):15787–15801, 1992.

[18] S Bisnath and Y Gao. Current state of precise point positioning and future prospects and limitations. *Proc. of International Association of Geodesy Symposia:Observing our Changing Earth, Springer*, pages 615–623, 2009.

[19] H. D. Black. An easily implemented algorithm for the tropospheric range correction. *J. Geophys. Res.*, 83(B4):1825–1828, 1978.

[20] G. Blewitt. Basics of the GPS Technique: Observation Equations. *Geodetic Applications of GNSS*, pages 10–54, 1997.

[21] Michael S Braasch and AJ Van Dierendonck. GPS receiver architectures and measurements. *Proc. of the IEEE*, 87(1):48–64, 1999.

[22] A. Brown. Extended Differential GPS. *Navigation*, 36(3):265–285, 1989.

[23] R. G. Brown and P. Y. C. Hwang. *Introduction to Random Signals and Applied Kalman Filtering with Matlab Exercises*. CourseSmart Series. Wiley, 2012.

[24] R.G Brown and PYC Hwang. *"Introduction to Random Signals and Applied Kalman Filtering"*. Wiley, New York, 1996.

[25] S. Cadzow et al. Connected Vehicle Pilot Deployment Program Phase 2: Data Privacy Plan-New York City. Technical report, USDOT, December, 2016.

[26] Changsheng Cai, Yangzhao Gong, Yang Gao, and Cuilin Kuang. An approach to speed up single-frequency PPP convergence with quad-constellation GNSS and GIM. *Sensors*, 17(6):1302, 2017.

[27] J. Ceva, W. Bertinger, R. Mullerschoen, Yunck T., and B. Parkinson. Incorporation of orbital dynamics to improve wide area differential GPS. *Proc. ION GPS*, 1995.

[28] CC Chao. The tropospheric calibration model for Mariner Mars 1971. Technical report 19740008870, JPL, Mar 01, 1974.

[29] Myungjun Choi, Juan Blanch, Dennis Akos, Liang Heng, Grace Gao, Todd Walter, and Per Enge. Demonstrations of multi-constellation advanced RAIM for vertical guidance using GPS and GLONASS signals. *ION GNSS*, pages 3227–3234, 2011.

[30] S Choy. Investigation into the accuracy of single frequency precise point positioning (PPP). *PhD Thesis. School of Mathematical and Geospatial Sciences, RMIT University*, 2009.

[31] P. Collins, R. B. Langley, and J. LaMance. Limiting Factors in Tropospheric Propagation Delay Error Modelling for GPS Airborne Navigation. *Proc. ION Annual Meeting*, 1996.

[32] JL Davis, TA Herring, II Shapiro, AEE Rogers, and Gunnar Elgered. Geodesy by radio interferometry: Effects of atmospheric modeling errors on estimates of baseline length. *Radio Science*, 20(6):1593–1607, 1985.

[33] Philip J Davis and Philip Rabinowitz. *"Methods of numerical integration"*. Courier Corporation, 2007.

[34] Peter F de Bakker and Christian CJM Tiberius. Real-time multi-GNSS single-frequency precise point positioning. *GPS Solutions*, 21(4):1791–1803, 2017.

[35] A. J. Dierendonck, J. B. McGraw, and R. G. Brown. Relationship between Allan variances and Kalman filter parameters. *Proc. 16th Annual Precise Time and Time Interval (PTTI) Applications and Planning Meeting*, pages 273–293, 1984.

[36] Yi Dong, Dingjie Wang, Liang Zhang, Qingsong Li, and Jie Wu. Tightly Coupled GNSS/INS Integration with Robust Sequential Kalman Filter for Accurate Vehicular Navigation. *Sensors*, 20(2):561, 2020.

[37] Jie Du and Matthew J Barth. Next-generation automated vehicle location systems: Positioning at the lane level. *IEEE Transactions on Intelligent Transportation Systems*, 9(1):48–57, 2008.

[38] Shuang Du, Yang Gao, et al. Integration of PPP GPS and low cost IMU. *The Canadian geomatics conference and symposium of commission I, ISPRS, Calgary, Alberta, Canada*, pages 15–18, 2010.

[39] Lars Dyrud, Aleksandar Jovancevic, Andrew Brown, Derek Wilson, and Suman Ganguly. Ionospheric measurement with GPS: Receiver techniques and methods. *Radio Science*, 43(6):1–11, 2008.

[40] M. B. El-Arini, J. A. Klobuchar, and P. H. Doherty. Evaluation of the GPS WAAS ionospheric grid algorithm during the peak of the current solar cycle. *Proc. ION National Technical Meeting*, 1994.

[41] M. B. El-Arini, P. A. O'Donnell, P. Kellam, J. A. Klobuchar, T. C. Wisser, and P. H. Doherty. The FAA wide area differential GPS (WADGPS) static ionospheric experiment. *Proc. ION National Technical Meeting*, 1993.

[42] M Bakry El-Arini, Patricia A O'Donnell, Paul M Kellam, John A Klobachar, Thomas C Wisser, and Patricia H Doherty. The FAA Wide Area Differential GPS(WADGPS) static ionospheric experiment. *Evolution through Integration of Current and Emerging Systems*, pages 485–496, 1993.

[43] Mohamed Elsheikh, Walid Abdelfatah, Aboelmagd Noureldin, Umar Iqbal, and Michael Korenberg. Low-Cost Real-Time PPP/INS Integration for Automated Land Vehicles. *Sensors*, 19(22):4896, 2019.

[44] Mohamed Elsobeiey and Salim Al-Harbi. Performance of real-time Precise Point Positioning using IGS real-time service. *GPS solutions*, 20(3)(3):565–571, 2016.

[45] P. Enge. The global positioning system: Signals, measurements, and performance. *Int. J. of Wireless Info. Net.*, 1(2):83–105, 1994.

[46] Per Enge, Todd Walter, Sam Pullen, Changdon Kee, Yi-Chung Chao, and Yeou-Jyh Tsai. Wide area augmentation of the global positioning system. *Proc. of the IEEE*, 84(8):1063–1088, 1996.

[47] Per K Enge, Rudolph M Kalafus, and Michel F Ruane. Differential operation of the global positioning system. *IEEE Comm. Mag.*, 26(7):48–60, 1988.

[48] Ashraf Farah. Accuracy Assessment Study of UNB3m Neutral Atmosphere Model for Global Tropospheric Delay Mitigation. *Artificial Satellites*, 50(4):201–215, 2015.

[49] J. A. Farrell. *"Aided Navigation: GNSS with High Rate Sensors"*. McGraw-Hill Inc, 2008.

[50] J. A. Farrell, M. Djodat, M. Barth, and M. Grewal. Latency compensation for differential GPS. *Navigation*, 44(1):99–107, 1997.

[51] J. A. Farrell, T. Givargis, and M. Barth. Real-time differential carrier phase GPS-aided INS. *IEEE T. Control Systems Technology*, 8:709–721, 2000.

[52] J.A Farrell. *Aided navigation: GPS with High Rate Sensors*. McGraw-Hill, Inc., 2008.

[53] Jay A Farrell, Tony D Givargis, and Matthew J Barth. Real-time differential carrier phase GPS-aided INS. *IEEE Transactions on Control Systems Technology*, 8(4):709–721, 2000.

[54] Jay A Farrell, Felipe O Silva, Farzana Rahman, and Jan Wendel. IMU Error State Modeling for State Estimation and Sensor Calibration: A Tutorial. *Proceedings of the IEEE, under review*, 2020.

[55] Tim Fuller-Rowell. USTEC: A new product from the Space Environment Center characterizing the ionospheric total electron content. *GPS Solutions*, 9(3):236–239, 2005.

[56] Yang Gao and Kongzhe Chen. Performance analysis of precise point positioning using real-time orbit and clock products. *Journal of Global Positioning Systems*, 3(1-2):95–100, 2004.

[57] Yang Gao and Xiaobing Shen. A New Method for Carrier-Phase-Based Precise Point Positioning. *Navigation*, 49(2):109–116, 2002.

[58] Yang Gao, Yufeng Zhang, and Kongzhe Chen. Development of a real-time single-frequency precise point positioning system and test results. *Ion GNSS*, pages 26–29, 2006.

[59] A. Gelb, J. F. Kasper Jr, R. A. Nash Jr, C. F. Price, and A. A. Sutherland Jr. *Applied Optimal Estimation*. Analytic Sciences Coorporation, 1974.

[60] J Geng, Felix Norman Teferle, X Meng, and AH Dodson. Towards PPP-RTK: Ambiguity resolution in real-time precise point positioning. *Advances in Space Research*, 47(10):1664–1673, 2011.

[61] C. Goad, B. W. Parkinson, J. J. Spliker Jr, P. Axelrad, and P. Enge. *Global Positioning System: Theory and Applications*. AIAA, 1996.

[62] M. S. Grewal, A. P. Andrews, and C. G. Bartone. *"Global Navigation Satellite Systems, Inertial Navigation & Integration"*. John Wiley & Sons, 2013.

[63] Mohinder S Grewal, Lawrence R Weill, and Angus P Andrews. *"Global Positioning System, Inertial Navigation,and Integration"*. John Wiley & Sons, 2007.

[64] P. D. Groves. *Principles of GNSS, Inertial, and Multisensor Integrated Navigation Systems*. Artech House Remote Sensing Library, 2013.

[65] Paul D Groves. Principles of GNSS, inertial, and multisensor integrated navigation systems, [Book review]. *IEEE Aerospace and Electronic Systems Magazine*, 30(2):26–27, 2015.

[66] Tomasz Hadas and Jaroslaw Bosy. IGS RTS precise orbits and clocks verification and quality degradation over time. *GPS Solutions*, 19(1):93–105, 2015.

[67] Jakob M Hansen, Thor I Fossen, and Tor Arne Johansen. Nonlinear observer design for GNSS-aided inertial navigation systems with time-delayed GNSS measurements. *Control Engineering Practice*, 60:39–50, 2017.

[68] R. R. Hatch. The synergism of GPS code and carrier measurements. *Proc. 3rd International Geodetic Symp. on Satellite Doppler Positioning*, 1982.

[69] J. Hidalgo-Carrió, S. Arnold, and P. Poulakis. On the design of attitude-heading reference systems using the allan variance. *IEEE Trans. Ultrason., Ferroelectr., Freq. Control*, 63(4):656–665, 2016.

[70] Sinpyo Hong, Man Hyung Lee, Ho-Hwan Chun, Sun-Hong Kwon, and Jason L Speyer. Observability of error states in GPS/INS integration. *IEEE Transactions on Vehicular Technology*, 54(2):731–743, 2005.

[71] Sinpyo Hong, Man Hyung Lee, Sun Hong Kwon, and Ho Hwan Chun. A car test for the estimation of GPS/INS alignment errors. *IEEE Transactions on Intelligent Transportation Systems*, 5(3):208–218, 2004.

[72] HS Hopfield. Two-quartic tropospheric refractivity profile for correcting satellite data. *Jour. of Geophy. Research*, 74(18):4487–4499, 1969.

[73] N. Jakowski, C. Mayer, M. M. Hoque, and V. Wilken. Total electron content models and their use in ionosphere monitoring. *Radio Science*, 46(RS0D18):1–11, 1994.

[74] Christopher Jekeli. *Inertial navigation systems with geodetic applications*. Walter de Gruyter, 2012.

[75] S. Johnson, L. Rolfes, et al. Connected Vehicle Pilot Deployment Program Phase II Data Privacy Plan-Tampa (THEA). Technical report, USDOT, February, 2017.

[76] E. D. Kaplan and C. J. Hegarty. *Understanding GPS/GNSS - Principles and Applications*. Artech House, 2018.

[77] K Kazmierski, M Santos, and J Bosy. Tropospheric delay modeling for the EGNOS augmentation system. *Survey Review*, 49(357):399–407, 2017.

[78] C. Kee and B. W. Parkinson. Algorithms and implementation of wide area differential GPS. *Proc. ION GPS*, 1992.

[79] C. Kee and B. W. Parkinson. High accuracy GPS positioning in the continent: Wide area differential GPS. *Proc. Differential Satellite Navigation Systems*, 1993.

[80] C. Kee and B. W. Parkinson. Wide area differential GPS as a future navigation system in the U.S. *IEEE Proc. Position Location and Navigation Symposium*, 1994.

[81] C. Kee and B. W. Parkinson. Wide area differential GPS (WADGPS): Future navigation system. *IEEE T. Aero. Elec. Sys.*, 32(2):795–808, 1996.

[82] C. Kee, B. W. Parkinson, and P. Axelrad. Wide area differential GPS. *Navigation*, 38(2):123–145, 1991.

[83] Changdon Kee, Bradford W Parkinson, and Penina Axelrad. Wide area differential GPS. *Navigation*, 38(2):123–145, 1991.

[84] F. M. Kitchener, T. English, et al. Connected Vehicle Pilot Deployment Program Phase 2, Data Management Plan-Wyoming. Technical report, USDOT, April, 2017.

[85] J. A. Klobuchar, P. H. Doherty, and M. B. El-Arini. Potential ionospheric limitations to Wide Area Differential GPS. *Proc. ION GPS*, 1993.

[86] John A Klobuchar. Ionospheric time-delay algorithm for single-frequency GPS users. *IEEE Trans. on Aerospace and Electronic Systems*, (3):325–331, 1987.

[87] Victor L Knoop, Peter F de Bakker, Christian CJM Tiberius, and Bart van Arem. Lane determination with GPS precise point positioning. *IEEE Trans. on Intelligent Transportation Systems*, 18(9):2503–2513, 2017.

[88] Jan Kouba. A guide to using International GNSS Service (IGS) products. Technical report, IGS Central Bureau, Pasadena, 2009.

[89] Jan Kouba and Pierre Héroux. Precise point positioning using IGS orbit and clock products. *GPS solutions*, 5(2):12–28, 2001.

[90] Gregory T Kremer, Rudolph M Kalafus, Peter VW Loomis, and James C Reynolds. The effect of selective availability on differential GPS corrections. *Navigation*, 37(1):39–52, 1990.

[91] Grzegorz Krzan and Paweł Przestrzelski. GPS/GLONASS precise point positioning with IGS real-time service products. *Acta Geodyn. Geomater*, 13(1):69–81, 2016.

[92] Gérard Lachapelle. GNSS observables and error sources for kinematic positioning. *Kinematic Systems in Geodesy, Surveying, and Remote Sensing*, pages 17–26, 1991.

[93] Herbert Landau, Ulrich Vollath, Xiaoming Chen, et al. Virtual reference station systems. *Journal of Global Positioning Systems*, 1(2):137–143, 2002.

[94] G Lanyi. Tropospheric delay effects in radio interferometry. *TDA Prog. Rep. 42-78, vol. April*, pages 152–159, 1984.

[95] D Laurichesse. The CNES Real-time PPP with undifferenced integer ambiguity resolution demonstrator. *Proceedings of the ION GNSS*, pages 654–662, 2011.

[96] Rodrigo Leandro, MC Santos, and Richard B Langley. UNB neutral atmosphere models: development and performance. *Proc. of ION NTM*, 52(1):564–73, 2006.

[97] Liang Li, Chun Jia, Lin Zhao, Jianhua Cheng, Jianxu Liu, and Jicheng Ding. Real-time single frequency precise point positioning using SBAS corrections. *Sensors*, 16(8):1261, 2016.

[98] Wei Li, YunBin Yuan, JiKun Ou, Hui Li, and ZiShen Li. A new global zenith tropospheric delay model IGGtrop for GNSS applications. *Chinese Science Bulletin*, 57(17):2132–2139, 2012.

[99] Hang Liu, Sameh Nassar, and Naser El-Sheimy. Two-filter smoothing for accurate INS/GPS land-vehicle navigation in urban centers. *IEEE Trans. on Vehicular Tech.*, 59(9):4256–4267, 2010.

[100] Shuai Liu, Fuping Sun, Lundong Zhang, Wanli Li, and Xinhui Zhu. Tight integration of ambiguity-fixed ppp and ins: model description and initial results. *GPS solutions*, 20(1):39–49, 2016.

[101] Wenjiao Liu. Positioning performance of single-frequency GNSS receiver using Australian regional ionospheric corrections. *Queensland University of Technology*, 2016.

[102] Yue Liu, Fei Liu, Yang Gao, and Lin Zhao. Implementation and Analysis of Tightly Coupled Global Navigation Satellite System Precise Point Positioning/Inertial Navigation System (GNSS PPP/INS) with Insufficient Satellites for Land Vehicle Navigation. *Sensors*, 18(2):4305, 2018.

[103] P. V. W. Loomis, R. P. Denaro, and P Saunders. Worldwide differential GPS for space shuttle landing operations. *IEEE Position Location and Navigation Symp.*, 1990.

[104] Peter Loomis, Greg Kremer, and James Reynolds. Correction algorithms for differential GPS reference stations. *Navigation*, 36(2):179–193, 1989.

[105] Yidong Lou, Fu Zheng, Shengfeng Gu, Charles Wang, Hailin Guo, and Yanming Feng. Multi-GNSS precise point positioning with raw single-frequency and dual-frequency measurement models. *GPS Solutions*, 20(4):849–862, 2016.

[106] AJ Mannucci, BD Wilson, DN Yuan, CH Ho, UJ Lindqwister, and TF Runge. A global mapping technique for GPS-derived ionospheric total electron content measurements. *Radio Science*, 33(3):565–582, 1998.

[107] Z. Miao, F. Shen, D. Xu, K. He, and C. Tian. Online estimation of Allan variance coefficients based on a neural-extended Kalman filter. *Sensors*, 15(1):2496–2524, 2015.

[108] P. Misra and P. Enge. Special issue on global positioning system. *Proc. of the IEEE*, 87(1):3–15, 1999.

[109] P. Misra and P. Enge. *Global Positioning System: Signals, Measurements and Performance*. Massachusetts: Ganga-Jamuna Press, 2 edition, 2006.

[110] Ronald Muellerschoen, Willy Bertiger, Michael Lough, Dave Stowers, and Danan Dong. An internet-based global differential GPS system, initial results. *ION GPS*, 2000.

[111] S. Nassar, K. P. Scharwz, and N. El-Sheimy. Modeling inertial sensor errors using autoregressive AR models. *Navigation*, 51(4):259–268, 2004.

[112] Jerzy Neyman and Egon S Pearson. The testing of statistical hypotheses in relation to probabilities a priori. *Cambridge University Press*, pages 492–510, 1933.

[113] Lau N Nguyen and Can Pham. Improving Accuracy of Real Time Kinematic Positioning by Using PPP With IGS-RTS Corrections. 2018.

[114] AE Niell. Improved atmospheric mapping functions for VLBI and GPS. *Earth, Planets and Space*, 52(10):699–702, 2000.

[115] D. Odijk and L. Wanninger. *Springer Handbook of Global Navigation Satellite Systems*. Springer, 2017.

[116] M. H. Pajares, J. M. Juan, and J. Sanz. New approaches in global ionospheric determination using ground GPS data. *J. Atmos. Sol. - Terr. Phy.*, 61(1)(1):1237–1247, 1999.

[117] Byungwoon Park, Cheolsoon Lim, Youngsun Yun, Euiho Kim, and Changdon Kee. Optimal divergence-free Hatch filter for GNSS single-frequency measurement. *Sensors*, 17(3):448, 2017.

[118] Bradford W Parkinson, Per Enge, Penina Axelrad, and James J Spilker Jr. *Global positioning system: Theory and applications*. American Inst. of Aeronautics and Astronautics, 1996.

[119] Fabricio dos Santos Prol, Paulo de Oliveira Camargo, and Marcio Tadeu de Assis Honorato Muella. Comparative study of methods for calculating ionospheric points and describing the GNSS signal path. *Boletim de Ciências Geodésicas*, 23(4):669–683, 2017.

[120] A. G. Quinchia, G. Falco, E. Falletti, F. Dovis, and C. Ferrer. A comparison between different error modeling of MEMS applied to GPS/INS integrated systems. *Sensors*, 13(1):9549–9588, 2013.

[121] F. Rahman, E. Aghapour, and J. A. Farrell. ECEF Position Accuracy and Reliability in the Presence of Differential Correction Latency. *IEEE/ION PLANS*, pages 583–588, 2018.

[122] F. Rahman, E. Aghapour, and J. A. Farrell. ECEF Position Accuracy and Reliability in the Presence of Differential Correction Latency: Phase A Technical Report. Technical report, University of California, Riverside (escholarship.org/uc/item/38d3h08w), October, 2018.

[123] F. Rahman and J. A. Farrell. Earth-Centered Earth-Fixed (ECEF) Vehicle State Estimation Performance. *CCTA*, 2019.

[124] F. Rahman and J. A. Farrell. ECEF Position Accuracy and Reliability:Continent Scale Differential GNSS Approaches: Phase C Technical Report for Sirius XM. Technical report, University of California, Riverside (https://escholarship.org/uc/item/05p9p3c9), July, 2019.

[125] F. Rahman and J. A. Farrell. ECEF Position Accuracy and Reliability in the Presence of Differential Correction Latency: Phase B Technical Report. Technical report, University of California, Riverside (escholarship.org/uc/item/135578mw), June, 2019.

[126] Farzana Rahman, Elahe Aghapour, and Jay A Farrell. Vehicle ECEF Position Accuracy and Reliability in the Presence of DGNSS Communication Latency. *IEEE Intelligent Transportation Systems Magazine*, 2020.

[127] Arvind Ramanandan, Anning Chen, and Jay A Farrell. Inertial navigation aiding by stationary updates. *IEEE Transactions on Intelligent Transportation Systems*, 13(1):235–248, 2011.

[128] P. F. Roysdon and J. A. Farrell. Technical Note: INS Noise Propagation. Technical report, October, 2018.

[129] J Saastamoinen. Atmospheric correction for the troposphere and stratosphere in radio ranging satellites. *The Use of Artificial Satellites for Geodesy*, pages 247–251, 1972.

[130] E. Sardón, A. Rius, and N. Zarraoa. Estimation of the transmitter and receiver differential biases and the ionospheric total electron content from Global Positioning System observations. *Radio Science*, 29(3):577–586, 1994.

[131] P. G. Savage. *Strapdown Analytics*. Strapdown Associates, 2007.

[132] Luis Serrano, Don Kim, and Richard B Langley. A single GPS receiver as a real-time, accurate velocity and acceleration sensor. *17th Int. Tech. Meeting of the Sat. Div. of ION*, 2124, 2004.

[133] Luis Serrano, Donghyun Kim, Richard B Langley, Kenji Itani, and Mami Ueno. A GPS velocity sensor: how accurate can it be?–a first look. *ION NTM*, 2004:875–885, 2004.

[134] Atsushi Shimamura. MSAS (MTSAT satellite-based augmentation system) project status. *Air & Space Europe*, 1(2):63–67, 1999.

[135] Isaac Skog and Peter Handel. In-car positioning and navigation technologiesA survey. *IEEE Transactions on Intelligent Transportation Systems*, 10(1):4–21, 2009.

[136] Y. Stebler, S. Guerrier, J. Skaloud, and M. P. Victoria-Feser. A framework for inertial sensor calibration using complex stochastic error models. *Proc. Position, Location and Navigation Symp.*, pages 849–861, 2012.

[137] Dhiraj Sunehra. TEC and Instrumental Bias Estimation of GAGAN Station Using Kalman Filter and SCORE Algorithm. *Positioning*, 7(1):41, 2015.

[138] M. M. Tehrani. Ring laser gyro data analysis with cluster sampling technique. *Proc. SPIE*, 412(1):207–220, 1983.

[139] A. Tetewsky, J. Ross, A. Soltz, N. Vaughn, J. Anszperger, C. O'Brien, D. Graham, D. Craig, and J. Lozow. Making sense of inter-signal corrections: accounting for GPS satellite calibration parameters in legacy and modernized ionosphere correction algorithms. *Inside GNSS*, July-August(1):37–48, 2009.

[140] P. Teunissen and O. Montenbruck. *Handbook of Global Navigation Satellite Systems*. Springer International Publishing, 2017.

[141] PJG Teunissen. Differential GPS: Concepts and Quality Control. *Netherlands Institution of Navigation, Amsterdam*, 1991.

[142] PJG Teunissen and Amir Khodabandeh. Review and principles of PPP-RTK methods. *Jour. of Geodesy*, 89(3):217–240, 2015.

[143] David Titterton, John L Weston, and John Weston. *Strapdown inertial navigation technology*, volume 17. IET, 2004.

[144] Rafael Toledo-Moreo, David Bétaille, and François Peyret. Lane-level integrity provision for navigation and map matching with GNSS, dead reckoning, and enhanced maps. *IEEE Transactions on Intelligent Transportation Systems*, 11(1):100–112, 2009.

[145] Rafael Toledo-Moreo, Miguel A Zamora-Izquierdo, Benito Ubeda-Minarro, and Antonio F Gómez-Skarmeta. High-integrity IMM-EKF-based road vehicle navigation with low-cost GPS/SBAS/INS. *IEEE Transactions on Intelligent Transportation Systems*, 8(3):491–511, 2007.

[146] RJP Van Bree, PJ Buist, CCJM Tiberius, B Van Arem, and VL Knoop. Lane identification with real time single frequency precise point positioning: A kinematic trial. *ION GNSS*, pages 19–23, 2011.

[147] Roel JP van Bree and Christian CJM Tiberius. Real-time single-frequency precise point positioning: accuracy assessment. *GPS Solutions*, 16(2):259–266, 2012.

[148] Anh Vu, Jay A Farrell, and Matthew Barth. Centimeter-accuracy smoothed vehicle trajectory estimation. *IEEE Intel. Transp. Sys. Mag.*, 5(4):121–135, 2013.

[149] Anh Vu, Arvind Ramanandan, Anning Chen, Jay A Farrell, and Matthew Barth. Real-time computer vision/DGPS-aided inertial navigation system for lane-level vehicle navigation. *IEEE Transactions on Intelligent Transportation Systems*, 13(2):899–913, 2012.

[150] B. D. Wilson and A. J. Mannucci. Instrumental biases in ionospheric measurements derived from GPS data. *Proc. ION*, 1993.

[151] Z. Xing and D. Gebre-Egziabher. Modeling and bounding low cost inertial sensor errors. *Proc. Position Location and Navigation Symp.*, pages 1122–1132, 2008.

[152] Hongxing Zhang, Yunbin Yuan, Wei Li, Ying Li, and Yanju Chai. Assessment of three tropospheric delay models (IGGtrop, EGNOS and UNB3m) based on precise point positioning in the Chinese region. *Sensors*, 16(1):122, 2016.

[153] Junchuan Zhou, Yuhong Yang, Jieying Zhang, Ezzaldeen Edwan, Otmar Loffeld, and Stefan Knedlik. Tightly-coupled INS/GPS using Quaternion-based Unscented Kalman filter. *AIAA Guidance, Navigation, and Control Conference*, page 6488, 2011.

[154] JF Zumberge, MB Heflin, DC Jefferson, MM Watkins, and FH Webb. Precise point positioning for the efficient and robust analysis of GPS data from large networks. *Jour. of Geophysical Research: Solid Earth*, 102(B3):5005–5017, 1997.